Constraining the carbon budgets of croplands with Earth observation data

by

Andrew Revill

Thesis submitted in fulfilment of
the requirements for the degree of
Doctor of Philosophy
to the
University of Edinburgh
May, 2016

Declaration

I confirm that the work compiled and presented in this thesis is my own and has not been submitted for any other degree or professional qualification, except where explicitly stated otherwise in the text. In particular, research detailed in Chapters 2, 3 and 4 was adapted from papers that are either published or currently in review. I am lead author of the papers and the specific contributions from all co-authors are declared at the beginning of these chapters.

A. Revill

Andrew Revill

Tuesday, 18 May 2016

Acknowledgements

By way of a PhD studentship, I acknowledge that the research in this thesis was jointly funded by the School of Geosciences at the University of Edinburgh and the UK National Centre for Earth Observation (NCEO).

This thesis could not have been achieved without help from many students and staff within the School of Geosciences. Special thanks goes to my supervisor Mat Williams for first, giving me the opportunity to carry out this research and second, for providing continual support and advice throughout the last four years. The importance of clarity when writing and presenting a scientific analysis is one of the key skills I have developed under Mat's supervision.

I am grateful to Oliver Sus and Oliver Browne for their support when implementing the SPAc model. Many thanks to Anthony Bloom and Luke Smallman for sharing their technical experience – particularly when applying and evaluating the model-data fusion approaches. I would like to thank other members of the Global Change Ecology Lab (GCEL), including Darren Slevin and Jeff Exbrayat, for their help. I thank Mathias Disney, from the University College London, for his helpful comments on an earlier version of the research presented in Chapter 2.

Many thanks to my parents who have always supported the decisions and directions I have headed in over the years. And finally, I would like to thank Narelle for her patience when coming on this journey with me.

Abstract

Cropland management practices have traditionally focused on maximising the production of food, feed and fibre. However, croplands also provide valuable regulating ecosystem services, including carbon (C) storage in soil and biomass. Consequently, management impacts the extents to which croplands act as sources or sinks of atmospheric carbon dioxide (CO_2). And so, reliable information on cropland ecosystem C fluxes and yields are essential for policy-makers concerned with climate change mitigation and food security.

Eddy-covariance (EC) flux towers can provide observations of net ecosystem exchanges (NEE) of CO_2 within croplands, however the tower sites are temporally and spatially sparse. Process-based crop models simulate the key biophysical mechanisms within cropland ecosystems, including the management impacts, crop cultivar, soil and climate on crop C dynamics. The models are therefore a powerful tool for diagnosing and forecasting C fluxes and yield. However, crop model spatial upscaling is often limited by input data (including meteorological drivers and management), parameter uncertainty and model complexity. Earth observation (EO) sensors can provide regular estimates of crop condition over large extents. Therefore, EO data can be used within data assimilation (DA) schemes to parameterise and constrain models.

Research presented in this thesis explores the key challenges associated with crop model upscaling. First, fine-scale (20-50 m) EO-derived data, from optical and radar sensors, is assimilated into the Soil-Plant-Atmosphere crop (SPAc) model. Assimilating all EO data enhanced the simulation of daily C exchanges at multiple European crop sites. However, the individually assimilation of radar EO data (as opposed to combined with optical data) resulted in larger improvements in the C fluxes simulation. Second, the impacts of reduced model complexity and driver resolution on crop photosynthesis estimates are investigated. The simplified Aggregated Canopy Model (ACM) – estimating daily photosynthesis using coarse-scale (daily) drivers – was calibrated using the detailed SPAc model, which simulates leaf to canopy processes at half-hourly time-steps. The calibrated ACM photosynthesis had a high agreement with SPAc and local EC estimates. Third, a model-data fusion framework was evaluated for multi-annual and regional-scale estimation of UK wheat yields. Aggregated model yield estimates were negatively biased when compared to official statistics. Coarse-scale (1 km) EO data was also used to constrain the model simulation of canopy development, which was successful in reducing the biases in the yield estimates. And fourth, EO spatial and temporal resolution requirements for crop growth monitoring at UK field-scales was investigated. Errors due to spatial resolution are quantified by sampling aggregated fine scale EO data on a per-field basis; whereas temporal resolution error analysis involved re-sampling model estimates to mimic the observational frequencies of current EO sensors and likely cloud cover. A minimum EO spatial resolution of around 165 m is required to resolve the field-scale detail. Monitoring crop growth using EO sensors with a 26-day temporal resolution results in a mean error of 5%; however, accounting for likely cloud cover

increases this error to 63%.

Lay summary

Variability in crop yield is strongly determined by climate and management factors. Crop growth also generates large land-atmosphere exchanges of carbon dioxide (CO_2), which is a dominant greenhouse gas. And so, reliable estimates of crop growth and yield, to support a growing population, are essential for policy-makers concerned with climate change and food security.

Computer-based crop models mathematically describe the key biophysical processes of crop growth in response to regular (e.g. half-hourly to daily) weather observations and management. The models can therefore estimate daily crop development, net CO_2 exchanges and yield. However, crop models have often been calibrated at field-scales, and thus can lack validity when applied to generate regional-scale estimates. Satellite Earth observation (EO) data, on the other hand, can provide information over large areas, which can be used to update the crop model estimates.

The essence of the research compiled within this thesis is to explore crop modelling approaches, including the integration of EO data, for spatially upscaling estimates of crop vegetation CO_2 exchanges and yield. Findings from the four main research chapters can be summarised as:

1) Data from optical and radar EO sensors can be used to update and improve a crop model simulation of daily CO_2 exchanges.

2) A simple model of crop photosynthesis can be calibrated to reproduce estimates from a more detailed model. The simple model requires relatively minimal inputs and runs at much higher computational speeds and, therefore, could feasibly be used to generate regional-scale estimates.

3) Crop models can produce reasonable regional-scale estimates of yield. Integrating models with coarse-scale (1 km) EO data shows potential for improving these estimates.

4) EO sensors that have a spatial resolution of around 165 m can be used to resolve the field-scale detail of typical UK croplands. When using multi-temporal optical EO data to monitor crop growth, errors from current sensors can be as large as 63% when accounting for the likely cloud cover over dominant UK growing areas.

Contents

Chapter 3: Impacts of reduced model complexity and driver resolution on cropland ecosystem photosynthesis estimates ……………………………………… 64

Chapter 5: Earth observation spatial and temporal resolution requirements for crop growth monitoring at UK field-scales ……………………...…………… 140

List of Figures

Chapter 1: General Introduction………………………………………………….. 1

Chapter 2: Carbon cycling of European Croplands: A framework for the assimilation of optical and microwave Earth observation data 27

Chapter 3: Impacts of reduced model complexity and driver resolution on cropland ecosystem photosynthesis estimates…………………………………… 64

List of Tables

Chapter 2: Carbon cycling of European Croplands: A framework for the assimilation of optical and microwave Earth observation data 27

Chapter 3: Impacts of reduced model complexity and driver resolution on cropland ecosystem photosynthesis estimates ……………………………………64

Chapter 4: Model-data fusion approaches for the regional and multi-annual assessment of UK winter wheat yields ………………………………………..103

Chapter 5: Earth observation spatial and temporal resolution requirements for crop growth monitoring at UK field-scales ……………………………………..140

List of Acronyms

ACM	Aggregated Canopy Model
AOI	Areas of Interest
C	Carbon
CCD	Crop Calendar Dataset
CEH	Centre for Ecology and Hydrology
CERES	Crop Environment REsource Synthesis
CHESS	Climate, Hydrology and Ecology research Support System
DA	Data Assimilation
DALECc	Data Assimilation Linked Ecosystem Carbon crop
DEFRA	Department for Environmental Food & Rural Affairs
EC	Eddy-covariance
EnKF	Ensemble Kalman Filter
EO	Earth Observation
EOSDIS	Earth Observing System Data and Information System
ERS	European Remote Sensing
ESA	European Space Agency
FAO	Food and Agriculture Organisation

GEOGLAM	Group on Earth Observation’s Global Agricultural Monitoring
GHG	Greenhouse Gas
GIS	Geographical Information System
GPP	Gross Primary Production
G-R	Gelman-Rubin
GSD	Ground sampling distance
ha	Hectare
IFOV	Instantaneous field of view
IFPRI	International Food Policy Research Institute
IPCC	Intergovernmental Panel on Climate Change
LAI	Leaf Area Index
MHMCMC	Metropolis-Hastings Markov Chain Monte Carlo
MODIS	MODerate resolution Imaging Spectrometer instrument
NASA	National Aeronautics and Space Administration
NDVI	Normalised Difference Vegetation Index
NEE	Net Ecosystem Exchange
NEP	Net Ecosystem Productivity
NMB	Normalised mean bias
NPP	Net Ecosystem Productivity
NRC	National Research Council (Canada)
OS	Ordnance Survey
OSGB	Ordnance Survey National Grid

OSMM	Ordnance Survey MasterMap
PP	Partial pressure
QA	Quality assurance
RH	Relative Humidity
RMSE	Root-mean-square-error
SAIL	Scattering by Arbitrary Inclined Leaves
SAR	Synthetic Aperture Radar
SPAc	Soil-Plant-Atmosphere crop
SPOT	Satellite Pour l'Observation de la Terre
SVP	Saturation vapour pressure
UTM	Universal Transverse Mercator
VPD	Vapour pressure deficit
WDVI	Weighted Difference Vegetation Index
WOFOST	WOrld FOod STudies

CHAPTER 1

General Introduction

1.1. Cropland ecosystems in the 21st century: the importance and key challenges

Globally, agricultural ecosystems are entirely managed, with farming practices being applied on a range of spatial and temporal scales (Porter and Semenov, 2005; Reichstein *et al.*, 2013). This agricultural land cover includes croplands – defined throughout this thesis as land devoted to the production of cultivated crops (FAO, 2002). At the beginning of the 21st century, croplands occupied around 12% of the Earth's ice-free land surface (Wood, 2000; see Figure 1.1) with around 33% and 20% of this land located in Europe and North America, respectively (Ramankutty *et al.*, 2008).

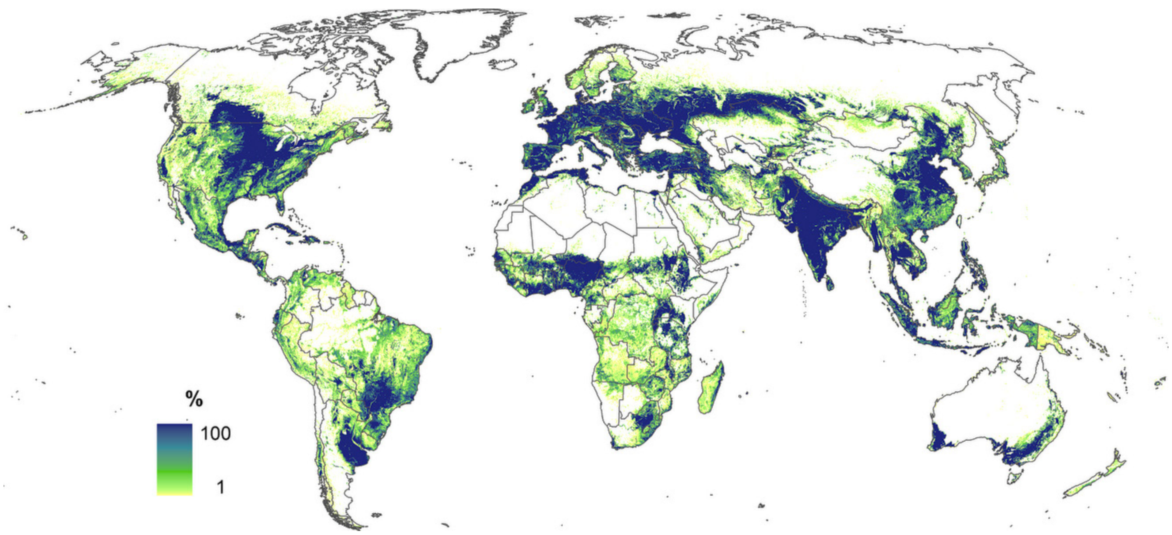

Figure 1.1: The IIASA-IFPRI global map of the percentage likelihood of croplands for the baseline year 2005. Data is derived from merging land cover products that are spatially aggregated to 0.0083° (≈ 1 km) resolution. Additional calibrations include the integration of national and sub-national cropland statistics from the Food and Agricultural Organisation (FAO) and the International Food Policy Research Institute (IFPRI, source: Fritz *et al.*, 2015).

Cropland ecosystems are essential for sustaining human life and environmental well-being (Zhang *et al.*, 2007; Robertson *et al.*, 2014). The Millennium Ecosystem Assessment (MEA, 2005) classifies ecosystem services into four interrelating categories: provisioning, regulating, cultural and supporting services. Traditionally, cropland management practices have focused on the provisioning services; most notably maximising yields in the production of food, feed, fibre and, more recently, bioenergy (Foley *et al.*, 2005; Power, 2010).

Since the arrival of 'Green Revolution' technologies – from around the late 1950s – there have been continual developments in agricultural machinery, agrochemicals and high-yielding crop cultivars. These advancements have mainly been driven by increased profits for farmers and higher grain yields (Tilman *et al.*, 2001; Gordon *et al.*, 2010). Coupled with a 12% increase in the global cropland area (Foley *et al.*, 2005), these technological achievements have resulted in a roughly two-fold increase in world grain yields over the past 40 to 50 years (Tilman *et al.*, 2001). As a more recent example, wheat crop – one of the most important crops grown worldwide – has seen an increase in production of around 9% between 1990 and 2010 (FAO, 2015). Consequently, this global increase in crop production has generally outpaced population growth in the majority of regions (Dorigo *et al.*, 2007).

Due to the combination of a rising population, dietary change and increasing income, the Food and Agricultural Organisation (FAO) of the United Nations estimate that a 70% increase in cereal crop yield is required to meet the increase in global food demand between the years 2000 to 2050 (Alexandratos and Bruinsma, 2012). Furthermore, Tilman *et al.* (2011) estimates that general food production needs to increase by 100 to 110% by 2050. Although higher crop production can be achieved through increasing the available cropland area, it is estimated that intensification (including increases in the input of fertilisers, pesticide and irrigation) will account for 80% of the future yield increases (Alexandratos and Bruinsma, 2012). However, there is a growing awareness of the detrimental impacts of intensive cropland management on the supporting ecosystem services, such as biodiversity and nutrient cycling, and regulating ecosystem services, including water and climate regulation (Power, 2010; Robertson *et al.*, 2014).

The role of croplands in regulating global climate change, through greenhouse gas (GHG) emissions, is of notable concern (Smith *et al.*, 2014). In 2005, total agricultural production, including croplands, accounted for an estimated 12-14% of global annual anthropogenic GHG emissions (IPCC, 2007). Among the principal GHGs affected by croplands is that of carbon dioxide (CO_2). This CO_2 is mainly released through disturbances to the soil and biomass carbon (C) pools, for instance tillage/ploughing and the management of crop residues (Ceschia *et al.*, 2010).

Feeding a growing population whilst adapting to a more sustainable means of production – required to preserve essential ecosystems services – pose major challenges to policy-makers concerned with food security and climate change (Foley *et al.*, 2011; Bajzelj *et al.*, 2014; Johnson *et al.*, 2014). At regional to global scales, the trade-offs associated with management practices are further compounded by spatial and temporal variability in climate, culture and socio-economic conditions (Power, 2010). This includes variability in planting and harvest dates, crop rotation, tillage, fertilisation, irrigation and pest control (Lokupitiya *et al.*, 2009). For instance, the European Union (EU-28), with croplands occupying around a quarter (24.7%) of the land area (Eurostat, 2013b), presents a mosaic of crop varieties, developmental stages and growth periods. This diversity is a consequence of spatio-temporal variations in soil and climatic conditions, together with local and regional production requirements. And so, this variability results in a broad range of management techniques – causing uncertainty when generalising the impacts of specific activities on crop C budgets (Osborne *et al.*, 2010).

1.2. Crop C budgets and the impacts of management

When compared to unmanaged natural vegetation, crops have a stronger uptake of atmospheric CO_2 as they are generally more productive due to intensive management (MacBean and Peylin, 2014). Specifically, crop gross primary production (GPP) gained through biomass production is estimated to contribute around 15% of global CO_2 fixation (Malmstrom *et al.*, 1997). However, in contrast to the volume of literature on crop yield, research investigating crop C budget processes and emissions associated with management has been scarce (Sus *et al.*, 2010; Ciais *et al.*, 2011).

Climate and management practices strongly influence the key crop C cycle processes, including the net fixation of atmopheric CO_2, termed net ecosystem exchange (NEE). NEE expresses the balance between the total amount of C released through total ecosystem respiration (R_{total}) and the uptake of atmospheric CO_2 used in photosynthesis (i.e. GPP):

$$NEE = R_{\text{total}} - GPP \qquad \text{Equation 1.1}$$

where R_{total} is the sum of autotrophic respiration (R_{a}, the respiration from vegetation) and heterotrophic respiration (R_{h}, total respiration from animals and microbes):

$$R_{\text{total}} = R_{\text{a}} + R_{\text{h}} \qquad \text{Equation 1.2}$$

Approximately half of the GPP is used by R_{a} for the maintenance and production of new vegetation (Waring *et al.*, 1998), and the remaining fraction of GPP, defined as the net primary production (NPP), is partitioned throughout the vegetation organs (Penning de Vries *et al.*, 1989).

$$NPP = GPP - R_{\mathrm{a}} \qquad \text{Equation 1.3}$$

In cropland ecosystems, further to the release of C due to R_{total} (including R_{h} of the soil and vegetation micro-organisms), a fraction of C is exported through harvest removal (Figure 1.2). However, some C remains as crop residue and soil organic carbon (SOC). Management modifies the SOC pool either by removing C through R_{a}, due to tillage/ploughing, or the additional C by applying manure (Ciais *et al.*, 2011). And so, through increasing crop residue in soils, farming practices can potential be adapted to sequester atmospheric CO_2, thereby mitigating the negative impacts of climate change (Smith *et al.*, 2007; Zhang *et al.*, 2015).

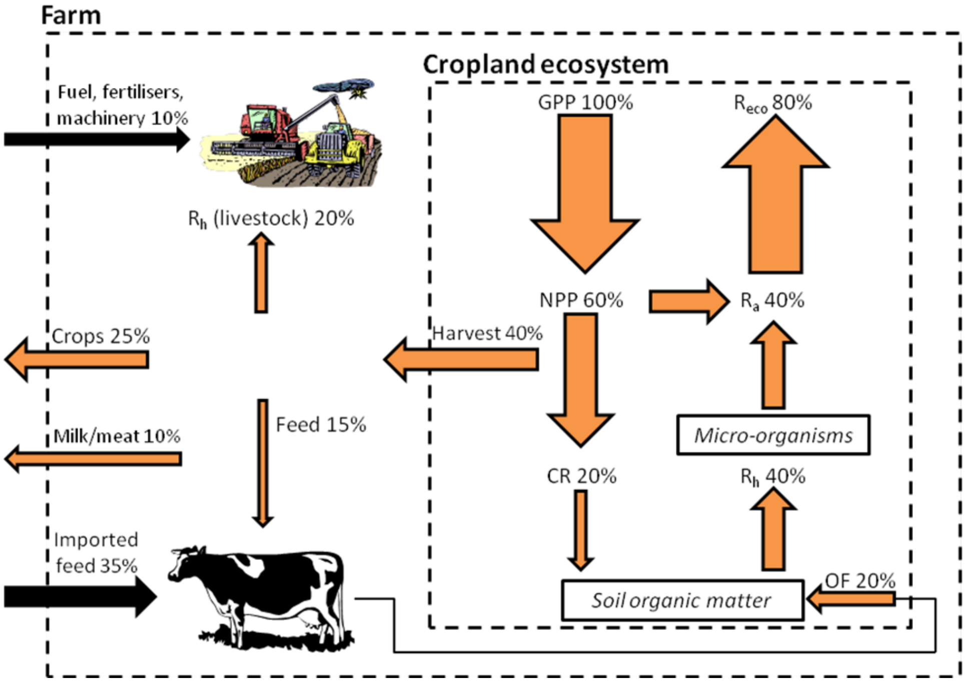

Figure 1.2: Schematic representation of the key components of the cropland C cycle, including 'off-site' fluxes of exported C (crops 25% and milk/meat products 10%) and imported C (livestock feed 35%, fuel and fertilisers 10%). Within the cropland ecosystem (i.e. field) 20% of total GPP is allocated to crop residuals (CR). About 15% of the total crop harvest C is allocated to feed livestock, 20% of which is then respired by the livestock and a further 20% is returned to the cropland ecosystem as organic fertiliser (OF) (adapted from: Smith *et al.*, 2010).

1.3. Crop C budget measuring and modelling approaches

Reliable information on the magnitude and spatial variability of C fluxes across cropland landscapes are essential for understanding the processes that drive the crop C cycle (Sus *et al.*, 2010; Zhang *et al.*, 2015). In recent decades, eddy-covariance (EC) flux towers have been used to provide direct NEE flux measurements at plot/field-scales (Baldocchi, 2003;

Ceschia *et al.*, 2010; Smith *et al.*, 2010; Xiao *et al.*, 2011). EC data, such as that available from the Global FLUXNET regional network (fluxnet.ornl.gov, Figure 1.3), is recorded at high frequencies within the spatial extents of the sensor 'footprint', which can vary from hundreds of meters to several kilometres due to changeable wind speed and direction (Schmid, 1994). Although EC datasets are available for multiple locations, crop types, seasons and climate regimes, globally the tower sites are sparsely distributed and C fluxes remain inherently under-sampled (Zheng *et al.*, 2014). Complex terrain and typically heterogeneous spatial distributions of vegetation within the footprint (e.g. multiple fields and hedgerows) also undermines the assumptions involved with the EC approach, which causes uncertainty in NEE observations (Baldocchi, 2003; Finnigan *et al.*, 2003; Hollinger and Richardson, 2005). Further uncertainty arises from empirically estimating values when gap-filling incomplete time-series datasets (Williams *et al.*, 2005; Osborne *et al.*, 2010)

Figure 1.3: EC flux towers in a maize/wheat crop rotation field located in Lamasquère, south-west France (source: fluxnet.ornl.gov).

Approaches to modelling the impacts of variable environmental drivers on the cropland C budget include empirical and process-based models. Empirical models assume a statistical relationship between an agronomic variable (e.g. biomass or yield) and a predictor, such as mean temperature (e.g. Lobell and Burke, 2010; Lobell, 2013) or Earth observation (EO) vegetation indices (e.g. Mkhabela *et al.*, 2011; Kogan *et al.*, 2013). When compared to process-based approaches, empirical models require less input data and are generally more straightforward to implement. However, since the calibration is based on historical observations, empirical models can lack validity when applied to other growth seasons, crop cultivars and locations that differ to those used to develop the statistical relationship (Fang *et al.*, 2011; Casa *et al.*, 2012; Ma *et al.*, 2013; Huang *et al.*, 2015; Lobell *et al.*, 2015).

An alternative to empirical modelling is the use of process-based crop growth models (referred to hereafter as crop models). Crop models provide a framework to link knowledge of the key biophysical mechanisms within cropland ecosystems (Casa *et al.*, 2012; Asseng *et al.*, 2013). For instance, these main processes can including soil-plant water balances integrated with existing models of leaf-level photosynthesis (e.g. Farquhar and von Caemmerer, 1982) and transpiration (Penman-Monteith equation, see Jones, 1992). The interactions between management, crop genetic traits, soil type and meteorology are mathematically described in the models, and their subsequent impacts on crop C dynamics (including development and dry-matter partitioning) are simulated Figure 1.4).

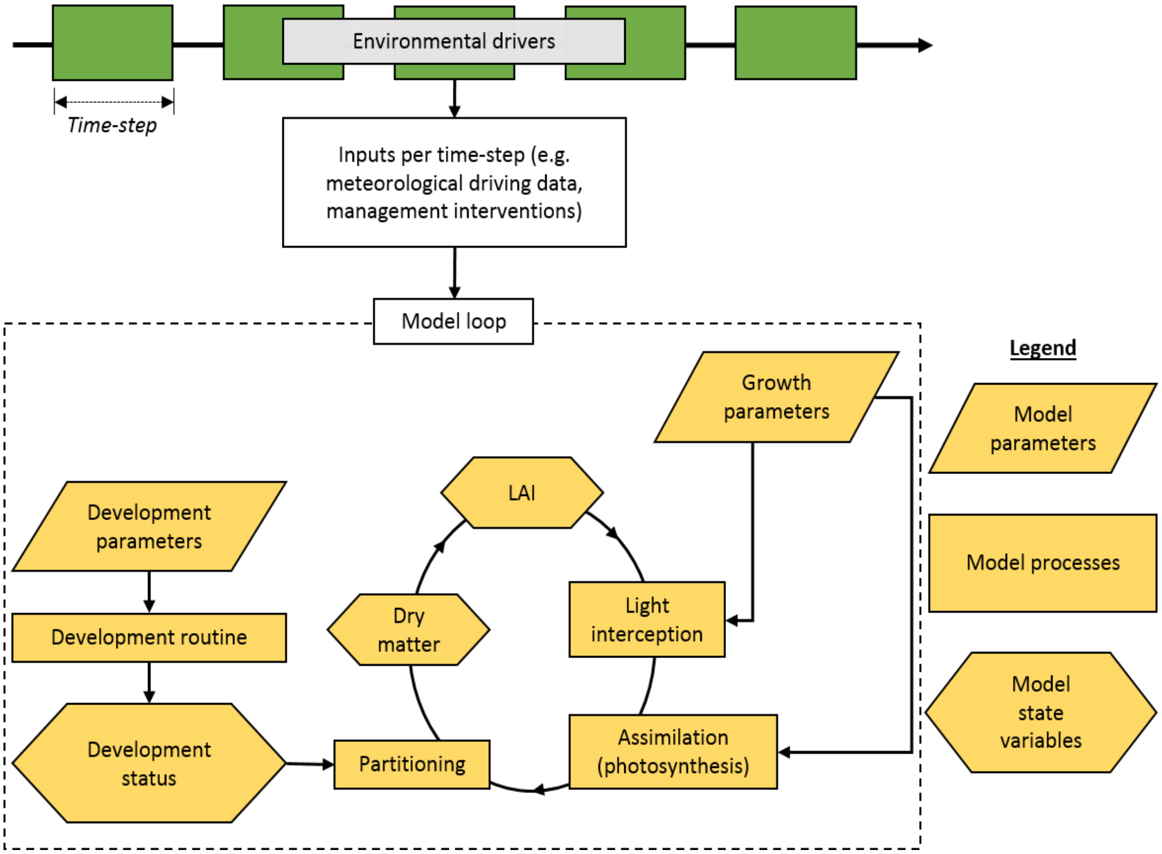

Figure 1.4: Schematic of a basic crop model structure driven by temporally frequent (half-hourly to daily) meteorological data. At each model time-step, partitioning of C is determined based on the development status and the rate of photosynthesis. The photosynthetic rate is determined by crop growth parameters and the degree of light (i.e. solar radiation) intercepted by the canopy, which is governed by the LAI and crop growth parameters. The partitioned C is allocated to the crop organs (e.g. root, stem, leaves and grain) as dry matter (adapted from: Dorigo *et al.*, 2007).

Crop models, often evaluated using EC data, are typically crop-specific (e.g. CERES-Wheat, Singh *et al.*, 2008; and SPAc, Sus *et al.*, 2010). Among the most important crop-specific parameters are those affecting the development rate; for instance cardinal temperatures and optimum photoperiod, which control the timings of key phenological stages within the vegetative and reproductive phases (Wang and Engel, 1998; Boote *et al.*, 2013). In the case of winter cereal crop development, models also incorporate the impacts of vernalisation – defined throughout this thesis as the exposure of crops to low temperatures in order to promote flowering in the following spring months (Streck *et al.*, 2003).

Since crop models account for the main vegetation and environmental processes they are generally more robust when compared to empirical approaches (Dorigo *et al.*, 2007). Additionally, in contrast to the EC method, crop models provide a more complete analysis of the crop C balance by simulating the processes (e.g. photosynthesis and respiration) that result in gains and losses of C (Boote *et al.*, 2013). And so, the models are a powerful tool for diagnosing and forecasting the seasonal variability of crop C fluxes and yield in response to climate change (Wong and Asseng, 2006; Sus *et al.*, 2010; Ciais *et al.*, 2011).

In addition to meteorological driving data, crop models often require large amounts of inputs, including that related to soil characteristics, management practices and plant traits. Due to the generally high spatial and temporal variability of these model inputs, which consequently challenges the capabilities of making direct measurements, this input data is rarely available (Launay and Guerif, 2005; Becker-Reshef *et al.*, 2010; Kogan *et al.*, 2013). Furthermore, when compared to standard land-surface models, detailed crop models – simulating complex leaf-level process over multiple canopy layers – typically require a large number of parameters (Valade *et al.*, 2013). These parameter values are often unknown, and are therefore based on expert knowledge that can be subjective (Ziehn *et al.*, 2012; Rafique *et al.*, 2015) or through model calibration using observations (Tang and Zhuang, 2009). And so, parameters uncertainty, combined with the extensive input data requirements, often limits the spatial-temporal upscaling of the models (Lobell and Burke, 2010; Xu *et al.*, 2011; Ma *et al.*, 2013; Zhao *et al.*, 2013; Huang *et al.*, 2015). However, applying crop models at regional to global extents is becoming increasing important to support management decisions on issues related to climate change (Challinor *et al.*, 2004; Bondeau *et al.*, 2007; Asseng *et al.*, 2011; Rötter *et al.*, 2012) and food security (Godfray *et al.*, 2010).

1.4. Earth observation (EO) cropland applications

1.4.1. EO data for crop monitoring

The synoptic, timely and repetitive coverage of satellite EO sensor data, including optical reflectance and radar backscatter, can provide spatially and temporally consistent information on actual crop growth over large areas (Zhao *et al.*, 2013). The exploitation of EO data covering croplands has been an active area of researched since the launch of the Multi-spectral Scanner System (MSS) on Landsat 1 in 1972, which was initially used for classifying maize and soybean producing areas (Bauer and Cipra, 1973). Continual developments in EO sensors, and associated technologies, has led to ever-increasing volumes of EO data at higher spatial and temporal resolutions. Consequently, the availability of EO data has given rise to a multitude of cropland EO applications – existing across a range of crop types and spatial scales (Delecolle *et al.*, 1992; Fritz *et al.*, 2008; Becker-Reshef *et al.*, 2010; Atzberger, 2013; Franch *et al.*, 2015). These EO applications generally include yield forecasting (e.g. Mkhabela *et al.*, 2011; Bolton and Friedl, 2013), crop condition monitoring (e.g. Zhengwei *et al.*, 2011) and crop mapping (e.g. Conrad *et al.*, 2010; Pittman *et al.*, 2010).

The wide-spread utility of EO data and methods has led to the development of gridded products that correlate with crop vegetation, including leaf area index (LAI), fraction of absorbed photosynthetically active radiation (FAPAR), soil moisture, normalised difference vegetation index (NDVI) and evapotranspiration. Most notably, NDVI (e.g. Figure 1.5) and LAI are a good indicator of crop condition and are closely related to other agronomic variables of interest, including yield, biomass, crop nitrogen uptake and water stress (Mkhabela *et al.*, 2011; Casa *et al.*, 2012). In particular, LAI (defined throughout this thesis as the one-sided leaf area per unit horizontal ground area; Campbell and Norman, 1989) is one of the most common vegetation canopy variables that are derived from EO data. EO LAI products include the eight-day LAI estimates available from the MODIS sensor at 1 km spatial resolution since the year 2000 (Knyazikhin *et al.*, 1998; Yang *et al.*, 2006).

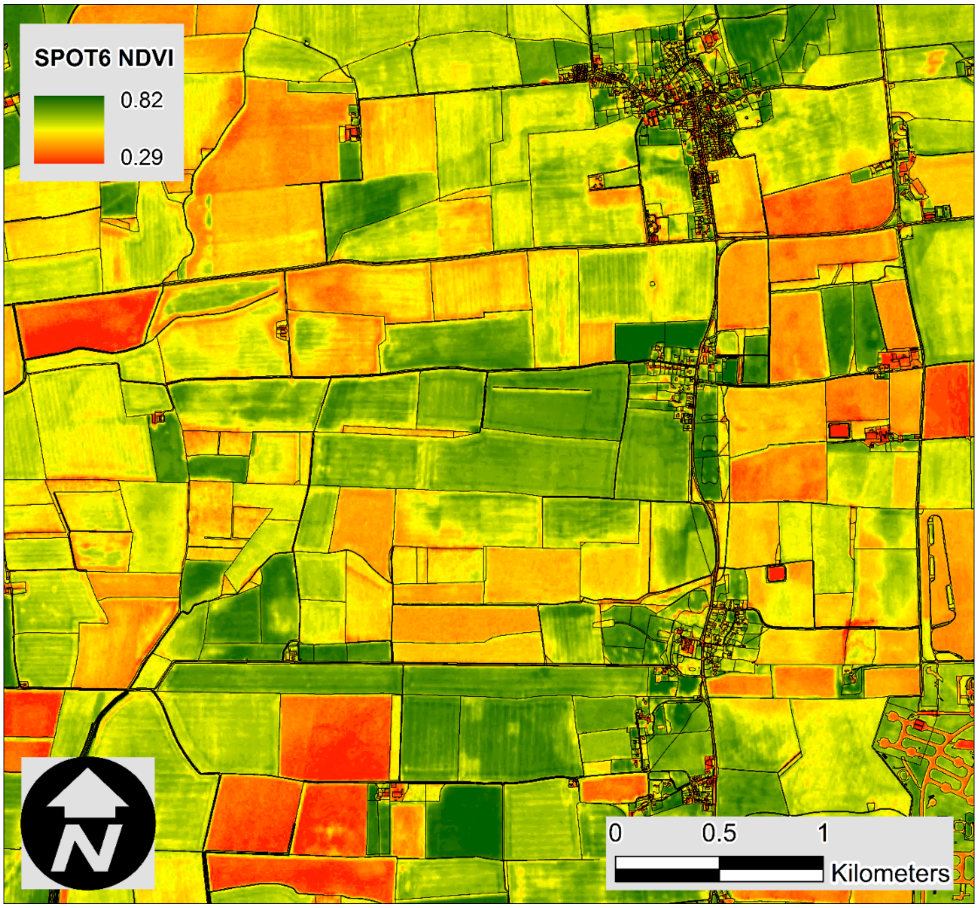

Figure 1.5: Normalised Difference Vegetation Index (NDVI) calculated from a SPOT-6 multi-spectral imagery acquisition on the 9th March 2014 covering a cropland landscape located in Lincolnshire, UK. Field boundaries are included (black lines) using the Ordnance Survey MasterMap Topographic Layer features (source of original SPOT-6 image: Airbus Defence and Space).

Past studies have investigated the direct use of EO data for estimating crop production and yields (e.g. Becker-Reshef *et al.*, 2010; Mkhabela *et al.*, 2011; Kogan *et al.*, 2013). These approaches have been based on empirical relationships between historical yield observations and reflectance-based vegetation indices. For instance, the period of maximum leaf area of cereal crops coincides with that of flowering and grain filling

(Mkhabela *et al.*, 2011), therefore yield is closely correlated with maximum LAI (Forbes and Watson, 1992; Franch *et al.*, 2015). For wheat crops, studies also demonstrate a positive linear correlation between yield and the seasonal peak NDVI (Tucker *et al.*, 1980; Mahey *et al.*, 1993; Smith *et al.*, 1995). Mkhabela *et al.* (2011) evaluated the potential of MODIS NDVI for forecasting the yields of multiple crop types and growing seasons at regional-scales. Through regression-based analysis with official crop yield statistics, this study demonstrated that MODIS NDVI can be used to predict crop yield to within ±10% of the reported yield. Similarly, Becker-Reshef *et al.* (2010) developed an empirical model for forecasting winter wheat yields in Kansas. When this calibrated model was independently validated in Ukraine, the forecasted wheat yields for the years 2001 to 2008 were also within ±10% of the official statistics when applying the model six weeks prior to harvest.

In order to capture the key developmental stages involved with crop growth, EO sensors require a high temporal resolution – including daily to weekly observations (Moulin *et al.*, 1998; Launay and Guerif, 2005). However, the use of high temporal resolution EO data is typically at the expense of a reduction in spatial resolution, defined throughout this thesis as the ground sampling distance that is within the sensor's instantaneous field of view (Lillesand *et al.*, 2008).

Previously crop monitoring studies have involved the use of moderate to coarse spatial resolution EO sensors (250 m to 1 km, e.g. de Wit and van Diepen, 2007; Xu *et al.*, 2011;

Wu *et al.*, 2012; Kogan *et al.*, 2013). Using 250 m spatial resolution MODIS data, Wardlow *et al.* (2007) discriminated individual fields that were at least 32.4 ha in size in an area located in the United States Central Great Plains region. Fritz *et al.* (2008) also demonstrated that the MODIS time-series data was suitable for mapping field sizes of around 75 ha in a dominant crop producing region in Russia. However, the use of medium to low spatial resolution sensors is typically insufficient for retrieving biophysical variables at field sizes < 25 ha (Doraiswamy *et al.*, 2004). Such field sizes are typical across the European Union (EU-28) where the average size of an agricultural holding is only 14.4 ha (Eurostat, 2013a). To resolve the spectral detail, these relatively small and fragmented fields require finer spatial resolution sensors, such as imagery available from the Landsat-8 sensor that has a pixel size of around 30 m, i.e. smaller than the average field across most of the EU-28 regions.

1.4.2. Radar EO data

The availability of sufficiently clear observations from optical sensors is challenged by the presence of cloud cover – the extent of which varies both temporally and spatially (Whitcraft *et al.*, 2015). And so, cloud obscurity can result in observations gaps in a multi-temporal analysis of crop growth. However, radar backscatter ($\sigma°$) derived from Synthetic Aperture Radar (SAR) sensors can provide fine scale observations and, using active microwave signals, they are relatively unaffected by clouds.

Where, optical sensors are sensitive to biochemical properties of crops (including chlorophyll-a), SAR sensors are more responsive to the water content and structural elements of the crop, such as the size and shape of leaves and stem (Ulaby *et al.*, 1984). Therefore, an approach that utilises data from both sensors, can be complimentary and potentially improve the estimation of crop variables (Doraiswamy *et al.*, 2005; Shang *et al.*, 2009).

Past SAR crop monitoring research has focused on the degree of SAR σ° with respect to the sensor characteristics, including the wavelength and polarisation (e.g. McNairn, 2008; Baghdadi *et al.*, 2009; McNairn *et al.*, 2009). In particular, comparisons have been made between different radar frequency bands, the majority of which have been conducted using C-band (4 to 8 GHz). Generally, higher frequencies, such as the X-band (8 to 12 GHz) and C-band, interact with the heads of crops in the upper part of the canopy; whereas lower frequencies, such as L-band (1 to 2 GHz), penetrate deeper into the canopy (Inoue *et al.*, 2002; Jiao *et al.*, 2010). Experiments in Baronti *et al.* (1993) concluded that agricultural crops were not visible at the P-band (0.25 to 0.5 GHz) frequency; however, the higher frequency C-band provided a significant amount of backscatter, even for moderate crop growth.

In addition to the waveband, the interaction of a SAR sensor signal with a crop canopy is also dependant on the horizontal and vertical structure of the target vegetation (Shang *et al.*, 2009). Therefore, investigations have also been carried out with different polarisations (i.e. orientations) of the transmitted and received signal (McNairn *et al.*, 2002). Generally, differences in the vegetation structure, through changes in crop growth, can be detected with vertically (VV) polarised signals; whereas, horizontally (HH) polarised SAR signals are less attenuated by vegetation and therefore penetrate the canopy further – providing more information regarding the soil conditions (Ferrazzoli *et al.*, 1999; McNairn and Brisco, 2004). Using a C-band SAR sensor (ERS-1), Paloscia (2002) observed that VV-polarised σ° of narrow-leaf crops (e.g. wheat) decreases with increasing biomass, whereas the σ° of broad-leaf crops (e.g. sunflowers) increases with biomass. The high attenuation rates of VV-polarised signal can partly be attributed to the predominantly vertical orientation of the stems and ears of the narrow-leaf crop structure (Ferrazzoli *et al.*, 1999). Furthermore, Ferrazzoli *et al.* (1999) found that σ° is dominated by soil early in the season and during the drying stages, whereas leaf scattering is more dominant in the middle of the season.

1.5. Integrating EO data and crop models

When compared to crop models, EO data cannot directly resolve the environmental interactions and mechanisms of crop growth dynamics. However, EO data can estimate the condition and phenology of vegetation over large areas (Xu *et al.*, 2011). And so, EO-derived data can potentially be exploited to initialise and parameterise crop models; thereby supporting their spatial and temporal upscaling (de Wit and van Diepen, 2007; Xu *et al.*, 2011). EO data can also compliment models by correcting for processes that are either incorrectly represented or not included in the model structure (Huang *et al.*, 2015). Such processes can include those relating to land management activities and disturbance events – for instance, damage caused by frost, wind, hail, disease, weeds and pests – that could lead to variability in cropland C fluxes and yield (Xiao *et al.*, 2011; Zhao *et al.*, 2013).

Several model-data fusion approaches for integrating crop models with EO data during the growing season have been reviewed (e.g. Delecolle *et al.*, 1992; Clevers *et al.*, 1994; Bouman, 1995; Fischer *et al.*, 1997; Moulin *et al.*, 1998; Dorigo *et al.*, 2007; Dente *et al.*, 2008). Generally, past studies make a distinction between model forcing and data assimilation (DA) strategies: calibration (or re-initialisation) and updating (Figure 1.6). The forcing approach involves the direct use of EO data; thus replacing the modelled value at either some or all of the time-step. A key issue with the forcing method is that the EO data are assumed to be error-free (Ines *et al.*, 2013). Furthermore, due to satellite orbital parameters and cloud cover, if replacing all of the modelled values, the EO temporal frequency is typically insufficient to match that of the model time-steps and some interpolation is necessary, which can introduce uncertainty (Dorigo *et al.*, 2007; Yuping *et al.*, 2008).

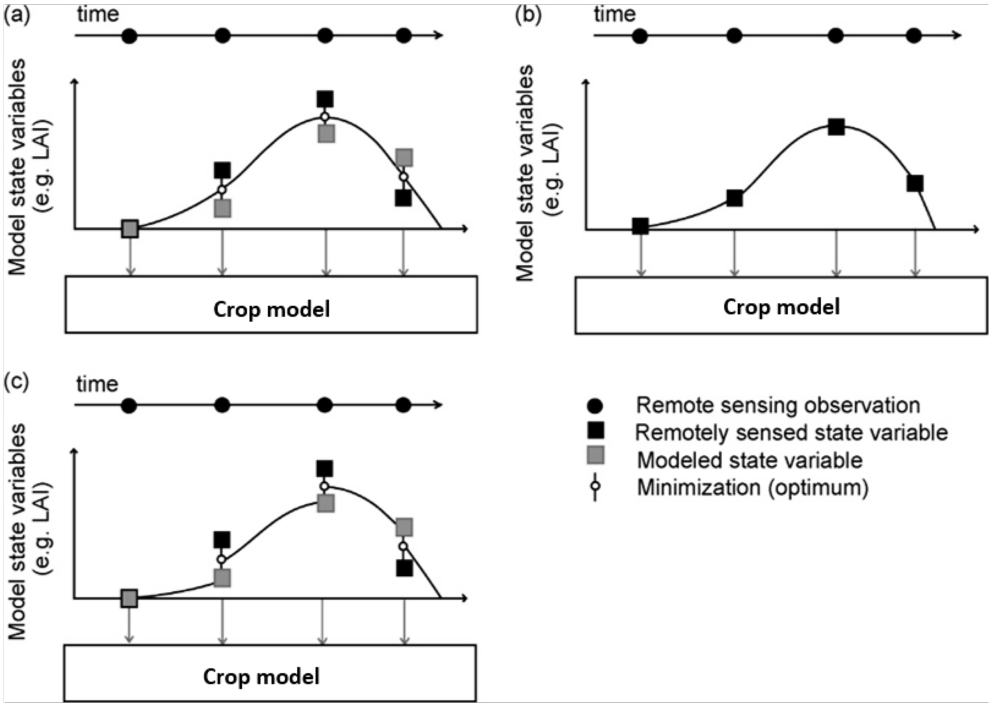

Figure 1.6: Approaches for integrating crop models with EO time-series estimates of the model state variables (e.g. LAI), including (a) calibration (or re-initialisation), (b) forcing and (c) updating (adapted from: Dorigo *et al.*, 2007).

DA methods have been applied to constrain simple models, or model components, with observations (Smith *et al.*, 2013; Luo *et al.*, 2015). The calibration DA method (also known as variational assimilation) includes re-initialising (e.g. sowing or emergence date, Brown and de Beurs, 2008; Yuping *et al.*, 2008; Sus *et al.*, 2013) or re-parameterising (e.g. canopy and growth parameters) crop models until an optimum agreement is achieved between the simulated state variables and the EO time-series estimates (Delecolle *et al.*, 1992; Bouman, 1995; Dorigo *et al.*, 2007; Ines *et al.*, 2013). For instance, Xu *et al.* (2011) optimised emergence date and minimum temperature of the WOFOST model based on

MODIS LAI for improving regional winter wheat yield estimates.

In recent years, studies have evaluated the assimilation of EO data and crop models using the updating DA approach (also known as sequential DA). This approach is based on the assumption that updating the state variable at one time-step improves the simulation accuracy at subsequent time-steps where EO measurements are unavailable (Dorigo *et al.*, 2007). Since uncertainties exist in both models and observations, updating DA algorithms aim to provide an optimum solution for combining models and observations when minimising the uncertainty of a state variable. For instance, the ensemble Kalman Filter (EnKF, Evensen, 2003) algorithm assigns the relative weight of the model and observation uncertainty in the calculation of updated state estimates. And so, accurately determining the uncertainty in models and observations is of fundamental importance when applying the sequential DA algorithm (Williams *et al.*, 2005; Zhao *et al.*, 2013).

Among the updating DA algorithms used for integrating EO data and crop models (e.g. particle filter, Kalman Filter) the EnKF algorithm is one of the most widely used (Ines *et al.*, 2013). The EnKF is based on Bayes' theorem where new observations are used to update the probability of an estimate. The algorithm represents the model and observation uncertainty with a Monte Carlo ensemble (i.e. probability distribution) around the mean state variable. The EnKF then produces a probabilistic estimate of the state variable by combining the forecasted and observed values.

Past studies, have used the EnKF for providing sequential updates of LAI with the aim of improving estimates of yield (Ines *et al.*, 2013; Zhao *et al.*, 2013; Li *et al.*, 2014; Huang *et al.*, 2016) and net C fluxes (e.g. Revill *et al.*, 2013, see Chapter 2; Sus *et al.*, 2013). Zhao *et al.* (2013) demonstrated the EnKF algorithm for coupling MODIS LAI and the pyWOFOST model and successfully reducing errors in maize yield estimates at 22 (out of 24) sites located in China. In particular, with the assimilation of LAI, Zhao *et al.* (2013) achieved improvements in yield estimates at sites that were exposed to adverse meteorological conditions. Research in de Wit and van Diepen (2007) investigated the assimilation of soil moisture; specifically, the EnKF was applied to assimilate soil water index estimates to reduce uncertainties in the WOFOST model regional-scale maize yield estimates. Although assimilating soil moisture improved estimates for the majority of regions, the course-scale (~ 25 km) scatterometer derived data used by de Wit and van Diepen (2007) was unable to resolve small-scale land management practices – notably irrigation systems. Ines *et al.* (2013) applied the EnKF to assimilate AMSR-E soil moisture and MODIS LAI into the DSSAT-CSM-Maize model for simulating multi-annual (2003-2009) yields in Story County in the United States. When compared to observations, only slight improvements were achieved when assimilating the LAI and soil moisture independently. However, the yield estimates improved more when LAI and soil moisture were assimilated simultaneously.

1.6. Thesis overview and key research questions

The overarching aim of this thesis is to address the challenges associated with the spatial upscaling of crop models – in particular the limitations due to parameter uncertainty, model complexity and input data requirements. Four key interrelated research chapters (Chapters 2, 3, 4 and 5) evaluate approaches that could support the scaling (from fields to regional extents) of crop C budget models (Figure 1.7).

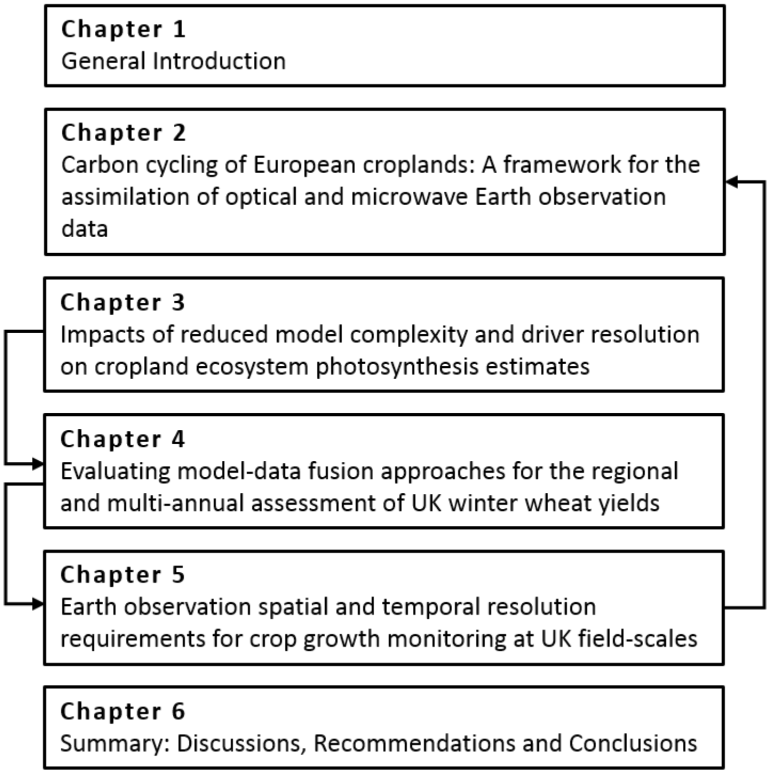

Figure 1.7: Structure of thesis with arrows indicating links between chapters.

Chapter 2 describes the assimilation of EO-derived LAI estimates, using the EnKF DA algorithm, for sequentially updating the Soil-Plant-Atmosphere crop (SPAc) model of crop development and C fluxes. Data from high spatial resolution (20-30 m) optical and radar EO sensors are used to empirically retrieve LAI estimates within the winter wheat growing seasons at six European field sites. The performance of SPAc (both with and without the DA) for estimating LAI, NEE and yield is evaluated using field-scale observations of C stocks and fluxes. The key research questions addressed are:

1) To what extent can the assimilation of EO-derived LAI improve the NEE flux estimates of winter cereal crops at the field-scale?

2) Is the model DA framework valid for multiple European cropland sites?

Chapter 3 determines the impacts of reduced model complexity and driver resolution when simulating winter cereal crop photosynthesis. The simplified Aggregated Canopy Model (ACM) was used to simulate daily photosynthesis using minimum driving data. ACM is calibrated based on estimates from the detailed SPAc model, which simulates leaf-level processes at half-hourly time-steps across multiple canopy layers. The calibrated ACM outputs are compared to SPAc and independent photosynthesis estimates, which were derived from EC data. Both models are also evaluated when driven by local and gridded meteorology data to answer the following research questions:

3) How does model complexity influence estimates of photosynthesis?

4) How do single-site and multi-site photosynthesis calibrations compare across European field sites?

5) How do the complex and simple model photosynthesis estimates compare when driven by gridded atmospheric re-analysis data?

Chapter 4 uses a novel model-data fusion framework for the regional and multi-annual

(2000-2013) assessment of UK winter wheat yields. Spatial datasets delineating wheat growing areas are used to extract 8-day 1 km MODIS LAI. The relationship between the MODIS LAI and official regional yield statistics was quantified. The use of MODIS LAI for constraining the crop model yield estimates was also evaluated using the yield data.

6) What is the empirical relationship between MODIS LAI and crop yields across UK regions?

7) What is the accuracy of grid-scale crop model yield estimates when aggregated to regional-scales?

8) Can MODIS LAI be used to constrain and improve the model estimates of yield?

Chapter 5 quantifies errors associated with the spatial and temporal resolutions of optical EO sensors when resolving crop growth at UK field-scales. Fine-scale (5 m) images were spatially aggregating to simulate a continuum of images from medium to coarse-scale EO sensors. To approximate errors due to spatial resolution, per-field samples were extracted from the aggregated datasets and compared to that from the fine-scale image. Temporal resolution errors were estimated by removing LAI estimates from a daily LAI dataset – generated using a crop model – in order to mimic the temporal resolution of current EO sensors. LAI values were further removed on potentially cloudy days. The filtered LAI time-series are then statistically compared to the original LAI time-series. The quantified errors were used to solve the questions:

9) What is the minimum EO sensor spatial resolution required to monitor crops at field-scales that are characteristic of UK agriculture?

10) How does temporal resolution and likely cloud cover influence the effectiveness of optical EO sensors for tracking winter wheat crop growth over a cropland landscapes?

11) What are the expected benefits of the dual Sentinel-2 constellation (i.e. Sentinel-2A and 2B) for multi-temporal crop monitoring at UK field-scales?

CHAPTER 2

Carbon cycling of European croplands: A framework for the assimilation of optical and microwave Earth observation data

Declaration

The research presented in Chapter 2 has been adapted from a paper that was published in the journal *Remote Sensing of Environment* on the 12th July 2013. Andrew Revill was the first author of the paper with co-authors: Oliver Sus, Brian Barrett and Mathew Williams (see Revill *et al.*, 2013). Specifically, the modelling approaches were evaluated by A. Revill with support from O. Sus and M. Williams. A. Revill processed the Earth observation data with recommendations from B. Barret. A. Revill wrote the manuscript with edits from M. Williams and suggested inputs from all other authors. Further paper comments were received from Mathias Disney of the University College London.

2.1. Introduction

Agricultural intensification over the past 40 to 50 years, achieved by 'Green Revolution' technologies and an increase in cropland area (Foley *et al.*, 2005), has resulted in an approximate doubling in worldwide cereal production between 1970 to 2010 (FAO, 2015). Through changes to carbon (C) storage and emissions – associated with management activities – croplands also provide opportunities for climate change mitigation (Smith *et al.*, 2007; Power, 2010; Zhang *et al.*, 2015). In 2012, around one quarter (24.7%) of the European Union (EU-27) land area was occupied by croplands (Eurostat, 2013). This land area presents a mosaic of crop cultivars, phenological stages and growth periods due to spatio-temporal variations in soil and climatic conditions. In the EU, spatial variability in regional-scale crop growth and production is further driven by changes in the Common Agricultural Policy. These environmental and policy changes result in a broad range of cropland management techniques (e.g. tilling intensity, use of fertilisers and irrigation) causing uncertainty when generalising the impact of specific activities on crop C budgets (Osborne *et al.*, 2010).

There is considerable uncertainty involved in quantifying C dynamics, particularly when identifying whether, and under what conditions, landscapes act as sources or sinks of C (Quaife *et al.*, 2008). Flux towers can provide measurements of the net ecosystem exchanges (NEE) at local scales (~1 km^2) via the eddy-covariance (EC) technique (Baldocchi, 2003). However, complex terrain and heterogeneous spatial distributions of vegetation within the sensor ‘footprint’ undermine the assumptions of the EC technique, which introduces measurement uncertainty (Hollinger and Richardson, 2005). Globally the tower sites are also sparsely distributed and data-gaps are always present. Where EC towers provide direct measurements of the net land-atmosphere CO_2 exchanges only, a more complete analysis of crop C dynamics and yield relies on simulations using process-based crop models (Jones *et al.*, 2003; Boote *et al.*, 2013; Zhang *et al.*, 2015), which are often linked to C flux observations for validation. The models require reliable input parameters, including management interventions, plant traits, soil properties and meteorological driving data at points within the model domain. Therefore parameter estimates are the largest source of model uncertainty (Launay and Guerif, 2005) and a particular challenge is to derive these parameters across the model spatial and temporal extents.

Earth observation (EO) data can be combined with models to provide objective updates of state variables describing crop condition over landscape scales. This model-data fusion can be achieved via data assimilation (DA) algorithms that are based on the assumption that estimates from neither observations nor models are perfect but a combination of the two, weighted by a specified uncertainty, will produce more realistic model updates (Williams *et al.*, 2005). Research has demonstrated how DA can link regional-scale models with moderate to coarse spatial resolution EO sensors (250 m to 1 km, e.g. de Wit and van Diepen, 2007; Xu *et al.*, 2011; Wu *et al.*, 2012; Kogan *et al.*, 2013; Huang *et al.*, 2016). These sensors have high temporal resolutions – from daily to weekly time-scales –

that are suitable for capturing the key developmental stages of crop growth (Launay and Guerif, 2005; Whitcraft *et al.*, 2015a). However, the spatial resolution of these sensors is typically insufficient for retrieving biophysical variables at field sizes less than 25 ha (Doraiswamy *et al.*, 2004), such as fields that are characteristic of European croplands. These smaller fields require higher spatial resolution sensors (e.g. < 20 m, SPOT 2–6). However, the use of high resolution EO sensors is typically at the expense of a lower temporal resolution – potentially leading to gaps in acquisitions during critical growth stages. The presence of clouds (i.e. cloud cover obscurity) can also affect the availability of suitable optical EO imagery (Whitcraft *et al.*, 2015b); thus resulting in further reductions in the number of observations. The spatial/temporal resolution trade-off, compounded with the issue of cloud cover obscurity, can partly be addressed by using Synthetic Aperture Radar (SAR) sensors. SAR provide high resolution data and, since they operate using microwave energy, SAR sensors are relatively unaffected by cloud cover. Furthermore, where optical EO sensors are sensitive to the biochemical properties of crops, SAR sensors are more responsive to the water content and structural elements of the vegetation, such as the size and shape of leaves (Shang *et al.*, 2009).

In this research we demonstrate a framework for the assimilation of leaf area index (LAI) estimates, retrieved from optical and SAR EO sensors, to update the LAI simulated by a cereal crop model of C dynamics over European croplands. Our specific objectives were to: first, determine the potential of a DA technique for improving the simulated daily NEE fluxes, along with the at-harvest cumulative NEE, of winter wheat crops at the field-scale.

The accuracy of the DA, when assimilating optical and SAR LAI estimates individually and synergistically, is evaluated by comparing model outputs to independent observations from flux towers at European sites. Second, establish if the same methodology (including model calibrations) is applicable for improving the relationship between the simulated and observed values at multiple European field sites; thereby providing a proof-of-concept for future spatial upscaling activities. And so, we address the following research questions:

1) To what extent can the assimilation of EO-derived LAI improve NEE flux estimates of winter cereal crops at the field-scale?
2) Is the model DA framework valid for multiple European cropland sites?

Innovations of this study include the sequential assimilation of data derived from both optical and SAR high spatial resolution EO sensors, thus increasing the number of within-season observations. It is hypothesised that the multi-sensor approach improves the model performance at the field-scale by more effectively tracking the canopy development of cereal crops, which is critical for seasonal C balances (Sus *et al.*, 2010).

2.2. Data and Methods

This section first presents an outline of the study sites and data for driving and validating the model framework. Second, a description of the pre-processing and LAI retrieval approaches applied to the EO data are provided. Third, a brief overview of the SPAc model is given along with details on the DA algorithm implemented in this research.

2.2.1. Study sites and data

This study investigates one winter wheat (*Triticum aestivum*) growing season at six different European field sites (Figure 2.1); located in France (Auradé, Lamasquère and Grignon), Germany (Klingenberg and Gebesee) and Switzerland (Oensingen). These specific crop sites and seasons were selected as they were also used by Sus *et al.* (2010) in the development of the crop C cycle model used in this study; thereby allowing comparisons to this previous research.

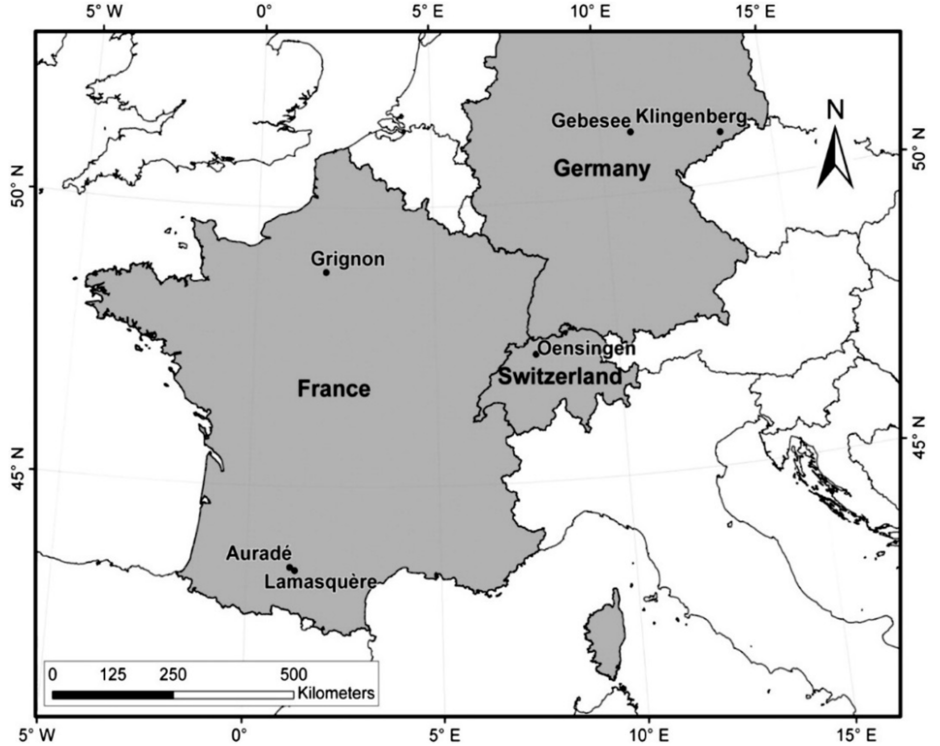

Figure 2.1: Map showing the locations of six European winter wheat crop sites/seasons.

As well as different management techniques, the sites vary in latitude (43.5-51.1°N) and longitude (1.1-13.5°E) and show significant variations in temperature (annual average 6 to 11 °C) and precipitation (mean annual values from 327 to 1051 mm). Consequently, the sites had different growing periods, in terms of both the sowing and harvest date and the overall length of the growing season (i.e. sowing to harvest) – ranging from 245 to 346 days. Field sizes also varied from 1.5 to 97.6 ha (Table 2.1), and the terrain across each field site can be considered level to very gently sloping.

Table 2.1: List of study sites and meteorological observations between sowing and harvest, including growth period length (from sowing to harvest), average temperature (Av. temp.) and precipitation (Precip.) for winter wheat crop seasons covering years from 2005 to 2007. Also included are the number of multi-temporal SPOT-2/4 and ERS-2 EO scenes that were available for this analysis.

Site	Field size (ha.)	Sowing date	Harvest date	Period (days)	Av. temp. (°C)	Precip. (mm)	SPOT 2/4 scenes	ERS-2 scenes
Auradé	22.35	27.10.05	29.06.06	245	9.7	374	3	4
Grignon	19.45	21.10.05	15.07.06	267	8.2	327	3	3
Lamasquère	12.11	18.10.06	15.07.07	270	11.3	531	5	5
Klingenberg	97.60	25.09.05	06.09.06	346	6.0	607	3	6
Oensingen	1.50	19.10.06	16.07.07	270	10.2	1051	0	6
Gebesee	93.50	09.11.06	07.08.07	271	10.6	447	4	4

For each of the cropland sites, data was sourced from the Global FLUXNET database (fluxnet.ornl.gov), which included EC daily NEE flux tower measurements made throughout the growing seasons. The NEE datasets consisted of aggregates of half-hourly observations. Gap-filling was applied to the original data using the Marginal Distribution Sampling method (Reichstein *et al.*, 2005). However these datasets were filtered such that only days comprising of aggregates of original data (i.e. days consisting of 48 observations without gap-filled estimates) were used in this analysis, consequently between 15% and 45% of the values were rejected.

Meteorological observations collected at each site, used to drive the crop C cycle model, included half-hourly radiation, temperature, wind speed, humidity and precipitation. Cartographic information detailing the physical extents of the FLUXNET field sites were digitised and subsequently used in the processing and extraction of EO data. Additional site information, recorded at dates during the crop growing seasons, included soil texture data (i.e. clay/sand ratio), site management (e.g. sowing/harvest dates and applied fertilisers), crop yield and LAI. These LAI observations, used to evaluate the model performance and to calibrate the EO LAI retrieval algorithms, were available for all sites except for Gebesee.

2.2.2. Earth observation LAI retrieval

Earth observation data and pre-processing

A total of 18 SPOT (Satellite Pour l'Observation de la Terre) cloud-free images and 28 ERS-2 (European Remote Sensing) SAR scenes (PRI data format) were sourced from

ESA under a Category-1 agreement. The specific EO scenes were selected to cover all study sites and growing seasons (Table 2.1). The level-2A processed SPOT images consisted of a combination of SPOT-2 and SPOT-4 data. The multi-temporal SPOT scenes were sourced for the growing seasons at all sites with the exception of Oensingen where sufficiently cloud-free images were unavailable. Each SPOT scene had a spatial resolution of 20 m and included multi-spectral measurements, centred on green (500–590 nm), visible red (610-680 nm) and near-infrared (790-890 nm) wavelengths.

For each site, pre-processing of the SPOT scenes included applying a geometric correction to one scene. Using the Universal Transverse Mercator (UTM) coordinate system, this process involved correcting the image to within one SPOT pixel (20 m), using the digitised field boundaries and the nearest-neighbour resampling algorithm. Using the single-date geo-referenced scene, image-to-image geometric registration was then applied to the remaining multi-temporal images.

For each pixel (p), the SPOT image pixels were converted from the raw radiometric digital numbers (DN) to top-of-atmosphere radiance (L) for each spectral band (b) using the absolute radiometric calibration coefficients (i.e. GAIN and BIAS) available in the imagery metadata:

$$L_{\mathrm{b(p)}} = \frac{DN_{\mathrm{p}}}{GAIN_{\mathrm{b}}} + BIAS_{\mathrm{b}} \qquad \text{Equation 2.1}$$

The time-series of images for each site were normalised to reduce the effects of variable sun angle, which involved dividing the pixel values by the sine of the solar elevation angle, which was also reported in the image metadata. Since the field sites were relatively flat, no further corrections were applied to reduce the differences in scene illumination due to the slope of terrain relative to the solar elevation and azimuth (as applied in Chapter 5).

Atmospheric normalisation was applied to correct for spectral differences due to variable atmospheric conditions across the SPOT imagery time-series. Due to the absence of field-based atmospheric data, the relative image-based correction technique of pseudo-invariant targets was applied (Lu *et al.*, 2002). For each field site, this correction procedure first involved normalising all images to a standard reference scene, which was chosen as the most cloud-free image. Second, using the criteria outlined in Eckhardt *et al.* (1990), surface features with a spectral reflectance signal, which were assumed to be constant throughout a crop growth season (hence invariant targets), were selected. These features included man-made structures, such as car parks and roof tops, and inland water bodies. Once the target features were identified in the reference scene, based on the spectral differences in the target features in the reference scene, the remaining scenes were corrected band-by-band.

Pre-processing of the ERS-2 SAR (C-band; VV-polarisation) data included deriving the backscatter coefficient ($\sigma°$), expressed in decibels (dB), by using the processing steps described in Laur *et al.* (2004) that are accurate to within ± 0.4 dB. This process includes corrections for range spreading losses, application of absolute calibration constants and terrain corrections to derive local incident angle using the SRTM (Shuttle Radar Topography Mission) digital elevation model. Similarly to the SPOT scenes, the ERS data were also geometrically registered to UTM, to match the boundaries of the cropland sites to within one ERS-2 pixel (12.5 m).

LAI retrieval from EO data

Simplified empirical retrieval algorithms were used for estimating LAI from the EO data. The mean within-field reflectance value, with pixel sample sizes between 226 (Grignon) to 695 (Klingenberg), was extracted from the SPOT scenes for each band and used to calculate the Weighted Difference Vegetation Index (WDVI, Clevers, 1988; 1991). The WDVI is an orthogonal index used to reduce the effect of soil reflectance, which influences the relationship between the scene reflectance and LAI. This relationship is specifically related to moisture, as reflectance decreases with increasing soil moisture content. However this decrease is independent of wavelengths between 400 and 1000 nm (Clevers, 1988). For each SPOT scene, the WDVI was calculated using:

$$WDVI = R_{\mathrm{NIR}} - \gamma . R_{\mathrm{VIS}} \qquad \text{Equation 2.2}$$

The R_{NIR} and R_{VIS} parameters correspond to the reflectance values in the near-infrared and visible red sensor wavebands, respectively. The ratio of reflectance in the near-infrared and visible red wavebands ($R_{\mathrm{NIR}}: R_{\mathrm{VIS}}$) for bare soil (i.e. before crop emergence) is shown as γ. Across all cropland sites the γ value ranged from 0.75 to 1.98.

The LAI was then retrieved based on a linear relationship between all WDVI and the ground measured LAI at all sites. Therefore, a single calibration was determined from this regression approach that could be used to estimate LAI from WDVI for all sites; thus allowing for the potential use in further spatial upscaling studies of European croplands:

$$LAI = m.WDVI + c$$ Equation 2.3

where m and c (calibrated as m = 0.23, c = -1.57) are the slope and intercept coefficients of the linear fit between the WDVI and LAI. This calibration involved matching each WDVI measurement to an in-situ LAI measurement made on a date that approximately corresponded to the SPOT acquisition. A sensitivity analysis was carried out to investigate any temporal disparity in canopy development between the measured LAI and SPOT WDVI dates to within ±10, ±7 and ±5 days. It was found that the inclusion of more measurements from accepting temporal difference of ±10 days reduced the root-mean-square error (RMSE) of SPOT estimated LAI compared to ground measurements from 0.70 (±5 days) to 0.24 (±10 days), with the corresponding negative bias being less than 1.31 $m^2 m^{-2}$ in both cases.

The mean within-field σ° value was extracted from the calibrated ERS scenes. The number of pixels used in this averaging procedure depended on the size of the field sites and varied significantly from 49 (Oensingen) to 4845 (Gebesee). The LAI values were then estimated from this mean σ° by empirically modelling the relationship between σ° and the corresponding measured LAI value ±10 days of ERS acquisition dates.

2.2.3. Ecosystem model and assimilation

Ecosystem model description

The C cycle was simulated at the cropland sites using the Soil-Plant-Atmosphere (SPA) model (Williams *et al.*, 1996; 2001), with modifications for C allocation (Williams *et al.*, 2005) and croplands (Sus *et al.*, 2010). SPA simulates the ecosystem C cycle and water-balance at the point-scale over fine temporal (half-hourly) and vertical scales (ten canopy and twenty soil layers) using half-hourly drivers: air temperature (°C), wind speed (m s^{-1}), shortwave radiation (W m^{-2}), vapour pressure deficit (hPa) and precipitation (mm). The model integrates leaf-level processes including photosynthesis, using the Farquhar model (Farquhar and von Caemmerer, 1982), and transpiration, determined using the Penman-Monteith equation (see Jones, 1992). These two processes, scaled up to make canopy-scale predictions, are linked to a radiative transfer scheme – tracking absorption, reflectance and transmittance of direct and diffuse irradiance. Furthermore, photosynthesis and transpiration are linked at leaf-level by a model of stomatal conductance. The stomatal conductance is varied to optimise C uptake, but also to maintain leaf water potential above a minimum value, explicitly linking vapour phase losses with hydraulic transport.

Sus *et al.* (2010) applied modifications to SPA in order to develop SPA v2-Crop (referred to henceforth as SPAc), which involved defining a crop-specific C partitioning scheme based on empirical observations of crop growth cycles (Penning de Vries *et al.*, 1989). This C partitioning scheme describes the fraction of assimilated C that is allocated amongst the roots, leaves, stem and storage (i.e. grain) organs as a function of development stage. The development stage is calculated as the accumulation of daily development rates, which is a function of temperature, photoperiod and vernalisation (until emergence, Streck *et al.*, 2003). SPAc has previously been tested and parameterised by Sus *et al.* (2010) over the same European FLUXNET sites/seasons used in this analysis (see Appendix section A1 for the specific SPAc parameters used for winter wheat).

Assimilation algorithm

By assimilating the EO-derived LAI, the model can propagate these estimates throughout the model state vector, according to error covariance, and forward to subsequent time-steps when EO data is unavailable. The ensemble Kalman Filter (EnKF, Evensen, 2003) DA algorithm was used to produce a probabilistic estimate of LAI by combining the forecasted and observed values, which are weighted according to the relative uncertainty assigned to the modelled and EO LAI estimates. This updated LAI is then used to update the full model state vector, which consisted of all the above and below ground biometric variables. The EnKF approach represents the model and observation error statistics with a Monte Carlo ensemble (i.e. probability distribution) of state variables, where the mean of the ensemble is the best estimate and the error covariance is determined by the variance of the state variables. For each ensemble member the basic analysis steps for the EnKF can be written as:

$$A^{\mathrm{a}} = A^{\mathrm{f}} + P_{\mathrm{e}} H (H P_{\mathrm{e}} H^{\mathrm{T}} + R_{\mathrm{e}})^{-1} (D - HA) \qquad \text{Equation 2.4}$$

where A^{a} represents the analysed state vector updated by the forecasted state A^{f}. P_{e} and R_{e} represent the model and observation covariance matrices. H is the observation operator, which consists of a probability matrix that relates the model state vector to the data, and $(D - HA)$ represents the innovation vectors.

Ecosystem model setup and determination of uncertainty

Initial simulations with the SPAc model were undertaken without DA (referred to henceforth as the ‘forward mode’) using only the input vegetation, soil parameters and meteorological driver data available for each site. A detailed overview of the parameters fitted in SPAc, along with nominal values and references, can be found in Sus *et al.* (2010) and Appendix Section A1. Experimentation was then carried out using the EnKF algorithm (referred to hereafter as ‘EnKF DA’) to assimilate the EO-derived LAI into SPAc at time-steps corresponding to 12 noon on the same day as the EO acquisitions (i.e. no other assimilations were performed on the remaining 23 hours of the day).

As the EnKF technique is based on the assumption that both SPAc and EO data are uncertain descriptions of the cropland ecosystem processes, it was necessary to quantify the uncertainties of the model and EO-derived LAI. Ideally, observation error variances are detailed in the instrument specifications (Williams *et al.*, 2005). However, the pre-processing techniques applied to retrieve the SPOT and ERS LAI estimates, including geometric, atmospheric and radiometric corrections, would have introduced additional uncertainty into the EO data (Quaife *et al.*, 2008). Therefore, EO data uncertainty was estimated individually for SPOT and ERS based on the random error (i.e. R^2) between ground measured LAI and the LAI derived from the empirical analysis – calculated as 38% and 24% for the SPOT and ERS data, respectively. The model variance was then quantified by an iterative procedure where the prescribed value was adjusted until at least 68% of the ground measured LAI were within ±1 standard deviation of the SPAc daily LAI estimates with the EnKF DA (Williams *et al.*, 2005).

The influence of the EnKF ensemble size that represented the mean LAI values was evaluated by assessing the outputs from using 50, 100 and 250 members based on the RMSE between the observed and modelled daily NEE. It was found that an ensemble size of 50 members reduced the RMSE between observed and modelled NEE with little or no improvements noticed beyond this size. This observation is also consistent with the study by Sus *et al.* (2013) for the assimilation of MODIS LAI and with de Wit and van Diepen (2007) for the assimilation of soil moisture estimates. Therefore, the EnKF experiments were carried out using model outputs from 50 members only.

Comparisons were carried out between the LAI values simulated by SPAc – both in the forward model and the EnKF DA – to the ground measurements of LAI available at each site. Further experimental analysis was conducted to assess the DA of EO measurements for improving the simulation of daily C fluxes, at-harvest cumulative NEE and yield at each site, including the assimilation of ERS LAI and SPOT LAI estimates both synergistically and individually, by comparison to independent EC data.

2.3. Results

This section first presents the results from retrieving LAI estimates from the EO data. Second, an evaluation of the SPAc model is given – both in the forward model and the EnKF DA – for the simulation of LAI, NEE and yield when compared to the FLUXNET site data.

2.3.1. LAI retrieval results

There was a reasonable correlation ($R^2 = 0.62$, $P < 0.05$, Standard Error = 0.11 $m^2 m^{-2}$) between all multi-temporal WDVI values at Auradé, Grignon, Lamasquère and Klingenberg with the corresponding (within ±10 days) ground measured LAI values (Figure 2.2a). For the remaining sites SPOT imagery was either unavailable (Oensingen) or ground measured LAI was not recorded (Gebesee). Overall, the LAI derived from the WDVI (RMSE = 0.60) showed a slightly negative bias when compared to measured values with a mean bias (i.e. mean SPOT LAI minus ground measured) of -0.05 $m^2 m^{-2}$. However, the mean error for Klingenberg (0.87 $m^2 m^{-2}$) had a much stronger positive bias when compared to the other sites.

A strong exponential relationship ($R^2 = 0.76$, $P < 0.05$, Standard Error = 0.06 $m^2 m^{-2}$)

existed between all mean ERS σ° values and ground LAI measurements within ±10 days of the ERS acquisition (Figure 2.2b). Using the coefficients (*A* and *B*) calibrated from this exponential fit the LAI was then estimated:

$$LAI = A^{B.\sigma^{\circ}} \qquad \text{Equation 2.5}$$

where A = 0.087 and B = -0.257. As was the case with the WDVI calculation, this exponential fit was determined globally between all σ° and measured LAI values.

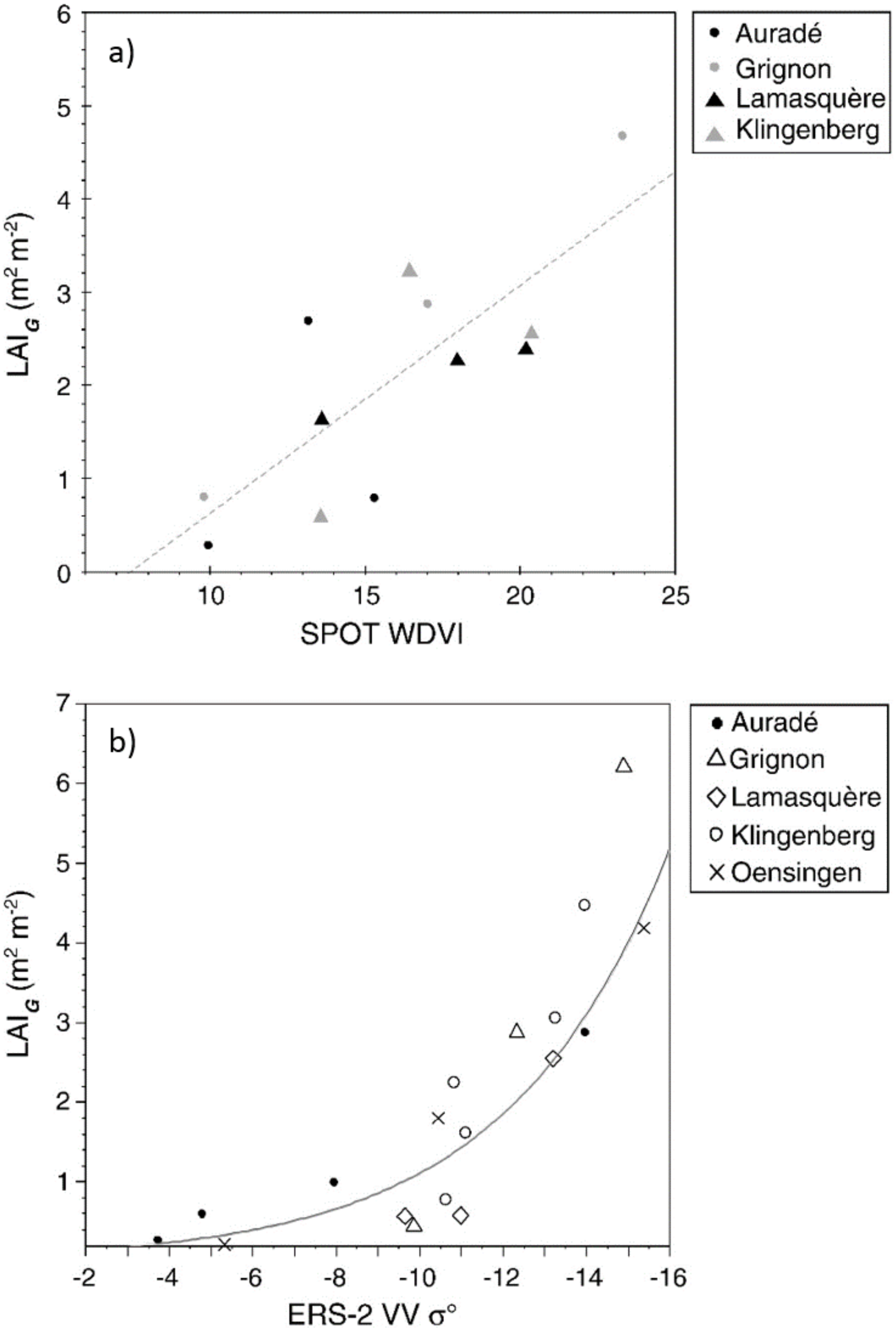

Figure 2.2: Regression of ground measured LAI (LAI_G) against a) SPOT WDVI (dashed grey line) and b) ERS-2 σ° (solid grey line).

Overall, the LAI values retrieved from the ERS σ° using Equation 2.5 were overestimated, with a mean bias of 0.15 $m^2 m^{-2}$ (RMSE = 0.54), compared to measured LAI. The LAI and σ° relationship weakens and becomes negatively biased with decreasing σ° below around -14 dB (Figure 2.2b). This change is significant for Grignon, where the σ° is -14.8 dB, and the estimated LAI value is around 1.6 $m^2 m^{-2}$ less than that of the measured.

2.3.2. Ecosystem model results: forward mode

Some clear differences in the magnitude of the SPAc simulated peak LAI values in the forward mode can be seen when compared to the ground data (Figure 2.3). Particularly, this can be seen for Auradé where the simulated LAI is overestimated by 1.3 $m^2 m^{-2}$ and Grignon where the LAI is underestimated by 1.6 $m^2 m^{-2}$.

The overall timings of the peak LAI in the forward mode simulation generally matched the ground measured LAI. The exception was Klingenberg, where the simulated peak LAI value was around 25 days later than the ground measurements. However, this apparent discrepancy in timing could be due to a lack of field measurements around the time of maximum LAI.

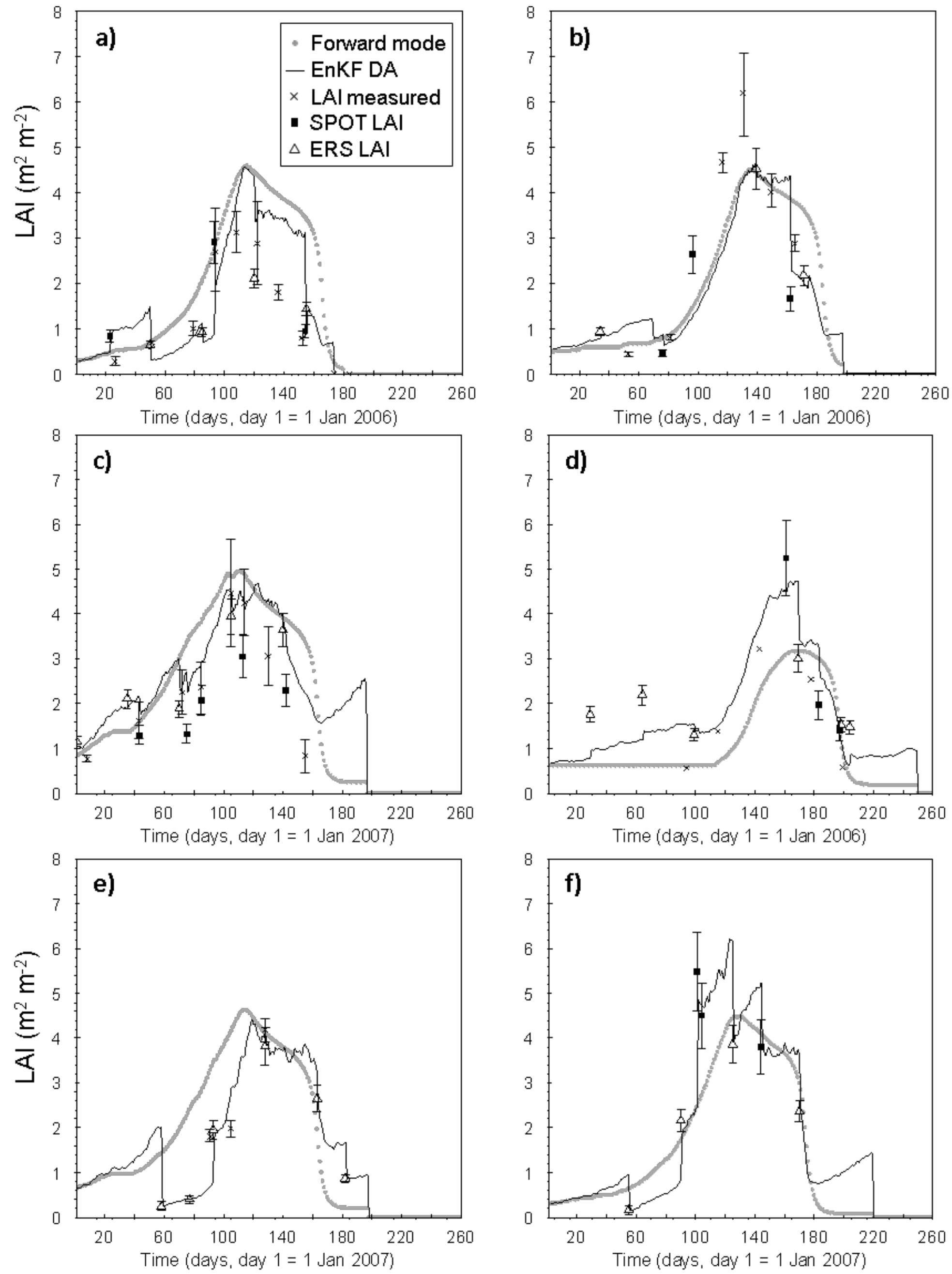

Figure 2.3: Modelled time-series LAI plots in the forward mode (grey dots) compared to EnKF DA of all EO LAI estimates (black line) for sites a) Auradé, b) Grignon, c) Lamasquère, d) Klingenberg, e) Oensingen and f) Gebesse. Including ground measured LAI and EO-derived LAI values with error bars showing the standard deviation. Note: No standard deviation of the ground measured LAI was reported for Klingenberg.

The overall seasonal trends and timings of the observed NEE fluxes of the crops were reproduced by SPAc in the forward mode simulation (Figure 2.4). For all sites there is a progressive decrease in NEE – from early in the season onwards – in response to an increase in C uptake (i.e. increase in sink strength) as the crops develop. The date of minimum NEE (i.e. peak C uptake) varies between different sites ranging from early May (Auradé (a), Lamasquère (c) and Oensingen (e)) to early-mid June (Klingenberg (d)). After the maximum C uptake the observed and simulated values show a relatively sharp increase in NEE, corresponding to crop maturity, and become a net source of C at or around the harvest date.

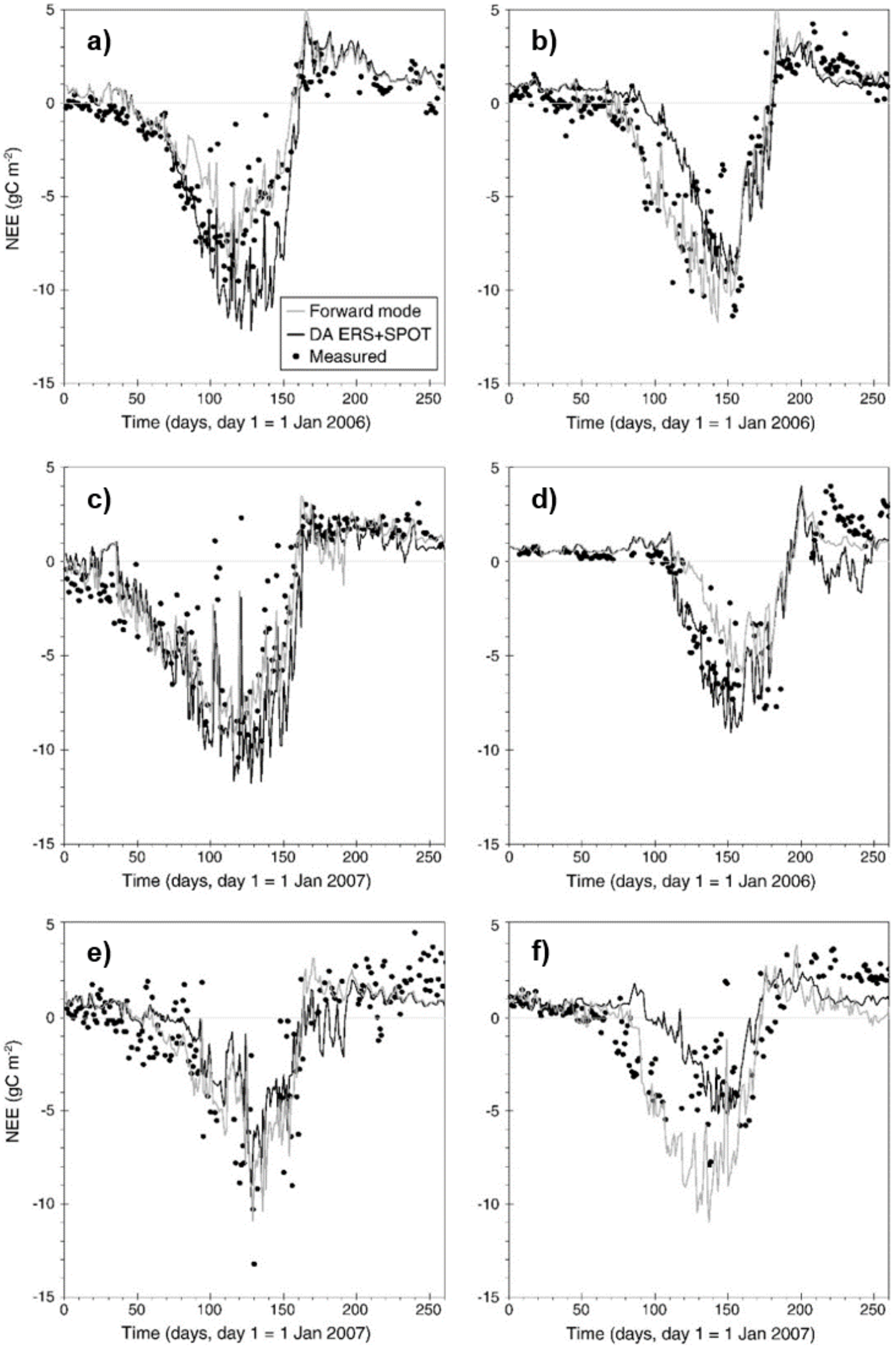

Figure 2.4: Comparison of daily NEE between observed and modelled, forward mode (grey line) and EnKF DA of all EO LAI estimates (black line), for a) Auradé, b) Grignon, c) Lamasquère, d) Klingenberg, e) Oensingen and f) Gebesee.

2.3.3. Ecosystem model results: assimilation of EO data

Simulated LAI

The SPAc EnKF DA simulation decreased the simulated peak LAI values for Auradé (a), Grignon (b), Lamasquère (c) and Oensingen (e) by an average of 0.18 $m^2 m^{-2}$. However, for sites Klingenberg (d) and Gebesee (f), where the EO estimated peak LAI was higher than the simulated value, the DA significantly increased this maximum value by a mean of 1.84 $m^2 m^{-2}$. The timing of the peak LAI was also adjusted by the DA when compared to the forward mode. This adjustment was most notable for Lamasquère, with the maximum LAI being 12 days later with DA; whereas Klingenberg and Gebesee were 9 and 7 days earlier, respectively.

With adjustments in both the magnitude and timing of the simulated LAI, a linear fit (R^2) between the observed and simulated LAI (Table 2.2) showed that the EnKF DA improved the overall modelled and ground measured LAI relationship by an average of 43% when compared to the forward mode. This improvement was noted for all sites with the exception of Auradé where the DA reduced the strength of the relationship by 19%.

Table 2.2: A summary of modelled results (forward mode and EnKF DA of all EO LAI estimates) and measured values. A comparison between the modelled and observed NEE including RMSE, linear fit statistics (R^2 and slope) and cumulative NEE (from sowing to harvest, gC m^{-2}). Comparison between the linear fit and maximum LAI values to measured LAI (m^2 m^{-2}).

	Daily NEE comparisons				**Cumulative NEE**			**LAI comparisons**		**LAI max**	
Sites	**R^2 (forward mode)**	**R^2 (EnKF DA)**	**Slope (forward mode)**	**Slope (EnKF DA)**	**Measured**	**Forward (25/75th percentile)**	**EnKF DA (25/75th percentile)**	**R^2 (forward mode)**	**R^2 (EnKF DA)**	**Forward**	**EnKF DA**
Auradé	0.85	0.91	1.17	0.87	-476	-639 (-790/-462)	-377 (-452/-291)	0.61	0.49	4.60	4.57
Grignon	0.85	0.86	0.70	1.06	-471	-694 (-819/-580)	-593 (-674/-509)	0.75	0.87	4.52	4.47
Lamasquère	0.78	0.82	0.98	0.92	-549	-747 (-916/-584)	-602 (-681/-531)	0.69	0.84	4.96	4.53
Klingenberg	0.65	0.72	0.45	0.47	-287	-361 (-434/-315)	-340 (-449/-221)	0.33	0.92	3.18	5.15
Oensingen	0.60	0.58	0.44	0.64	-369	-426 (-476/-378)	-250 (-304/-188)	0.26	0.67	4.64	4.43
Gebesee	0.78	0.74	0.39	0.53	-242	-170 (-235/-102)	-279 (-364/-213)	N/A	N/A	4.49	6.21

Simulated C fluxes

The assimilation of all EO LAI estimates resulted in some clear adjustments in the magnitudes of daily fluxes (Figure 2.4). Specifically, based on an analysis of the NEE residuals (i.e. observed minus modelled) the sink strength is reduced at Grignon, Oensingen and Gebesee by an average of 1.85 g C m^{-2} per day. Furthermore, the residuals show a progressive increase in the difference between the forward mode and EnKF DA estimates (i.e. forward mode minus DA values) from the beginning of the year to an average of 1.12 g C m^{-2} at the date of maximum C uptake, whereas this average difference was only 0.02 g C m^{-2} 60 days earlier.

With regards to the R^2 between the observed and modelled NEE values (Table 2.2), the DA strengthened this relationship by an average of 6% for sites Auradé, Grignon, Lamasquère and Klingenberg. However, the observed-modelled relationship was weakened by an average of 4% for Oensingen and Gebesee. The slope of this linear fit was also adjusted by DA, and for the majority of these sites, with a value less than 1, this value was increased by 9%, from 0.69 to 0.75 with DA.

Estimated yields

The simulated yield statistic (i.e. total mass of C allocated to the storage organ at harvest) was underestimated at all sites when compared to observed values (Table 2.3). When comparing the average difference across the sites, the magnitude of this underestimation with the EnKF DA (47%) was greater than that in the forward mode (38%). Specifically, in the EnKF DA simulation there was an improvement of 10% between the measured and modelled yield for Klingenberg, however for Auradé the yield was further underestimated by 35% when compared to the forward mode.

Table 2.3: At-harvest yield values (g C m^{-2}) from comparing measured and SPAc estimates in the forward mode (i.e. no DA), DA of ERS LAI (DA ERS), DA of SPOT LAI estimates (DA SPOT) and the DA of both ERS and SPOT LAI estimates.

Sites	**At-harvest yield (gC m^{-2})**				
	Measured	**Forward**	**DA ERS**	**DA SPOT**	**DA ERS and SPOT**
Auradé	283	237	119	149	138
Grignon	350	223	169	179	179
Lamasquère	394	247	239	217	215
Klingenberg	318	223	219	154	254
Oensingen	255	175	174	N/A	N/A
Gebesee	387	82	69	76	65

2.3.4. Synergistic and individual DA comparison of ERS and SPOT results

Assimilating the ERS and SPOT LAI estimates synergistically reduced the RMSE of the forward mode daily NEE simulations by an average of 10% for three out of the six sites (Table 2.4). However, the assimilation of ERS LAI estimates alone improved the simulation for five out of six sites, by an average of 13%. Gebesee was an exception to this as the assimilation of EO LAI in all cases appears to increase the RMSE when compared to the forward mode.

Table 2.4: RMSE values from comparing the observed and modelled daily NEE of SPAc in the forward mode (no DA), DA of ERS LAI estimates (DA ERS), DA of SPOT LAI (DA SPOT) and the DA of both ERS and SPOT LAI estimates.

Sites	**Daily NEE RMSE (gC m^{-2} per day)**			
	Forward	**DA ERS**	**DA SPOT**	**DA ERS and SPOT**
Auradé	2.08	1.53	1.64	1.56
Grignon	1.67	1.53	1.58	1.66
Lamasquère	2.02	1.91	1.82	1.98
Klingenberg	2.19	1.97	2.03	2.22
Oensingen	1.92	1.65	N/A	N/A
Gebesee	1.95	2.26	2.98	2.69
Average	**1.97**	**1.81**	**2.01**	**2.02**

With the EnKF DA, the increase in agreement between the model and observations is also reflected by the at-harvest cumulative NEE (Table 2.5). The observed mean cumulative NEE was -399 g C m^{-2}. The model forward mode estimates of the cumulative NEE were lower than observed for nearly all sites with a mean cumulative NEE of -506 g C m^{-2}, thereby over-estimating the sink strength by 107 g C m^{-2} (27%). The assimilation of all EO-derived LAI had a mean cumulative NEE of -438 g C m^{-2}, thus the mean difference between the measured and modelled cumulative NEE was only 33 g C m^{-2} (8%).

Furthermore, although the RMSE of the simulation of daily NEE at Gebesee was not reduced with DA, the synergistic assimilation of both ERS and SPOT LAI improves the estimated cumulative NEE by over 50% when compared to the forward mode at this site. However, with the individual assimilation of ERS LAI alone the mean cumulative NEE was only -421 g C m^{-2}, representing a difference of only 22 g C m^{-2} (6%) when compared to that of the measured.

Table 2.5: At-harvest cumulative NEE values (g C m^{-2}) from comparing measured and SPAc estimates in the forward mode (no DA), DA of ERS LAI estimates (DA ERS), DA of SPOT LAI (DA SPOT) and the DA of both ERS and SPOT LAI estimates.

Sites	**At-harvest cumulative NEE (gC m^{-2})**				
	Measured	**Forward**	**DA ERS**	**DA SPOT**	**DA ERS and SPOT**
Auradé	-476	-639	-338	-396	-377
Grignon	-471	-694	-543	-565	-593
Lamasquère	-549	-747	-650	-561	-602
Klingenberg	-287	-361	-329	-158	-340
Oensingen	-369	-426	-250	N/A	N/A
Gebesee	-242	-170	-418	-718	-279

2.4. Discussion

This section first includes an evaluation of the LAI retrieval approaches. Second, the performance of the SPAc model with the DA is analysed. Third, the validity of applying the model framework to multiple cereal crop sites is discussed along with recommendations for future research.

2.4.1. LAI retrieval and assimilation

With the image processing techniques applied in this research, a reasonable linear relationship was established between all WDVI values and LAI ground measurements within ±10 days of the SPOT acquisitions (Figure 2.2a). This relationship suggests that a single empirical approximation can adequately describe the relationship between WDVI and LAI across multiple European winter wheat sites.

The relationship between all ERS σ° and ground measured LAI (within ±10 days) was approximated by a single exponential function (Figure 2.2b). This strong exponential relationship is consistent with research by Macelloni *et al.* (2001) for narrow leaf crops. Furthermore, the RMSE between the ERS-derived LAI and measured LAI was reduced by 11% when compared to the LAI estimated from the WDVI. This improvement highlights some of the key operational advantages of SAR over optical sensors for multi-temporal analysis. Specifically, SAR sensors are unaffected by localised atmospheric conditions, thus making them less site specific. Additionally, since it was not necessary to apply atmospheric corrections to the ERS data, this prevents the inclusion of the potential uncertainties involved with the atmospheric normalisation step.

The higher sensitivity of σ° to LAI, when compared to that of the WDVI, can be attributed to the frequency and polarisation of the ERS sensor. Specifically, C-band frequency (5.3 GHz) provides significant amounts of σ° even for moderate crop growth, i.e. early in the growth season (Baronti *et al.*, 1993). Paloscia (2002) mentions that VV-polarised σ° from small-leaf crops (including wheat) decreases with increasing biomass. This is partly due to the attenuation of the VV-polarised signal by the predominantly vertical orientation of the wheat crop structure, including the stem and ears (Ferrazzoli *et al.*, 1999).

The use of EO-derived LAI for adjusting the peak simulated LAI value is clearly dependant on the timing of EO acquisitions. This timing sensitivity was particularly the case for Grignon and Klingenberg where the peak EO LAI days approximately coincided with the maximum LAI day simulated by SPAc. For Grignon, the maximum LAI in the forward mode is similar to that of the ERS LAI acquired around the same day; therefore the peak LAI value remains the same between the forward mode and the EnKF DA (Figure 2.3). However, the SPOT LAI value for Klingenberg, derived around the same date as the peak LAI simulated in the forward mode, resulted in an increase in maximum LAI when the EnKF was applied.

At sites where the SPAc forward mode peak LAI values, and the corresponding NEE sink strengths were higher than observed, it would have been expected that the forward mode simulation overestimated the grain yield. However, although the DA technique was successful in reducing the yield predicted at these sites, in some cases this had the consequence of underestimating this value even further when compared to observations.

This issue of yield estimation suggests weaknesses in the structural representation and calibration of yield formation in SPAc. As recommended by Sus *et al.* (2010), further research should be applied to better constrain the C allocation parameterisation, particularly for the allocation to the roots.

2.4.2. The quality of simulated C fluxes

Generally, the modelled daily NEE matched the magnitude of the observed values more closely with the assimilation of EO LAI estimates (Figure 2.4). For three out of the six sites the overall representation of winter wheat C flux dynamics by SPAc was improved with a mean reduction in RMSE of 10%. However, for the majority of sites the assimilation of all EO LAI estimates was more significant at reducing the simulated sink strength, suggesting that SPAc is slightly negatively biased when compared to observations. These findings are similar to those reported in Sus *et al.* (2010) and also have the consequence of a lower at-harvest cumulative NEE (i.e. overestimate of net C uptake) for most sites. However, for the majority of sites, an increase in the slope value of the measured versus modelled linear regression with the assimilation of all EO LAI estimates suggests that the assimilation technique is also successful at reducing model biases.

A greater improvement in the simulation was achieved with the assimilation of ERS LAI estimates alone, as opposed to synergistically (i.e. with SPOT estimates). This improvement is likely due to a stronger correlation between the ERS $\sigma°$ and LAI, when compared to that of the WDVI and LAI. This enhanced simulation when using the ERS LAI only is reflected both in the RMSE of daily fluxes and the at-harvest cumulative NEE when compared to observations.

The extent to which the differences between modelled and observed values are minimised, particularly around the period of peak C uptake, is also dependant on the timings of the assimilated LAI estimates. This is evident for sites Grignon, Lamasquère and Klingenberg where LAI values are assimilated on days that approximately correspond to the day of peak simulated LAI. Therefore this maximum LAI value is adjusted, which then varies the magnitude of daily NEE values accordingly. This was also discussed in Launay and Guerif (2005), where the model performance for crop yield estimates was improved when the timings of assimilated EO acquisitions coincided with growth stages in the vegetative phase when crop condition is expressed through canopy development.

2.4.3. Is the model framework valid for multiple cropland sites?

Although the sites selected in this analysis are not considered wholly representative of the full variations in European winter wheat crop growing conditions, their spatial distribution covers a relatively large area of western-central Europe. With the assimilation of EO data, an overall improvement in daily C flux modelling was achieved for up to five out of six sites. This suggests that the techniques reported here, including parameterisation and LAI retrieval calibrations, are sufficiently accurate and can reliably enhance the forecasting of winter wheat C fluxes at multiple European sites under different climate conditions. A specific example of this is demonstrated by the precision of the simulated NEE at Lamasquère and Klingenberg. These sites represented the largest variation in latitude and average temperature, along with growth seasons in different years. In spite of this, with the DA of ERS LAI alone, the RMSE of the forward mode simulated NEE fluxes was reduced by 5% and 10% for Lamasquère and Klingenberg, respectively; whereas that of the at-harvest cumulative NEE was improved by 49% and 43%.

Further proof of concept regarding the multi-site applicability of this framework, including the derivation of LAI, is demonstrated at Gebesee. Ground measured LAI was not available for this site, therefore LAI values were estimated from EO data only using retrieval algorithms calibrated using measurements from the remaining sites. The synergistic assimilation of ERS and SPOT estimates had the result of improving the at-harvest cumulative NEE value by around 50% when compared to the forward mode.

2.4.4. Recommendations for further EO data and model developments

This study evaluates the assimilation of LAI estimated from ERS and SPOT EO sensor data, an intrinsic area of development would be to assess the model accuracy with measurements from alternative sensors. Moreover, it is expected that the model framework, including the EnKF DA and LAI retrieval techniques, is sufficiently versatile to facilitate measurements from sensors operating at different spatial and temporal resolutions to those used in this study. This multi-sensor framework would also be appropriate for the inclusion of data from future EO missions, including ESA's Sentinel-1 that consists of a dual satellite constellation (i.e. Sentinel-1A and 1B; Torres *et al.*, 2012). Research should also focus on updating additional model state variables to further improve the precision of the model. Specifically, soil moisture measurements could enhance the simulation of water-balance, as demonstrated in de Wit and van Diepen (2007), and improve the simulation of root allocation. Soil moisture estimates can also be retrieved from dedicated EO sensors, such as the Soil Moisture and Ocean Salinity (SMOS) sensor (Kerr *et al.*, 2012) and Soil Moisture Active Passive (SMAP) mission (Entekhabi *et al.*, 2010).

The model framework was successfully calibrated and applied at the point-scale using within-field mean LAI estimates. Future research could involve investigating the spatial implementation of this modelling approach. Furthermore, if the current model framework was applied spatially over large areas, where input data regarding spatially heterogeneous soil and meteorological conditions are typically unavailable, it is anticipated that the integration of EO observations would become more valuable for updating state-variables.

2.5. Conclusion

A technique for simulating cropland C dynamics has been presented and evaluated over six European cropland sites with varying environmental conditions. The framework consisted of deriving LAI estimates from SPOT and ERS satellite measurements using empirical retrieval algorithms – calibrated using ground measured values. Generally, when compared to the WDVI values calculated from SPOT imagery, a stronger exponential relationship existed between all ERS σ° and ground measured LAI when applied across all sites.

The EnKF sequential DA algorithm was used to update the LAI simulated by SPAc. The modelled outputs were compared to ground measured LAI and NEE flux data. For three out of the six study sites, the assimilation of all EO LAI estimates resulted in a mean error reduction in NEE estimates of around 10%. However, when assimilating the ERS estimated LAI only, this error was reduced by around 13% for the majority of the sites. Further improvements to the simulation were achieved with the DA approach based on the increased accuracy of at-harvest cumulative NEE estimates. For most sites, in the forward mode this value was consistently lower than observed by around 27%; therefore the overall sink strength was overestimated. Assimilating all EO LAI estimates resulted in this value being overestimated by 8%; however assimilating only the ERS LAI estimates resulted in the cumulative NEE being overestimated by 6%.

The results highlights weaknesses in the SPAc parameterisation, specifically those related to allocation to roots and storage organs; nonetheless it is concluded that this DA approach, particularly the use of radar sensors alone, provided a superior means of quantifying the overall extents to which croplands are sources or sinks of C at harvest. Specific refinements should be made to the C allocation scheme as a function of development, with the overall aim of improving the prediction of harvested yield. Such changes would also allow for an improved crop C simulation, not only in the contexts of

C cycling and climate change, but also crop yield forecasting and food security. Future studies could also focus on improving the modelling of C fluxes by assimilating additional state variables from different EO satellite sensors. Furthermore, owing to the intrinsically high variability in soil and meteorological conditions over large areas, it is expected that a technique allowing for the spatial implementation of the current framework would rely more heavily on the assimilated EO measurements.

2.6. Summary

This study has evaluated the sequential DA of optical and radar EO data for constraining the SPAc model estimates of daily fluxes and stocks at the point-scale. By assimilating EO-derived LAI the simulation of cumulative daily C fluxes was improved by over 50% when compared to the simulation without DA. Furthermore, it was demonstrated that the same model framework, including parameterisations, can be applied to generate reliable estimates across multiple cereal crop sites of differing climatic conditions. In the next chapter (Chapter 3), the validity of using a simplified crop model – simulating canopy-scale processes at daily time-steps – is assessed based on the output of SPAc and FLUXNET data.

CHAPTER 3

Impacts of reduced model complexity and driver resolution on cropland ecosystem photosynthesis estimates

Declaration

The research detailed in Chapter 3 was adapted from a paper, which was accepted for publication in the journal *Field Crops Research* on the 11th December 2015 (see Revill *et al.*, 2016). Andrew Revill was the first author of the paper with co-authors: Anthony Bloom and Mathew Williams. In this research, A. Revill carried out the model calibrations with advice from A.A. Bloom. A. Revill wrote the manuscript with edits from M. Williams and additional inputs from A.A. Bloom.

3.1. Introduction

The importance of Croplands with regards to their ecosystems services, along with the challenges associated with food security and climate change, were discussed in Chapter 1. Crop ecosystems are also entirely managed, with farming practices being applied on a range of spatial and temporal scales. This variability in human intervention causes significant uncertainty when investigating feedbacks between climate and the crop C balance (Porter and Semenov, 2005; Reichstein *et al.*, 2013).

Eddy-covariance (EC) flux towers, such as those within the Global FLUXNET regional network, can provide continuous measurements of ecosystem-level C fluxes (Baldocchi *et al.*, 2001). Although these observations span multiple locations, crop cultivars, seasons and climate regimes, the tower sites are sparsely distributed and C fluxes remain inherently under-sampled (Zheng *et al.*, 2014). Alternatively, process-based crop models simulate the key processes involved in regulating ecosystem C exchanges, including photosynthesis and respiration (Williams *et al.*, 1996; Wattenbach *et al.*, 2010). While EC data are direct observations of net ecosystem exchanges (NEE) only, models offer a more complete analysis of processes, and can predict future C budgets under variable climate and management regimes (Ciais *et al.*, 2011; Osborne *et al.*, 2013; Challinor *et al.*, 2014).

Discrepancies between modelled and observed fluxes are due to errors in data (including EC measurements and meteorological drivers) and model uncertainties, such as poorly calibrated parameters, errors in initial state estimates and uncertainties in the representation of ecosystem processes (Williams *et al.*, 2009; Kuppel *et al.*, 2012). Errors in EC data can be attributed to complex terrain and heterogeneous spatial distributions of vegetation within the sensor footprint (Hollinger and Richardson, 2005). Croplands have the advantage of generally being located in more level terrain where mechanisation is possible. While fields are relatively homogeneous in advanced agriculture, European field sizes are small enough for the sample flux footprint to overlap with adjacent fields. For crop models, the most sensitive parameters related to C exchange are those determining photosynthesis and development (Streck *et al.*, 2003; Sus *et al.*, 2010).

Agricultural production is strongly influenced by climate (Hansen, 2002), therefore errors in meteorological drivers lead to uncertainties in model C budget estimates (Ciais *et al.*, 2011). And so, past crop C models, such as the Soil-Plant-Atmosphere crop model (SPAc, Sus *et al.*, 2010) and ORCHIDEE (Krinner *et al.*, 2005), have been applied and evaluated at relatively data-rich sites using fine temporal scale (e.g. half-hourly) drivers. However, at regional to global scales, the number of sites with available fine scale meteorology observations is grossly inadequate; therefore, due to the complex demands for inputs, the practical application of these models is limited (Sheffield *et al.*, 2006).

When compared to standard land-surface models, detailed crop models simulating leaf-level process over multiple canopy layers typically require a large number of input parameters (Valade *et al.*, 2013). Since exact parameter values are difficult to specify they are often based on some expert knowledge (Newlands *et al.*, 2012), but uncertainties associated with prior parameter estimates can result in large variations in simulated C fluxes (Knorr and Heimann, 2001; Ziehn *et al.*, 2012). Calibrated parameters can be overly tuned to particular sites (Kuppel *et al.*, 2012), presenting complications when scaling-up models for providing regional estimates (Fox *et al.*, 2009; Spadavecchia *et al.*, 2011; Newlands *et al.*, 2012). Additionally, parameterising complex models that run at fine temporal scales is often prohibited by computational processing time (Valade *et al.*, 2013; Rafique *et al.*, 2015). This computational demand is particularly significant when optimising parameters and updating state variables (e.g. Chapter 2) through an ensemble of model runs over large areas where parameters may be expected to vary with space.

Here we aim to address the limitations associated with the spatial upscaling of crop C models – specifically the issues related to model complexity, meteorological driver requirements and computational demand. We first use Bayesian inference to calibrate a simple model of photosynthesis based on the output from a previously validated and more complex model. Second, we explore the impacts of using gridded meteorological driver data, as opposed to local observations. We compare photosynthesis estimates derived from the Aggregated Canopy Model (ACM, Williams *et al.*, 1997) to the Soil-Plant-Atmosphere crop (SPAc) model. Our main objective is to determine the viability of using a simple model (i.e. ACM), with a single calibration of photosynthesis, when driven by atmospheric re-analysis data. We hypothesise that the increase in uncertainty linked to model and driver simplification is uncorrelated with, and similar in magnitude, to the uncertainty in driving the more complex SPAc model with sparse driver data. In particular, we address the following research questions:

1) How does model complexity influence estimates of photosynthesis?
2) How do single-site and multi-site photosynthesis calibrations compare across European cereal crop sites?
3) How do the complex and simple model photosynthesis estimates compare when driven by atmospheric re-analysis data?

The novelty of this research is the investigation of parameter and driver uncertainty on model estimates of crop C fluxes. Furthermore, the associated reductions in model complexity and temporal resolution allows ACM to run at higher computational speeds; thus increasing the efficiency for future experimentation. Such experiments include the application of ACM in a data assimilation framework (such as that detailed in Chapters 2 and 3) where large model ensembles are required at multiple locations.

3.2. Data and Methods

A brief overview of the FLUXNET study sites, used to calibrate and validate the modelling approaches, is first provided. Second, details of the two photosynthesis modelling approaches (i.e. SPAc and ACM) are given, along with the calibrations applied to ACM. Third, the technique used to temporally downscale atmospheric reanalysis data (from 3-hourly to half-hourly resolutions), in order to generate the driving data for SPAc, is described.

3.2.1. Study sites

This analysis uses a total of eight European winter wheat crop sites and seasons (Figure 3.1). These sites comprise of the six locations detailed in the research carried out in Chapter 2 (see section 2.2.1) with the addition of two sites that are located in Belgium (Lonzee) and France (Avignon). Since this research involves assessing the performance of a simplified model, the rational for selecting these additional sites was to provide a more thorough evaluation of the multi-site ACM calibration. Specifically, Auradé, Klingenberg, Lonzee and Oensingen were selected as calibration sites as they broadly covered the spatial extents of all eight sites. The remaining four sites – Grignon, Lamasquère, Gebesee and Avignon – were used for validating the multi-site ACM calibration.

With a range in latitude (43.5-51.1°N) and longitude (1.1-13.5°E), the locations of all eight sites span a large area of western-central Europe. Consequently, the sites also show variability in the overall length of the growing season (from sowing to harvest), ranging from 245 days (Auradé) to 342 days (Klingenberg), and seasonal average daily temperatures: from 7°C (Klingenberg) to 14°C (Avignon).

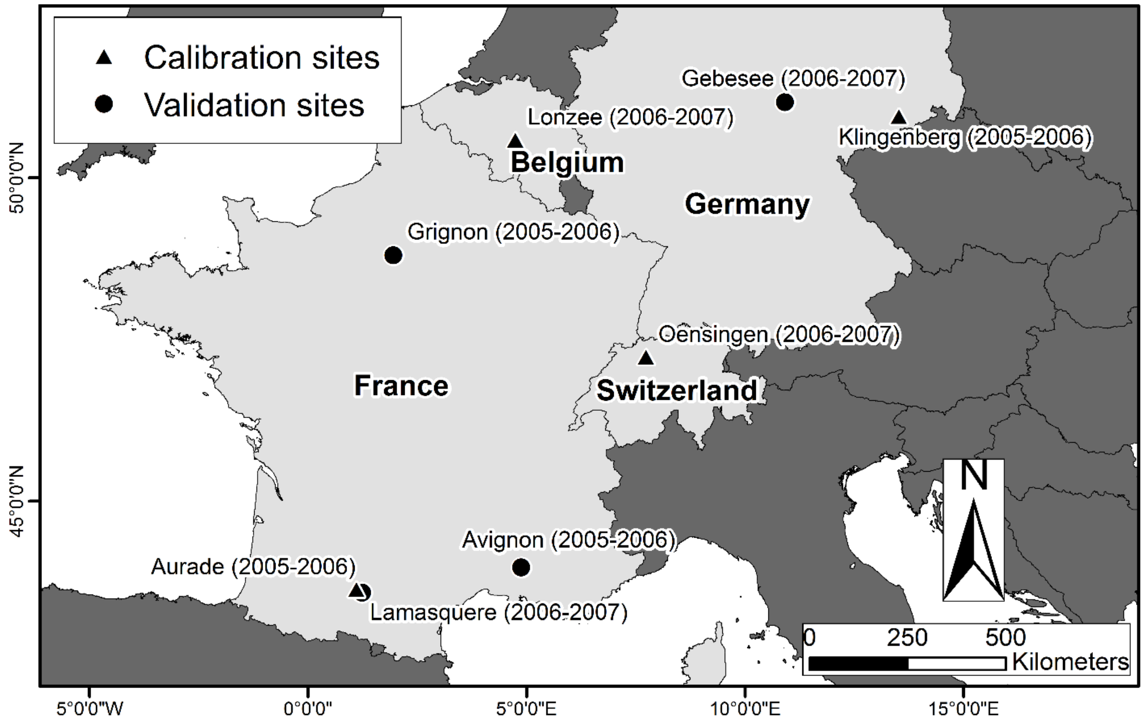

Figure 3.1: Locations of the eight winter wheat crop sites used in this analysis, indicating sites used for calibrating (solid triangle) and validating (solid circle) the daily photosynthesis model (ACM). Growing seasons/years are shown in brackets.

Site data that was available from the Global FLUXNET database (Level-4 processing) consisted of in-situ daily and half-hourly meteorological observations, which were used to drive ACM and the more complex SPAc model, respectively. Daily gross primary productivity (GPP), estimated from aggregated half-hourly EC data (Baldocchi *et al.*, 2001), were used for validating photosynthesis estimates from both models. Additional FLUXNET data used in this analysis consisted of soil texture (i.e. clay/sand ratio) and management information (sowing and harvest dates).

To evaluate the use of spatially averaged atmospheric re-analysis data for driving the two photosynthesis models, we use the Princeton dataset. Princeton is a 3-hourly 1.0° resolution (≈ 111 km) dataset developed by the Land Surface Hydrology Research Group at Princeton University with applied bias corrections (see Sheffield *et al.*, 2006). The Princeton data also has a near-global coverage and thus could supply the driving data for any regional application of a crop C cycle model.

3.2.2. Photosynthesis models

Soil-Plant-Atmosphere crop (SPAc) model

The SPAc model (see Sus *et al.*, 2010 for a full description) simulates cropland ecosystem photosynthesis and water-balance at point-scales over fine temporal (half-hourly) and vertical scales (ten canopy and twenty soil layers). Leaf-level processes are scaled up to make canopy-scale predictions. Furthermore, the leaf and canopy-scale simulations are linked to a radiative transfer scheme: tracking absorption, reflectance and transmittance of direct and diffuse irradiance. Photosynthesis, simulated using the Farquhar model (see Farquhar and von Caemmerer, 1982), and transpiration, determined using the Penman-Monteith equation (Jones, 1992), are linked at leaf-level by a model of stomatal conductance. The stomatal conductance varied accordingly to optimise C uptake whilst maintaining leaf water potential above a minimum value – explicitly linking vapour phase losses with hydraulic transport. The specific SPAc parameters used for simulating winter wheat crop growth, from Sus *et al.* (2010), are listed in Appendix section A1.

Aggregated Canopy Model (ACM)

ACM generates photosynthesis from daily inputs of irradiance, atmospheric CO_2, daylength, leaf area index (LAI), soil water availability, minimum and maximum temperature. To generate GPP from these drivers, ACM uses fixed variables and a series of aggregation equations (listed in Appendix sections B1 and B2) that are designed to reproduce the daily GPP estimates made by SPAc. The equations use a set of 10 unitless coefficients (listed in Table 3.1) that are fitted to create a response surface. This response surface scales the daily accumulation of half-hourly SPAc photosynthesis estimates in order to predict whole-canopy photosynthesis using only coarse-scale (daily) driving data. In essence, ACM is designed to capture and emulate the detailed behaviour of the SPAc photosynthesis routines whilst operating at a reduced temporal scale and, consequently, higher computational speeds.

The SPAc photosynthesis simulation is restricted when soil moisture is unavailable, either from drought or from freezing conditions. ACM does not simulate the energy balance and temperature of soils, therefore we implement a simple switch so that photosynthesis occurs only when daily average temperature is greater than 0.0°C (i.e. GPP = 0.0 g m^{-2} d^{-1} otherwise). This temperature-linked switch acts as an ecological constraint on C accumulation during cold days that typically coincide with key winter cereal crop developmental stages, including tillering and stem extension.

Table 3.1: List of ACM scalar coefficients, including priori minimum and maximum bounds, single-site mean and multi-site calibrated values. Brackets shown next to the single-site mean calibrations show the range in values across the eight sites. The multi-site calibrated coefficients were derived from four of the sites (i.e. calibration sites). The coefficients are used in a series of equations used to generate daily photosynthesis estimates (see Appendix section B2).

Description of coefficient	**Symbol**	**Prior min/max coefficient range**	**Mean single-site calibrated coefficient (min/max range)**	**Multi-site calibrated coefficient**
Nitrogen use efficiency	α_1	$1*10^{-8}$ / 200	14.97 (2.42 / 32.58)	10.38
Daylength coefficient	α_2	$1*10^{-8}$ / 5	0.05 (1.78×10^{-8} / 0.37)	0.04
Canopy CO_2 compensation point	α_3	$1*10^{-8}$ / 30	4.46 (3.73×10^{-8} / 21.36)	2.70×10^{-4}
Canopy CO_2 half compensation point	α_4	$1*10^{-8}$ / 500	187.97 (27.70 / 472.87)	83.18
Daylength constant	α_5	$1*10^{-8}$ / 4	0.04 (0.01 / 0.07)	0.03
Hydraulic coefficient	α_6	$1*10^{-8}$ / 10	2.27 (5.49×10^{-8} / 9.87)	4.54
Maximum canopy quantum yield	α_7	$1*10^{-8}$ / 200	4.69 (2.12 / 12.38)	3.86
Temperature coefficient	α_8	$1*10^{-8}$ / 5	0.01 (1.36×10^{-8} / 0.02)	4.10×10^{-3}
LAI-Canopy quantum yield coefficient	α_9	$1*10^{-8}$ / 50	0.35 (2.62×10^{-4} / 0.72)	0.38
Water potential constant	α_{10}	$1*10^{-8}$ / 50	0.27 (1.16×10^{-8} / 2.02)	2.72×10^{-8}

3.2.3. Data Assimilation Linked Ecosystem Carbon Crop (DALECc) model

The DALECc model provides the half-hourly and daily LAI inputs to both the SPAc and ACM photosynthesis models, respectively, and simulates C mass-balance and allocation when driven by the GPP estimates (Figure 3.2). The model structure consists of C pools/stores that are linked by allocation fluxes (i.e. rate of C allocated to plant tissues) or litterfall fluxes (i.e. rate of C removed from tissues, Figure 3.3). The model includes a crop-specific C allocation scheme that consists of a look-up table defining the C allocation to the plant organs (foliage, stem, storage and root) based on empirical observations (see Penning de Vries *et al.*, 1989). Allocation fractions assigned at each time-step are a function of developmental stage (DS), ranging from -1 (sowing) to 2 (maturity). The DS is calculated based on the accumulation of daily development rates, which are determined from the key developmental responses: daily temperature, photoperiod and vernalisation (until emergence only, Wang and Engel, 1998; Sus *et al.*, 2010).

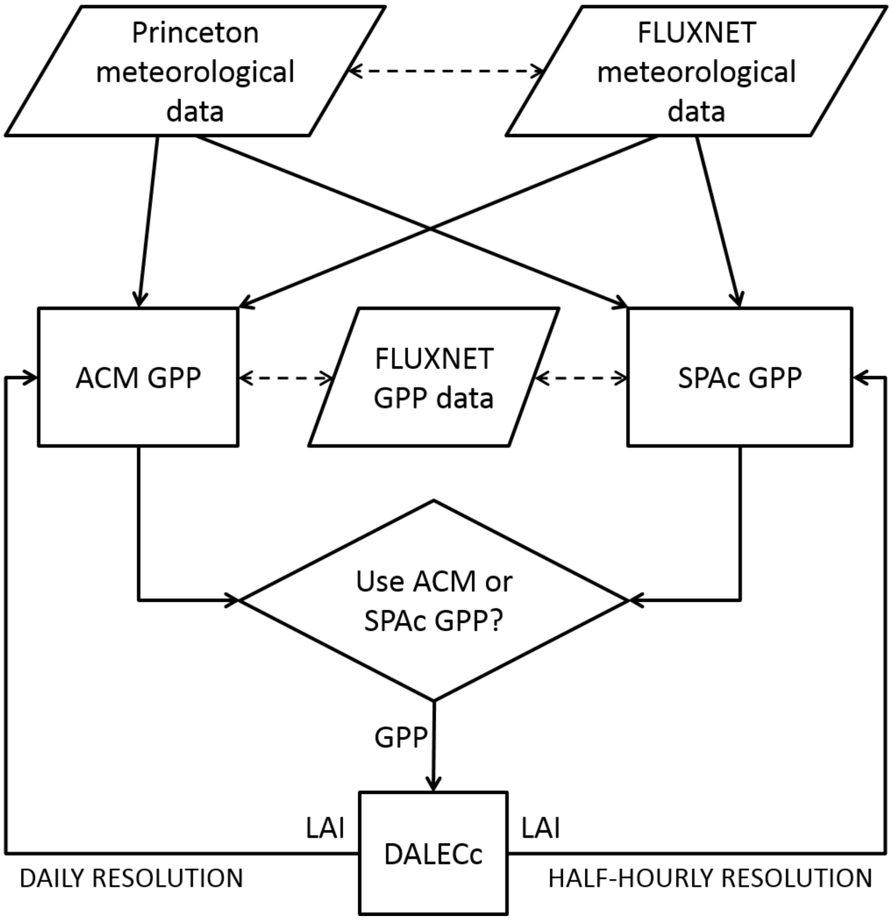

Figure 3.2: Outline of the experimental design of the study. Rectangles show models; rhombuses are datasets; solid lines are inputs; dashed lines are inter-comparisons. The daily photosynthesis model (ACM, left-hand side) can be driven by either climate reanalyses data (Princeton meteorological data) or daily aggregated local observations (FLUXNET meteorological data). The half-hourly photosynthesis model (SPAc, right-hand side) can be driven by either temporally downscaled estimates of the reanalyses data, or directly from the local half-hourly FLUXNET meteorology. A single crop development and carbon cycle model (DALECc) can be driven by either daily (from ACM) or half-hourly (from SPAc) estimates of photosynthesis. DALECc provides daily or half-hourly LAI updates (i.e. for ACM or SPAc, respectively) in order to generate successive photosynthesis estimates. Experimental tests include inter-comparisons between downscaled reanalyses data with FLUXNET meteorology; along with an evaluation of ACM (multi-site calibration) and SPAc GPP with independent FLUXNET GPP estimates.

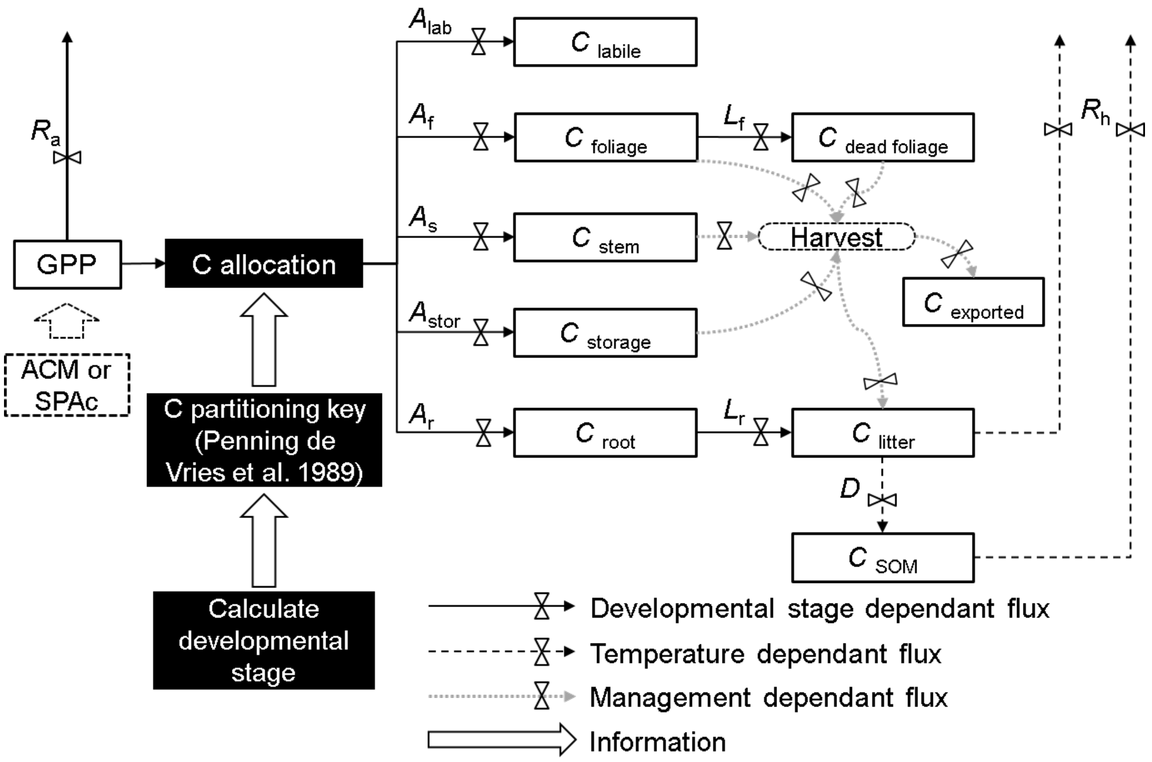

Figure 3.3: Schematic of the Data Assimilation Linked Ecosystem Carbon crop (DALECc) model structure, including a carbon (C) allocation scheme based on crop developmental stage – calculated from daily accumulations of effective temperature, photoperiod and vernalisation (until emergence). The GPP used to drive DALECc is estimated from either the daily photosynthesis model (ACM) or the half-hourly photosynthesis model (SPAc). The calculated C allocation fractions (A) set the C allocation to the five C pools. Allocated C is removed from the system as either harvest export or through heterotrophic respiration from the crop litter and soil organic matter (SOM) C pools.

3.2.4. ACM cropland photosynthesis calibration

In this research we calibrated the 10 ACM coefficients based on the daily simulation of SPAc photosynthesis for winter cereal crops. This calibration was applied on a single-site basis (i.e. at each of the eight sites individually) and then we merged the datasets from the four calibration sites to develop a single multi-site calibration. The calibration steps we carry out can be summarised as: (1) run SPAc once at each site using the local half-hourly FLUXNET drivers to generating daily outputs of GPP; (2) use the FLUXNET daily datasets to produce ACM meteorological drivers: minimum and maximum temperature, irradiance and atmospheric CO_2 (fixed at 393 ppm). For the LAI values – also required to drive ACM – we used the daily accumulation of LAI estimates, as generated by SPAc driving DALECc in the previous step. We assumed that soil moisture was not limiting at any location or time (we chose years when the recorded drought stress was not significant) and so the same soil moisture parameter for ACM was set in all cases; (3) Use SPAc GPP estimates to calibrate the ACM constants.

We use the Metropolis-Hastings Markov Chain Monte Carlo (MHMCMC) approach (e.g. Xu *et al.*, 2006; Hill *et al.*, 2012; Ziehn *et al.*, 2012, amongst others) to calibrate the ACM cereal crop coefficients. The likelihood function for ACM coefficient *x* given SPAc GPP values *c* (p(c|x)) can be expressed as:

$$\mathrm{p(c|x)} = e^{-0.5 \cdot \sum_i \frac{(M(x)-c)^2}{\sigma_{spa}^2}} \qquad \text{Equation 3.1}$$

where *M(x)* is the ACM GPP based on coefficient combination *x*, and σ_{spa} is the Gaussian uncertainty in SPAc GPP: σ_{spa} was set to 2 g C m^{-2} day^{-1}, which approximates the mean relative uncertainty previously quantified for SPAc (see Revill *et al.*, 2013; thesis Chapter

2). In accordance with Bayes' theorem, based on the likelihood p(c|x) the probability density function (PDF) of *x* given SPAc GPP values *c* (p(x|c)) can be expressed as follows:

$$\mathrm{p(x|c)} \propto \mathrm{p(c|x)} \cdot \mathrm{p(x)} \qquad \text{Equation 3.2}$$

where p(x) is the prior probability of *x*. For each ACM coefficient a log-uniform prior value and min/max range is prescribed (see Table 3.1) – these were determined from some preliminary runs whereby the bounds were progressively increased until the accepted coefficient space was unconstrained. To determine p(x|c), we use the MHMCMC to draw 2×10^6 samples of *x*, from which the probability distribution p(x|c) can be adequately approximated: a full description of the MHMCMC algorithm used in this study can be found in Bloom and Williams (2015).

To avoid correlations between subsequent samples only every 10th iteration was used to estimate the posterior coefficient distributions (Ziehn *et al.*, 2012) and so a total of 2×10^5 samples remained. The MHMCMC algorithm was applied five times (i.e. five chains) each with randomly selected initial prior values, in order to verify convergence between the p(x|c) distributions of each ACM constant. We also considered a burn-in time for each chain, defined here as the cut-off time before convergence to the PDF maximum (Ziehn *et al.*, 2012). Specifically, the first 50% of accepted values were discarded as burn-in time estimates. The calibrated values were selected from the union of the remaining values in all five chains based on the most likely value assigned (i.e. the coefficient set *x* with the highest corresponding p(x|c)). We test convergence of the five MHMCMC chains of accepted constant values using the Gelman-Rubin (G-R) diagnostic method (Gelman and Rubin, 1992).

3.2.5. Gridded meteorological driver disaggregation

The use of gridded meteorological products with regional to global coverage are essential to support and evaluate the spatial application of the photosynthesis models. And so, to complement the FLUXNET site-scale meteorological data, we constructed half-hourly and daily drivers (for the SPAc and ACM models, respectively) from the Princeton data. Temporal downscaling (i.e. to half-hourly resolutions) through cubic spline interpolation was first applied to the reanalysis datasets of temperature, precipitation, atmospheric pressure, wind speed, specific humidity and shortwave radiation.

The vapour pressure deficit (VPD), as required by SPAc, was estimated by first calculating the saturation vapour pressure (SVP) based on an empirical relationship to the interpolated temperature (see Monteith and Unsworth, 1990). Second, using the interpolated specific humidity and atmospheric pressure, we estimated the partial pressure (pp) of water vapour (see Roberts, 2010). We then estimated the relative humidity (RH = pp/SVP) and VPD, expressed as follows:

$$\mathrm{VPD} = \left(1 - \left(\frac{\mathrm{RH}}{100}\right)\right) \cdot \mathrm{SVP} \qquad \text{Equation 3.3}$$

In this research we considered the 3-hourly temporal coverage of the Princeton radiation to be too sparse for a reliable interpolation that could be used directly by SPAc. Therefore, we first constructed half-hourly estimates of the extraterrestrial radiation: a function of latitude, day of year and time (see Allen *et al.*, 1998). The relative shortwave radiation (i.e. ratio of actual to clear sky solar radiation) was then calculated as the fraction of the half-hourly interpolated Princeton values to the extraterrestrial radiation and thus used to express atmospheric attenuation (i.e. cloudiness). The half-hourly extraterrestrial radiation values were then multiplied by the daily averages of these half-hourly ratios. Essentially, this daily averaged ratio was used to scale the half-hourly potential radiation accordingly to reflect the degree of cloudiness. Daily drivers for ACM (minimum/maximum temperature and daily radiation) were then determined from the disaggregated half-hourly datasets.

3.2.6. Approaches for evaluating model performance

We analysed outputs from the temporal disaggregation routine applied to the Princeton data when generating both the half-hourly and daily drivers. However, we focus on irradiance and temperature estimates only as these variables are considered as the major environmental factors determining winter wheat development (Streck *et al.*, 2003). The disaggregated data were compared to FLUXNET site-level observations, and metrics were calculated: root-mean-square-error (RMSE) describing the average estimated-measured differences and the normalised mean bias (NMB) quantifying model over or under-predictions. We also compute the traditional R^2 regression statistic (least-squares coefficient of determination).

This study evaluates the calibration of a simple photosynthesis model when compared to estimates made by a more complex model. And so, where Sus *et al.* (2010) compared SPAc to independent EC data at the cereal crop sites, here we primarily focus our analysis between the ACM calibrations (single-site and multi-site) and SPAc outputs. We first compare ACM and SPAc estimates from using the local FLUXNET drivers (i.e. daily and half-hourly for ACM and SPAc, respectively), where disparities between the models were statistically summarised. For the multi-site calibration, we further extended this analysis to compare the ACM and SPAc photosynthesis relationship at the calibration and validation sites. Since reanalysis data has not been previously used to drive SPAc, we then compared the ACM (multi-site calibration only) and SPAc outputs – with both models driven using the disaggregated Princeton data – to GPP derived from the FLUXNET EC data.

3.3. Results

The results from the temporally downscaling procedure applied to generate the irradiance and temperature estimates are present here first. Second, the photosynthesis estimates from the calibrated ACM and SPAc models – both using local meteorological drivers – are compared to each other and the FLUXNET photosynthesis predictions. Third, estimates from the two models are evaluated when driven using the downscaled reanalysis data.

3.3.1. Meteorological disaggregation routine

Irradiance

There was a strong correlation (mean $R^2 = 0.76$) between the half-hourly disaggregated irradiance estimates from the Princeton data and FLUXNET Level-4 site-scale observations, as reported in W m^{-2} (Table 3.1 and Auradé example Figure 3.4). Furthermore, across all sites there was a relatively small range in R^2 ($0.71 \leq R^2 \leq 0.85$). From a linear fit, the sites showed positive intercept and slope values less than 1 suggesting similar biases, along with an NMB range from 13% to 54% (mean NMB = 27%). However, the Lonzee site, which had a slope value greater than 1 and the most bias (NMB = 54%), was a notable exception to this. Across all sites, the RMSE of the half-hourly irradiance estimates ranged from 96 to 134 W m^{-2} (mean RMSE = 111 W m^{-2}).

Table 3.2: Summary statistics evaluating half-hourly predictions of solar irradiance and temperature, produced from temporally disaggregating 3-hourly Princeton reanalysis data, used to drive SPAc. Comparisons are made against half-hourly FLUXNET Level-4 site-scale observations from sowing to harvest across eight crop sites. Metrics include root-mean-square-error (RMSE) and normalised mean bias (NMB).

	Half-hourly irradiance					**Half-hourly temperature**				
Site	**R^2**	**slope**	**Intercept ($W m^{-2}$)**	**RMSE ($W m^{-2}$)**	**NMB (%)**	**R^2**	**slope**	**Intercept (°C)**	**RMSE (°C)**	**NMB (%)**
Auradé	0.79	0.86	45.52	104.88	16.63	0.79	0.90	2.02	3.35	11.27
Grignon	0.76	0.89	45.47	101.59	25.57	0.67	0.78	3.18	4.05	16.89
Klingenberg	0.75	0.83	44.28	102.16	16.24	0.74	0.85	2.77	4.53	25.79
Avignon	0.85	0.91	35.62	95.78	13.31	0.77	0.86	2.70	3.61	7.84
Lonzee	0.75	1.09	49.99	119.23	54.04	0.63	1.07	-1.95	4.82	-10.9
Lamasquère	0.74	0.91	54.72	122.38	30.93	0.55	0.85	2.74	5.19	9.09
Gebesse	0.74	0.86	47.08	109.78	21.33	0.62	1.04	-3.77	5.76	-31.68
Oensingen	0.71	0.93	57.24	134.38	35.68	0.52	0.74	0.20	5.95	-24.41
Average	**0.76**	**0.91**	**47.62**	**111.27**	**26.72**	**0.66**	**0.89**	**0.99**	**4.66**	**0.49**

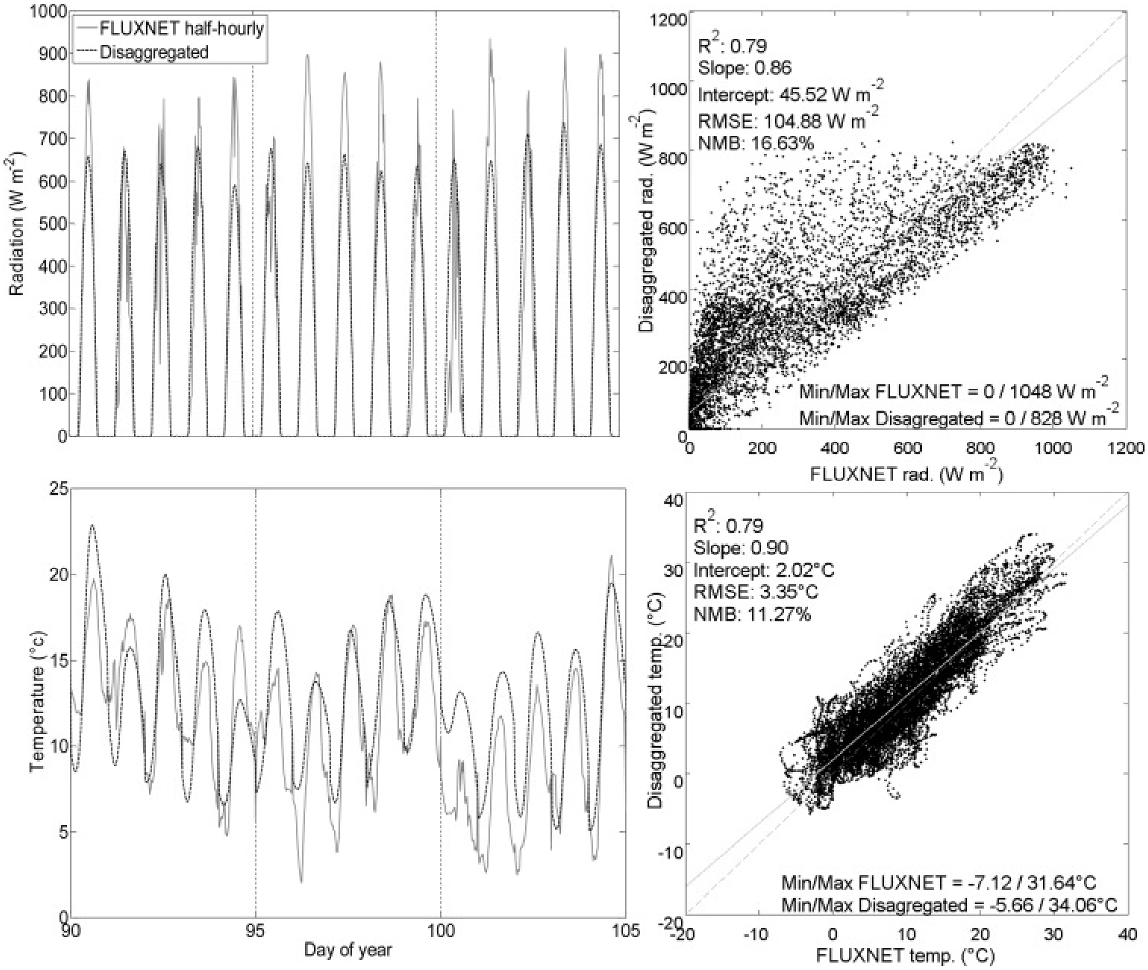

Figure 3.4: Comparisons of the disaggregated 3-hourly 1.0˚ resolution reanalysis data to FLUXNET Level-4 half-hourly observations shown for Auradé. Example time-series plots, for radiation (top-left panel) and temperature (bottom-left panel), for disaggregated (dashed line) and FLUXNET (grey line) values, shown for day of year 80 to 100 (21st March – 10th April). Scatter plots comparing disaggregated and FLUXNET values, for radiation (top-right panel) and temperature (bottom-right panel), over the entire crop growth season at Auradé. Metrics include the root-mean-square-error (RMSE) and normalised mean bias (NMB).

The daily irradiance estimates, as derived from sampling the half-hourly disaggregated values, compared to the daily FLUXNET Level-4 observations, reported in MJ m^{-2} d^{-1}

(Table 3.3 and Auradé example Figure 3.5), show a similar degree of bias (mean NMB = 22%) to that of the half-hourly estimates. There was also a similarly strong correlation ($0.59 \leq R^2 \leq 0.78$). Across all sites, the RMSE of the daily irradiance estimates ranged from 3.62 to 5.03 MJ m^{-2} d^{-1} (mean RMSE = 4.17 MJ m^{-2} d^{-1}).

Table 3.3: Summary statistics evaluating daily average predictions of solar irradiance and temperature, used as driver datasets for ACM, produced from sampling the half-hourly time-series of disaggregated Princeton 3-hourly reanalysis data. Comparisons are made against daily FLUXNET Level-4 site-scale observations from sowing to harvest across eight European crop sites.

	Daily irradiance					**Daily temperature**				
Site	**R^2**	**slope**	**Intercept (MJ m^{-2} d^{-1})**	**RMSE (MJ m^{-2} d^{-1})**	**NMB (%)**	**R^2**	**slope**	**Intercept (°C)**	**RMSE (°C)**	**NMB (%)**
Auradé	0.73	0.72	5.66	3.79	16.88	0.85	0.91	1.95	2.55	11.22
Grignon	0.78	0.83	4.57	3.66	26.48	0.85	0.88	1.97	2.61	12.55
Klingenberg	0.75	0.79	4.28	3.68	16.46	0.88	0.99	1.71	3.12	24.23
Avignon	0.78	0.84	4.06	3.62	13.17	0.88	0.86	2.99	2.24	10.38
Lonzee	0.63	0.82	4.88	4.61	32.58	0.59	0.84	1.79	3.63	0.81
Lamasquère	0.62	0.74	6.73	4.57	31.65	0.59	0.72	4.39	3.54	10.79
Gebesse	0.70	0.78	4.70	4.40	19.10	0.61	0.86	0.05	4.36	-13.72
Oensingen	0.59	0.71	5.64	5.03	19.39	0.55	0.64	2.63	4.33	-10.14
Average	**0.70**	**0.78**	**5.07**	**4.17**	**21.96**	**0.73**	**0.84**	**2.19**	**3.30**	**5.77**

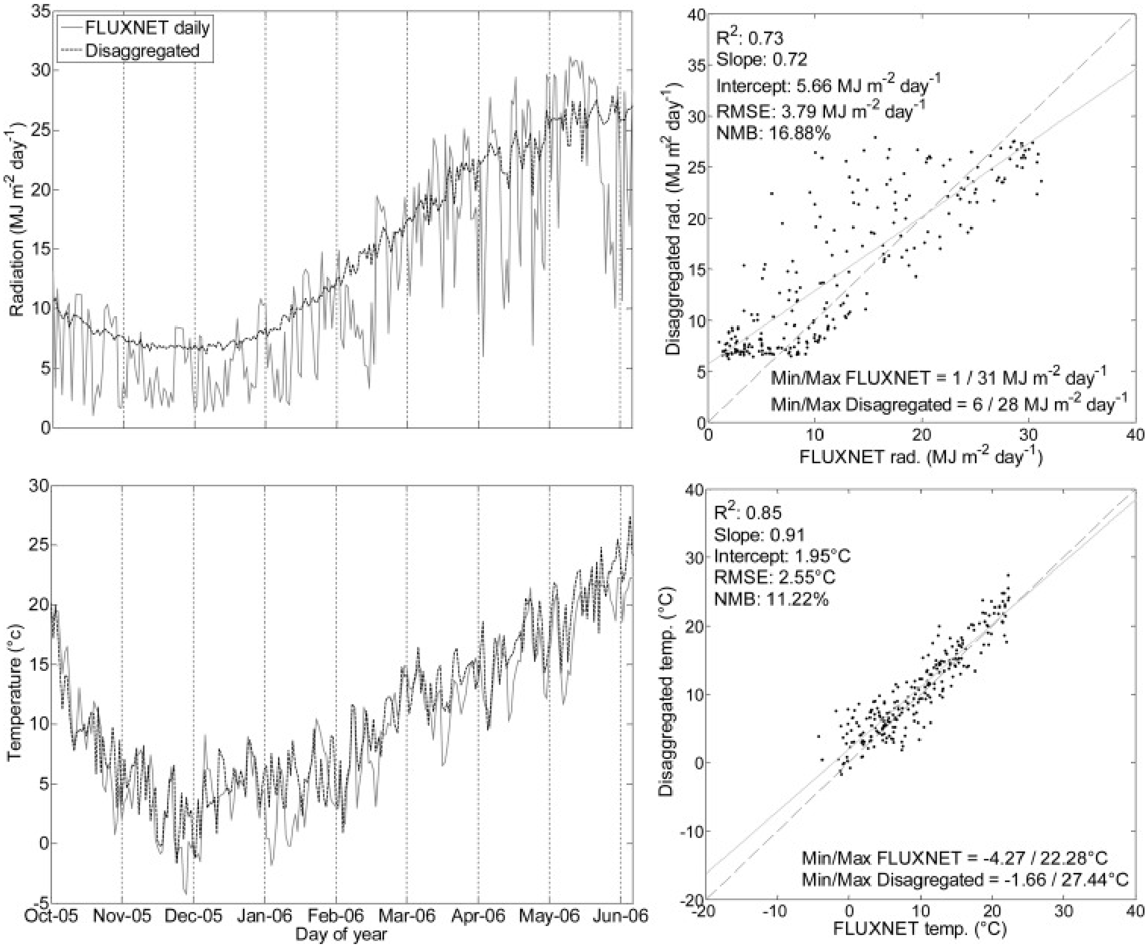

Figure 3.5: Plots of daily radiation and temperature estimates extracted from the disaggregated 3-hourly 1.0˚ resolution reanalysis data compared to FLUXNET Level-4 daily observations shown for Auradé. Time-series plots, for radiation (top-left panel) and temperature (bottom-left panel), for disaggregated (dashed line) and FLUXNET (grey line) values are shown for all day between sowing and harvest. Scatter plots comparing disaggregated and FLUXNET values, for radiation (top-right panel) and temperature (bottom-right panel), also shown for the entire crop growth season at Auradé.

Temperature

The half-hourly time-series of disaggregated temperature estimates explained an average of 66% of the variability recorded across all observations (Table 3.2 and Figure 3.4). The overall correlation range ($0.52 \leq R^2 \leq 0.79$) of the half-hourly temperature estimates to the FLUXNET site-level observations was larger when compared to that of the half-hourly irradiance values. Based on a linear fit, Lonzee and Gebesse both had negative intercepts and slopes greater than 1, whereas the remaining sites had positive intercepts and slopes less than 1 suggesting the degree of biases in the temperature was not consistent across all sites. Although the average bias was low (mean NMB = 0.49%), the range in NMB values (-32% ≤ NMB ≤ 26%) across all sites was large. The RMSE of the half-hourly temperature estimates ranged from 3.35 to 5.95°C (mean RMSE = 4.66°C).

Similarly to the half-hourly values, the analysis of the daily temperature estimates when compared to the FLUXNET observations across all sites (Table 3.3 and Figure 3.5) show a relatively low bias (mean NMB = 6%). However, the range in NMB values (-14% ≤ NMB ≤ 24%) was smaller when compared to the half-hourly analysis. Furthermore, the daily estimates have a generally stronger correlation to the observations ($0.55 \leq R^2 \leq 0.88$) when compared to the half-hourly values, and the RMSE had a smaller magnitude, from 2.24 to 4.36°C (mean RMSE = 3.30°C).

3.3.2. Model comparisons

Convergence analysis

For a qualitative determination of the convergence, we compared the five MHMCMC chains for both the single-site and multi-site calibrations. For the majority of constants the interquartile ranges in accepted values across the five chains are both similar in magnitude and share a degree of overlap. Furthermore, the G-R test values for each coefficient (1.00–1.12) were all close to 1 indicating convergence (Xu *et al.*, 2006).

Single-site calibration

ACM was run using a local calibration of constants (listed in Table 3.1) and local meteorology drivers (i.e. FLUXNET) for all days within each crop growth season (i.e. sowing to harvest). From evaluating the time-series GPP estimates by comparing to SPAc (Table 3.4 and Figure 3.1), for all eight sites there was a significant correlation between ACM and SPAc estimates (mean $R^2 = 0.97$), the range in R^2 values ($0.95 \leq R^2 \leq 0.98$) was also small. The RMSE ranged from 0.87 g m^{-2} d^{-1} (Gebesse) to 1.22 g m^{-2} d^{-1} (Oensingen) with a mean RMSE of 1.09 g m^{-2} d^{-1}. The slope of the linear fit ranged from 0.95 to 1.23; however for the majority of sites this value was greater than 1 indicating some positive biases (mean NMB = 6%).

Table 3.4: Summary statistics comparing ACM and SPAc GPP estimates from sowing to harvest indicating the sites used for calibrating (c) and validating (v) the multi-site ACM calibration. ACM GPP is shown for single-site and multi-site coefficient calibrations using local meteorological drivers. ACM (multi-site calibration) and SPAc GPP comparisons are also shown with both models driven with disaggregated 3-hourly 1.0° resolution reanalysis data.

Site (calibration or validation)	**Site-level calibration (FLUXNET drivers)**					**Multi-site calibration (FLUXNET drivers)**					**Multi-site calibration (disaggregated drivers)**				
	R^2	**slope**	**Intercept (g m^{-2} d^{-1})**	**RMSE (g m^{-2} d^{-1})**	**NMB (%)**	**R^2**	**slope**	**Intercept (g m^{-2} d^{-1})**	**RMSE (g m^{-2} d^{-1})**	**NMB (%)**	**R^2**	**slope**	**Intercept (g m^{-2} d^{-1})**	**RMSE (g m^{-2} d^{-1})**	**NMB (%)**
Auradé (c)	0.97	1.06	-0.36	1.04	-0.37	0.97	0.99	-0.38	0.98	-7.89	0.98	0.90	-0.25	0.82	-13.03
Grignon (v)	0.97	1.07	-0.48	1.20	-1.76	0.96	0.98	-0.37	1.13	-9.37	0.96	0.99	-0.18	1.33	-3.62
Klingenberg (c)	0.96	1.05	-0.31	1.17	-2.74	0.97	1.06	-0.32	1.05	-1.63	0.89	0.79	-0.71	2.16	-32.71
Avignon (v)	0.96	0.95	0.24	0.92	-0.46	0.94	1.08	0.62	1.35	19.20	0.93	1.09	1.34	1.53	33.49
Lonzee (c)	0.97	1.11	0.11	1.12	13.30	0.96	0.96	0.14	1.10	-1.13	0.64	1.04	3.07	3.78	66.59
Lamasquere (v)	0.97	1.11	0.09	1.16	13.17	0.96	0.95	-0.03	1.06	-5.27	0.96	0.86	0.38	1.11	-8.94
Gebesse (v)	0.98	1.23	-0.03	0.87	21.83	0.96	1.22	0.04	1.16	23.61	0.84	1.02	0.59	2.76	14.65
Oensingen (c)	0.95	1.15	-0.33	1.22	7.39	0.93	1.15	-0.18	1.48	10.72	0.89	0.90	-0.31	2.20	-14.66
Average calibration (c)	0.96	1.09	-0.22	1.14	4.40	0.96	1.04	-0.19	1.15	0.02	0.85	0.91	0.45	2.24	1.55
Average validation (v)	0.97	1.09	-0.05	1.04	8.20	0.96	1.06	0.07	1.18	7.04	0.92	0.99	0.53	1.68	8.90
Overall average	**0.97**	**1.09**	**-0.13**	**1.09**	**6.30**	**0.96**	**1.05**	**-0.06**	**1.16**	**3.53**	**0.89**	**0.95**	**0.49**	**1.96**	**5.22**

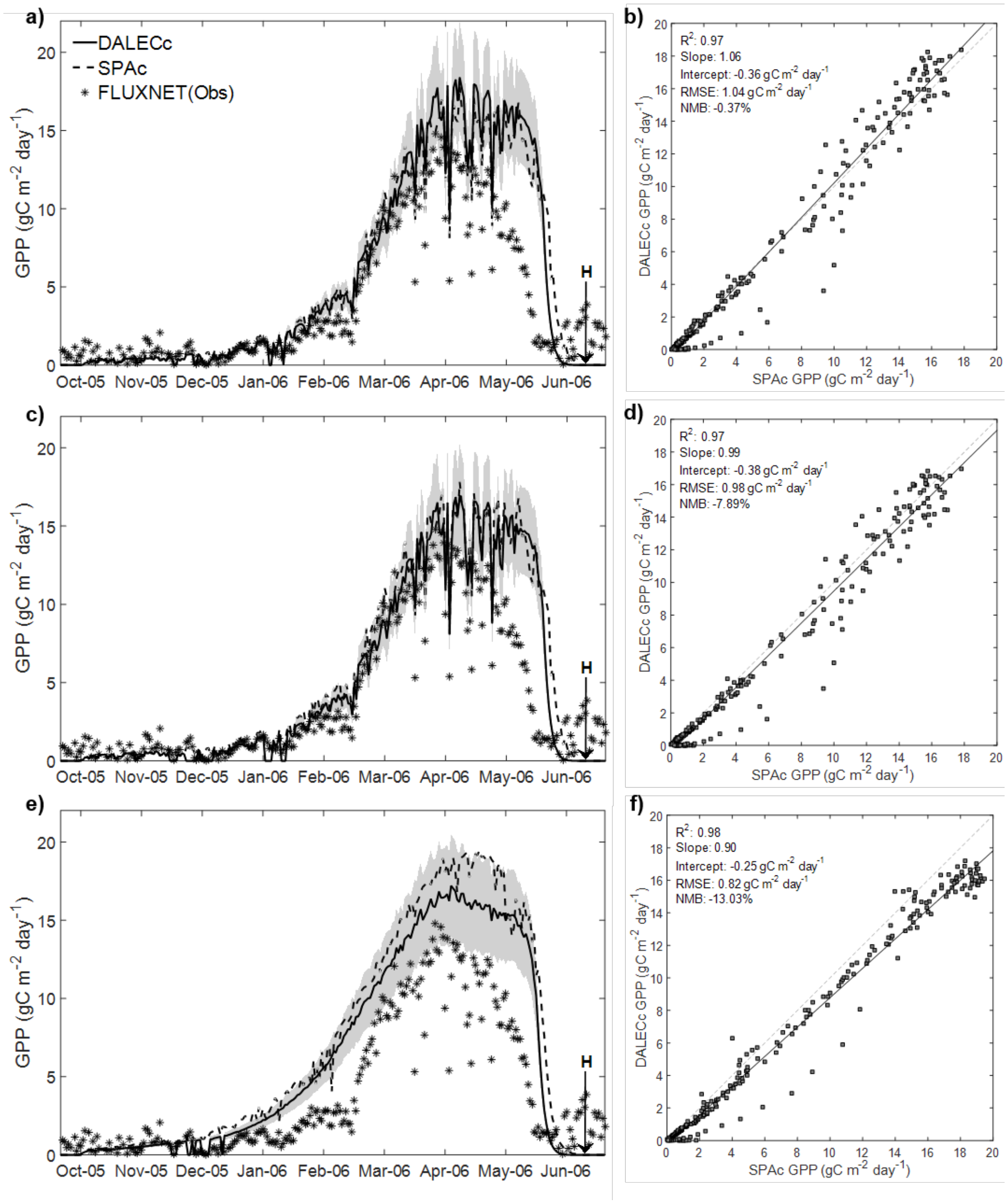

Figure 3.6: Plots (shown for Auradé only) comparing ACM and SPAc GPP estimates including ACM calibrations: single-site (a, b) and multi-site (c, d) using local meteorological drivers. ACM (multi-site calibration) and SPAc estimates – both models using disaggregated drivers – are also shown (e, f). Time-series consist of ACM (black line; grey shading indicating 5/95% confidence interval), SPAc (dashed black line) and FLUXNET estimates (black asterisks), including a black arrow indicating harvest (H) date. Scatter plots compare ACM and SPAc estimates, including 1:1 line (grey line).

Multi-site calibration

Similarly to the single-site calibration, from comparing the ACM GPP generated using the multi-site calibrated constants (listed in Table 3.1) to SPAc estimates, with both models using the FLUXNET drivers (Table 3.4 and Figure 3.6), a high correlation (mean $R^2 = 0.96$) was achieved between the two models at all sites. The range in R^2 values ($0.93 \leq R^2 \leq 0.97$) was relatively small. The RMSE results between ACM and SPAc were also comparable, ranging from 0.98 g m^{-2} d^{-1} (Auradé) to 1.48 g m^{-2} d^{-1} (Oensingen) with a mean value of 1.16 g m^{-2} d^{-1}. When compared to the single-site ACM constants, the use of the multi-site calibration showed a slight reduction in the biases of estimates, demonstrated by a decrease in the mean slope (from 1.09 to 1.05) and an increase in the intercept (from -0.13 to -0.06 g m^{-2} d^{-1}). Moreover, although differences in the degree of biases exist at individual sites, the difference in the average NMB for the single-site (6%) and multi-site (4%) were very similar.

When evaluating the performance of the multi-site ACM calibration specifically at the validation sites the mean correlation to SPAc (mean $R^2 = 0.96$) was the same as that for the calibration sites. The mean RMSE values were also similar in magnitude, being 1.15 g m^{-2} d^{-1} and 1.18 g m^{-2} d^{-1} for the calibration and validation sites, respectively. However, the mean NMB indicated a positive increase in bias between the calibration (mean NMB = 0%) and validation sites (mean NMB = 7%).

Local versus disaggregated meteorological drivers

We compared differences between the multi-site calibrated ACM and SPAc model GPP estimates when both models are driven by the disaggregated meteorological data (Table 3.4 and Figure 3.6). For the majority of sites, there was a strong correlation between GPP predictions from the two models ($0.64 \leq R^2 \leq 0.98$). However, with an R^2 value of 0.64, this correlation for Lonzee was significantly weaker when compared to other sites. Furthermore, with an intercept value of 3.07 g m^{-2} d^{-1}, a linear regression indicated biases in the Lonzee predictions. Compared to the relationship between the two models when using local drivers, the range in RMSE values across the sites was relatively large: from 0.82 g m^{-2} d^{-1} (Auradé) to 3.78 g m^{-2} d^{-1} (Lonzee). This corresponds to a large inter-site range in NMB values ($-33\% \leq \text{NMB} \leq 67\%$).

3.3.3. Model comparison with FLUXNET photosynthesis

Using the disaggregated gridded drivers, we compared ACM (using the multi-site calibration) and SPAc predictions to GPP estimates derived from FLUXNET EC data (Table 3.5 and Figure 3.7). For both models, overall there was a consistent and similarly strong correlation to the FLUXNET data across all sites: ACM ($0.61 \leq R^2 \leq 0.88$) and SPAc ($0.52 \leq R^2 \leq 0.88$). The overall degree of biases in estimates from ACM (mean NMB = 32%) and SPAc (mean NMB = 35%) were also comparable. However, the range in SPAc biases ($-45\% \leq \text{NMB} \leq 88\%$) was larger when compared to the ACM estimates ($3\% \leq \text{NMB} \leq 59\%$).

Table 3.5: Summary statistics of ACM (multi-site coefficient calibration) and SPAc GPP estimates compared to FLUXNET GPP, when both models are driven with the disaggregated meteorological data. Indicating the ACM multi-site calibration (c) and validation (v) sites.

Site (calibration or validation)	**ACM (multi-site calibration)**					**SPAc**				
	R^2	**slope**	**Intercept (g m^{-2} d^{-1})**	**RMSE (g m^{-2} d^{-1})**	**NMB (%)**	**R^2**	**slope**	**Intercept (g m^{-2} d^{-1})**	**RMSE (g m^{-2} d^{-1})**	**NMB (%)**
Auradé (c)	0.86	1.30	1.15	2.38	58.78	0.84	1.42	1.64	2.73	82.57
Grignon (v)	0.61	0.98	2.26	3.94	54.74	0.85	1.28	1.67	2.69	69.86
Klingenberg (c)	0.73	1.13	0.47	3.38	26.72	0.52	1.14	2.45	5.42	88.33
Avignon (v)	0.88	0.88	2.74	1.91	41.42	0.88	0.80	1.36	2.14	5.94
Lonzee (c)	0.78	0.89	1.19	2.96	9.75	0.86	0.68	-0.80	2.56	-45.25
Lamasquere (v)	0.79	1.08	0.61	2.72	19.80	0.80	1.25	0.34	3.04	31.56
Gebesse (v)	0.84	1.52	-0.32	2.73	42.96	0.69	1.24	0.02	3.38	24.69
Oensingen (c)	0.78	1.02	0.01	3.13	2.57	0.74	1.04	0.93	3.64	20.19
Average	**0.78**	**1.10**	**1.01**	**2.89**	**32.09**	**0.77**	**1.11**	**0.95**	**3.20**	**34.74**

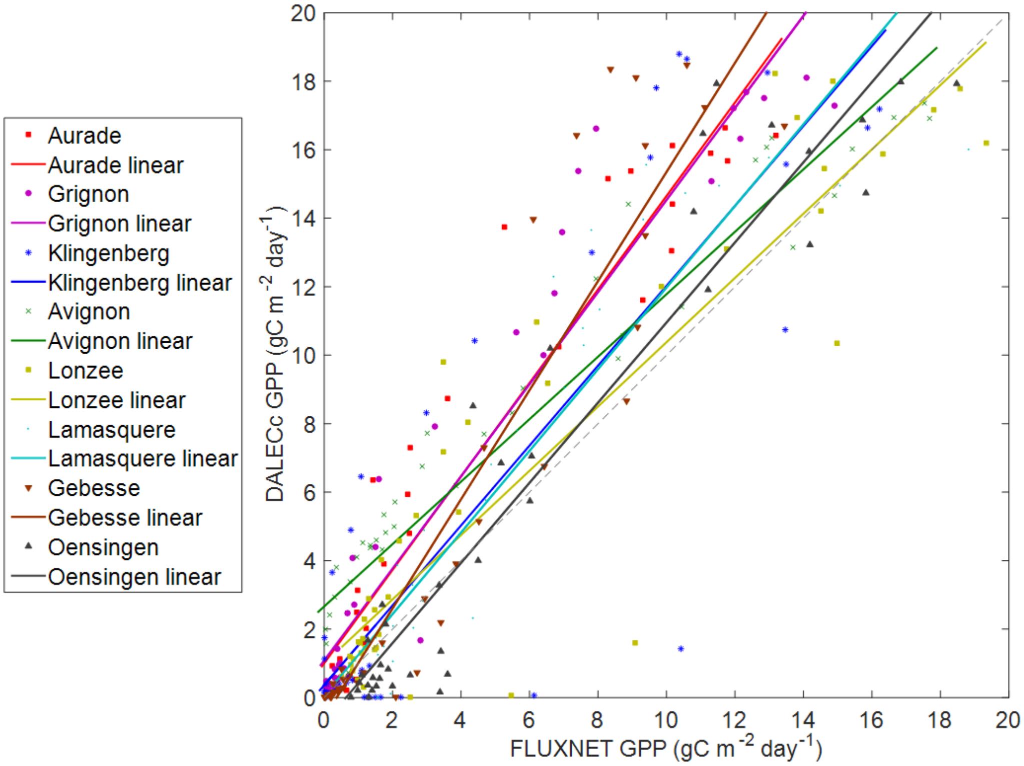

Figure 3.7: Plot comparing ACM GPP (multi-site calibration and disaggregated meteorological drivers) for all eight crop sites to FLUXNET estimates. The plot includes the 1:1 line (grey dashed line). Note: for simplicity, only weekly aggregates of GPP are shown here.

The range in RMSE between ACM and FLUXNET GPP (from 1.91 to 3.94 g m^{-2} d^{-1}) is smaller when compared to that between ACM and SPAc (from 0.82 to 3.78 g m^{-2} d^{-1}). From the linear fit there was an average slope of 1.10 indicating an overall positive bias in ACM GPP predictions compared to FLUXNET. For the ACM estimates at Lonzee, although having a relatively weak correlation and large biases when compared to SPAc ($R^2 = 0.64$, NMB = 67%), the correlation was stronger when comparing to FLUXNET estimates at this site ($R^2 = 0.78$, NMB = 10%).

Similarly to the comparison between ACM and SPAc, when comparing ACM photosynthesis to the FLUXNET data there was a consistently high correlation at the calibration (mean $R^2 = 0.79$) and validation sites (mean $R^2 = 0.78$). The error was also similar between these two groups of sites with a mean RMSE of 2.96 g m^{-2} d^{-1} and 2.83 g m^{-2} d^{-1} for the calibration and validation sites, respectively. However, the estimates at the validation sites were more positively biased (mean NMB = 40%) when compared to those at the calibration sites (mean NMB = 24%).

3.4. Discussion

The use of ACM for reproducing the photosynthesis estimates of the SPAc model is first discussed here. Second, the performance of both the models when driven by the downscaled meteorological data is evaluated. Third, the limitations and implications of the ACM calibrations are discussed.

3.4.1. Reduced model complexity

The application of ACM when driven with site-level meteorological data had a consistently high correlation to SPAc GPP estimates for both single-site and multi-site calibrations (Table 3.4). Therefore, a reduction in model complexity, including temporal resolution (i.e. from half-hourly to daily time-steps), does not significantly diminish the overall accuracy of photosynthesis estimates at daily timescales.

3.4.2. Single-site versus multi-site calibration

The analysis between the ACM coefficient MHMCMC chains, derived from SPAc GPP estimates, indicated convergence when comparing across eight sites for both the single-site and multi-site calibrations. Therefore, the overall ACM coefficient calibration approach detailed here, including sample size, was sufficient when searching the available space (i.e. prior upper and lower bounds) defined for each of the 10 ACM constants.

When comparing all the single-site and multi-site ACM calibrations with SPAc (Table 3.4) the accuracy and biases in ACM GPP were consistent in magnitude. Similar results in Kuppel *et al.* (2012), albeit for a deciduous broadleaf forest application, demonstrated that NEE estimates generated using a multi-site coefficient optimisation were also as good as those achieved using a single-site optimisation.

Although an increase in bias was observed at the validation sites, the correlation of the multi-site calibrated ACM to SPAc was equally high when compared to that of the calibration sites. Furthermore, with an increase in mean model error of only 0.02 g m^{-2} d^{-1}, the overall effectiveness of the model was not significantly reduced when applied at the validation sites. Consequently, from using only four calibration sites, we have produced a generic and robust ACM calibration of winter wheat photosynthesis; generating estimates that are comparable to outputs from a site-specific calibration and a more complex model. However, we acknowledge that the crop seasons and sites selected in this analysis were not considered to be drought-stressed and soil moisture was assumed to be fixed across all sites.

3.4.3. Performance of spatially aggregated drivers

From the temporal disaggregation procedure that was applied to the Princeton reanalysis data (i.e. from 3-hourly to half-hourly estimates), the temperature and irradiance estimates generally had a high agreement with the independent FLUXNET observations. However, there were biases in the two datasets across all sites. This bias was particularly the case for the half-hourly temperature estimates that indicated a large range of positive and negative biases (-32% ≤ NMB ≤ +26%) in the Princeton data.

We evaluated the use of the temporally disaggregated reanalysis data for driving SPAc. ACM (multi-site calibration) was then driven based on the daily aggregates (e.g. minimum and maximum temperature) of the half-hourly time-series of estimates. The GPP estimates from both models demonstrated a high agreement (Table 3.4). This observation indicates that the uncertainty associated with a reduction in model complexity is uncorrelated with that of a more complex model when driven with disaggregated meteorological data. And so, the use of disaggregated drivers satisfies our previous hypothesis: the propagation of driver data uncertainty impacts the two models to a similar degree.

Although selected as a calibration site, the GPP generated at Lonzee was a notable exception to the high correlation between the ACM and SPAc estimates, which can be attributed to the ACM temperature-linked photosynthesis switch that prevents photosynthesis when the daily average temperature was < 0.0°C. By preventing photosynthesis and, hence C accumulation, during cold days this ACM modification was effective at delaying crop development. However, the Lonzee growth season had a large number of days where the average temperature was < 0.0°C; furthermore these days coincided with key crop developmental stages. On the other hand, SPAc uses half-hourly drivers to simulate leaf-level processes within multiple canopy layers, and thus resolves photosynthesis at much finer temporal resolutions. Although the daily average temperatures used by ACM were less than 0.0°C, a large proportion of the disaggregated half-hourly time-series was greater than 0.0°C; therefore SPAc continued to simulating photosynthesis for some of the half-hourly periods during these days.

The bias range across individual site estimates was much larger for SPAc when compared to ACM (Table 3.5). We deduce this bias is a consequence of biases in the original Princeton reanalysis product, which was temporally (3-hourly) and spatially (1.0˚) aggregated. These biases would have propagated into the SPAc model at a higher frequency when compared to ACM, which corresponded to larger biases in SPAc photosynthesis estimates. In spite of this, the overall ACM and SPAc relationships to FLUXNET estimates were similar in terms of accuracy and biases. As was the case for the ACM and SPAc comparison, there was a positive increase in the mean bias when applying the multi-site calibration at the validation sites. However, comparisons of ACM to FLUXNET estimates at the calibration and validations sites also showed a similar correlation and error. And so, a simpler model can produce reliable estimates of photosynthesis even when driven with coarse-scale meteorological data.

3.4.4. Limitations and implications for future research

We acknowledge that the sites/seasons selected for analysis in this study are by no means representative of winter cereal crop conditions as a whole. However, the spatial distributions of the eight sites do span a relatively large area of western-central Europe; therefore, we would anticipate a similar model performance when applied at alternative winter wheat sites within this geographical extent. Although we equally divided eight sites for calibration and validation, due to the scarcity of European field-scale observations of cereal crop meteorology and photosynthesis, the multi-site ACM calibration could not be substantially validated against data from independent field sites. Nonetheless, we hypothesise that a similar accuracy in photosynthesis predictions could be achieved if the multi-site ACM calibration was applied at alternative western-central European winter wheat sites.

Generally, outputs from driving ACM with estimates from the applied disaggregation routine were promising. Given the wide-scale (global) coverage of the Princeton 1.0° 3-hourly reanalysis product used here, this shows potential for the spatial upscaling of ACM. It is also worthy of note, that errors existing in the SPAc model, due to parameter uncertainty and inadequacies in process understanding (see evaluation in Sus *et al.*, 2010), would have invariably transferred to ACM through calibration. However, we anticipate that a reduction in model uncertainty, along with improvements in predictions, could be achieved by combining ACM with additional observations within a model-data fusion framework. For instance, the research presented in Chapter 2 using SPAc has demonstrated that the sequential assimilation of Earth observation (EO) derived LAI estimates improves the estimation of C fluxes. However, the simplicity of ACM compared to SPAc, particularly in terms of computational demand, offers a more practical means of updating state variables through such data assimilation schemes involving a large ensemble of model runs.

3.5. Conclusion

Previous approaches to simulating the crop C cycle have used detailed models operating at fine spatial and temporal scales, with extensive and often uncertain parameterisations in order to resolve leaf-level processes. As a result, the spatial upscaling of these models is highly susceptible to errors and constraints stemming from fine temporal scale meteorological driver data and site-specific parameterisations. The computational costs of complex models also prohibit ensemble crop C cycle analyses at continental-scales. To this end, we evaluated the use of a simplified model framework that simulates aggregated canopy processes using comparatively coarse temporal scale meteorological data. We further reduced model complexity by applying a generic multi-site photosynthesis calibration and used disaggregated drivers instead of local observations.

Outputs from the simplified model using a multi-site calibration closely reproduced (range in RMSE 0.98 to 3.78 g m^{-2} d^{-1}) those of the more complex SPAc model when both models are driven with either local or disaggregated data. This strong relationship between the two models also existed when the multi-site calibrated model was evaluated at independent sites. Similar results were achieved when comparing the two models to site-level EC data. However, due to parameter uncertainty and meteorological driver availability, we argued that the use of simpler models with reduced parameterisation are more favourable for further studies involving the spatial upscaling of crop C simulations. Additionally, the increased computational efficiency, as a consequence of a decrease in model complexity, is more applicable for model-data fusion experiments that would potentially enhance the representation of cropland C fluxes.

3.6. Summary

This research has demonstrated the use of a simplified model (i.e. ACM) for simulating photosynthesis within cropland ecosystems. ACM was calibrated and evaluated – based on photosynthesis estimates generated by the more complex SPAc model and EC data – at the winter cereal crop FLUXNET sites used in Chapter 2. The validity of ACM when driven with course spatial and temporal scale meteorological data is further tested. Single-site and multi-site ACM calibrations had a high agreement with the SPAc estimates. From individually comparing the ACM (multi-site calibration) and SPAc photosynthesis predictions to FLUXNET estimates, the errors in the photosynthesis estimates were similar when both models were driven with the course-scale meteorological data. Therefore ACM – requiring only daily spatially aggregated meteorological drivers – can reliably reproduce the output from a more complex model.

And so, the next chapter (Chapter 4) exploits the simplicity of ACM (i.e. operating at higher computational speeds using reduced input parameters) for the estimation of winter wheat crop C stocks and fluxes at region-scales.

CHAPTER 4

Model-data fusion approaches for the regional and multi-annual assessment of UK winter wheat yields

Declaration

The research presented in Chapter 4 has been adapted from a paper, of which Andrew Revill is the first author with Mathew Williams as co-author, submitted for review in the *Agricultural and Forestry Meteorological* journal on the 21st August 2015 and is currently in revision. The model application and evaluation was performed by A. Revill with advice from M. Williams. The manuscript was written by A. Revill with edits by M. Williams.

4.1. Introduction

Variations in crop yield are strongly influenced by climate (Hansen, 2002; Osborne and Wheeler, 2013), however the specific impacts of climate on yield remains uncertain (Tubiello *et al.*, 2007). Cropland ecosystems are also entirely managed with human interventions applied on a range of spatial and temporal scales (Porter and Semenov, 2005; Reichstein *et al.*, 2013); causing further uncertainty when investigating feedbacks between climate and crop growth (Smith *et al.*, 2010; Sus *et al.*, 2010). However, understanding the complexity of agricultural production at a regional-scale, including the environmental interactions, is essential for policy-makers concerned with food security and climate change (Becker-Reshef *et al.*, 2010; Lobell and Burke, 2010; Ewert *et al.*, 2011; Hawkins *et al.*, 2013; Li *et al.*, 2014).

Crop models integrate multiple crop physiological mechanisms – simulating the key interactions between soil, vegetation, management and climate (Wattenbach *et al.*, 2010; Martre *et al.*, 2015). The models, driven by meteorological data, can estimate daily crop growth and are a powerful tool for evaluating the causes of variability in crop carbon (C) dynamics, including yield (Wong and Asseng, 2006; Coucheney *et al.*, 2015).

Typically, crop models are developed and calibrated at field-scales under the assumptions of homogenous field conditions (Balkovič *et al.*, 2013), therefore their regional application is complicated by factors concerning input data requirements and parameter uncertainty. Specifically, the models often require a large number of input data on crop cultivar, soil characteristics and management information that, due to the complexity of cropping patterns over agricultural landscapes, are often uncertain or unavailable (Kogan *et al.*, 2013; Ma *et al.*, 2013; Huang *et al.*, 2015). When compared to standard land-surface models, detailed crop models that simulate leaf-level processes, such as the Soil-Plant-Atmosphere crop model (SPAc, Sus *et al.*, 2010), involve extensive and uncertain parameterisations that are difficult to calibrate (Lobell and Burke, 2010; Valade *et al.*, 2013; Huang *et al.*, 2015). To evaluate leaf-level processes (e.g. photosynthesis), complex models also operate at fine temporal scales (e.g. hourly time-steps); thus making the models computationally intensive when calibrating parameters through an ensemble of runs over multiple points and growing seasons.

Satellite Earth observation (EO) sensors offer a synoptic and repetitive coverage – providing temporally consistent information on crops over large geographical extents (Dente *et al.*, 2008; Chen *et al.*, 2011). Atzberger (2013) discusses areas where EO derived data can support the analysis of crops, including yield forecasting, phenological monitoring and the mapping of crop types and distributions. There is also a growing volume of standardised EO products, most notably MODIS leaf area index (LAI) estimates (Knyazikhin *et al.*, 1998; Yang *et al.*, 2006), thus allowing for a regional-scale analysis over multiple crop growing seasons. Through empirical regression, studies have directly used EO data for forecasting regional crop yields (e.g. Becker-Reshef *et al.*, 2010; Mkhabela *et al.*, 2011; Kogan *et al.*, 2013). However, empirical approaches are typically calibrated using historical observations; consequently they may only be applicable for a specific growth season, crop cultivar, developmental stage or geographical location (Fang *et al.*, 2011; Ma *et al.*, 2013; Huang *et al.*, 2015; Lobell *et al.*, 2015).

The assimilation of EO data into crop models has been applied to enhance the simulation of C dynamics, including yield and net land-atmosphere C fluxes (e.g. De Wit *et al.*, 2012; Revill *et al.*, 2013; see Chapter 2; Sus *et al.*, 2013; Zhao *et al.*, 2013). High temporal resolution EO sensors, such as MODIS (e.g. 8-day LAI estimates), are essential for precise crop growth monitoring applications in order to capture the key developmental stages (Launay and Guerif, 2005; Whitcraft *et al.*, 2015).

Studies assimilating MODIS data have been conducted in North America where the average field size is at least comparable to the 1 km resolution LAI product. For example, Fang *et al.* (2011) achieved a reasonable agreement with official statistics when assimilating MODIS LAI into the CERES-Maize model for estimating corn yields in Indiana with reported field sizes of around 240 ha. Ines *et al.* (2013) assimilated MODIS LAI into the DSSAT-Crop model and reduced errors in yield estimates when compared to multi-annual (2003-2009) statistics for Iowa. However, to accurately resolve the detail within small (< 25 ha) fields, such as those that are characteristic of European croplands, the use of MODIS LAI is challenged by sub-pixel heterogeneity (Doraiswamy *et al.*, 2004; Duveiller and Defourny, 2010). And so, as opposed to using MODIS LAI directly in a sequential data assimilation (DA) framework (such as that detailed in Chapter 2), alternative variational assimilation approaches have combining models and EO data to calibrate phenological parameters (e.g. minimum temperature, Xu *et al.*, 2011) or management-related information (e.g. sowing or emergence date, Brown and de Beurs, 2008; Sus *et al.*, 2013).

In 2013, the UK was the eighth largest producer of cereal crops (predominantly winter wheat) in the European Union (Eurostat, 2015). Cereal crops also account for around 50% of the UK cropland area (DEFRA, 2015). Studies evaluating the performance of crop models against extensive time-series of European regional yield statistics (e.g. Balkovič *et al.*, 2013) are rare. Furthermore, to our knowledge, studies combining models with EO data – specifically for UK regional yield and net C flux estimates – are non-existent. To this end, here we conduct a spatially explicit approach for multi-annual (2000-2013) winter wheat yield estimates at UK regional-scales by integrating agricultural census data, MODIS LAI and a crop model. Our specific objectives are to: first, quantify the relationship between MODIS LAI and official regional yield data. This established relationship further allows us to test a filtering method for refining the selection of winter wheat crop areas derived from merging multi-temporal census data. Second, assess the spatial upscaling of crop model estimates generated at local scales (1 km) for reproducing the regional yield statistics. Third, through constraining the simulated phenology during the vegetative period, we evaluate the fusion of the model with the MODIS LAI for yield estimates in a DA framework. We further assess this model-data fusion method by establishing a relationship between the simulated net C fluxes and yield statistics. The following research questions are addressed:

1) What is the empirical relationship between MODIS LAI and crop yields across UK regions?

2) What is the accuracy of crop model yield estimates at the grid-scale when aggregated to regional-scales?

3) Can MODIS LAI be used to constrain and improve the model estimates of yield and net C fluxes?

The novelty of this research is the combined use of a crop-specific model and EO data for resolving UK regional crop yield and net C fluxes over a 14-year period. A further innovation is the regional application of the simplified photosynthesis model – calibrated and evaluated in Chapter 3 – that uses only daily meteorology drivers; therefore minimising the model complexity associated with computational demand and input driver data requirements.

4.2. Data and Methods

First, a brief overview of the study regions is presented, followed by a description of the data used to parameterise, drive, calibrate and validate the regional application of the model framework. Second, an overview of the crop C budget modelling approach is given. Third, the technique used to constrain the crop model canopy development simulation is provided, along with the experimental design used to evaluate the performance of the model-data fusion.

4.2.1. Study regions

This research focuses on multi-annual (2000-2013) winter wheat (*Triticum aestivum*) crop production across six UK administrative regions: East Midlands, West Midlands, Yorkshire & the Humber, North East, South East and Eastern England. These specific regions were selected as they were identified as the most dominant UK wheat producing regions from a 2013 survey conducted by the UK Department for Environmental Food and Rural Affairs (DEFRA, 2013).

4.2.2. Data description and pre-processing

Spatial datasets

To provide spatial estimates of annual wheat crop areas, we used the Agcensus datasets developed by Edinburgh University Data Library consisting of DEFRA Agricultural Census results aggregated to 2 km grid squares. Specifically, we used the wheat crop and total cereal crop area Agcensus data categories, which were available for the years 2000, 2004 and 2010 only. In order to minimise the impacts of spatial and temporal variability, using a Geographical Information System (GIS) we first selected 2 km cells where the estimated wheat growing area was greater than 50% of the total cereal crop area; this process was repeated for each of the three annual datasets. Through GIS overlay analysis, we further reduced the grid cell selection to those that only existed across all three years. Essentially we merged the three datasets to produce a single spatially and temporally consistent gridded dataset that delineated the dominant (i.e. > 50%) wheat crop producing areas. Therefore, it was assumed that wheat production was dominant at these selected 2 km^2 cells across the entire study period (2000-2013).

MODIS LAI data processing

The MODIS LAI data product (combined Terra and Aqua product; Level-4 MCD15A2) was sourced from the NASA Reverb Earth Observing System Data and Information System (EOSDIS, 2009). This LAI data, consisting of 8-day composites at 1 km resolution, was extracted to cover the selected 2 km cells of the merged census dataset over the entire 14-year study period. Consequently, there were approximately four MODIS time-series points for each of the cells per year. Using the available MODIS Quality Assurance (QA) data on cloud status, we also applied a filter to include only observations on days that were not flagged as cloudy and that the main retrieval algorithm provided the best possible results at the time of acquisition. In order to ensure that an LAI value was available for each day of the wheat crop growing season, cubic spline interpolation was also applied to the filtered MODIS LAI time-series.

Regional crop yield data

To quantify the empirical relationship between the MODIS LAI and yield, and to evaluate the regionally aggregated crop model estimates, official statistics on UK regional wheat yields (tonnes/hectare, $t\ ha^{-1}$) were sourced from DEFRA (DEFRA, 2015) for the full study period (i.e. 2000-2013). These were derived from the reported wheat production and area that was collated during DEFRA's annual agriculture surveys. We further applied a correction to the yield statistics to remove moisture content, which is standardised by DEFRA to be 14.5% for all cereal crops.

Meteorological driving data

In order to drive the crop model used in this research, meteorological data was acquired for each of the 1 km MODIS LAI points. These meteorological drivers were sourced from the 1 km resolution gridded Climate, Hydrology and Ecology research Support System (CHESS) dataset, which was developed by the Centre for Ecology and Hydrology (CEH, 2014). Specifically, daily estimates of minimum and maximum temperature and surface downwelling short-wave radiation were retrieved from CHESS.

Crop Calendar Dataset (CCD)

Information on management dates – specifically the sowing and harvest date, which was required to initialise the regional application of the crop model – was sourced from the gridded (5' x 5') CCD developed by Sacks *et al.* (2010). The CCD is a single global dataset that was produced based on the relationship between archived climate statistics and observed management dates. For this study, the average sowing and harvest dates for winter wheat – being 31st September (day 304) and 27th July (day 208), respectively – were the same across all UK regions. In spite of this, since our model approach accounts for winter cereal crop dormancy (i.e. vernalisation) and senescence, we do not anticipate a high sensitivity to sowing/harvest dates at regional-scales.

Empirical regression-based analysis

We determined the relationship been annual DEFRA yield and the maximum MODIS LAI through regression-based analysis for each of the six regions. Past regression models relating vegetation indices to yield differ depending on factor including crop type and environmental conditions (Mkhabela *et al.*, 2011). However for cereal crops, research in Forbes and Watson (1992), along with a preliminary analysis conducted using sample data in this study, revealed a reasonable correlation between the maximum LAI of cereal crops and yield. Therefore, for each region, we aggregated the MODIS LAI data by first calculating the maximum LAI estimate per year for each of the selected 2 x 2 km grid cells. Second, we calculated the mean maximum LAI across all cells per year and region. Consequently, for each of the six regions, this procedure generated one mean maximum LAI value per year. The regression analysis was then applied to evaluate the annual regional yields with the aggregated MODIS LAI.

Knowledge-based MODIS LAI point filtering

Given the scale mismatch between the 2 km resolution wheat area map and the 1 km MODIS LAI, the selection of MODIS LAI points was filtered for each year. As the spatial and temporal extents of this analysis are relatively large, reducing the number of MODIS LAI points through filtering is also favourable in terms of computational efficiency. This filtering involved combining an analysis of the full range in LAI time-series with a knowledge of winter wheat phenology under UK environmental conditions. In order to reduce the MODIS LAI uncertainty due to land cover misclassification, research in Zhao *et al.* (2013) involved the removal of maize crop sites based on the maximum MODIS LAI value. Similarly, in this research we analysed the MODIS LAI time-series at each point and removed points that were not considered representative of winter wheat. Using crop growth observations detailed in Sylvester-Bradley *et al.* (2008), the filtering criteria was based on two conditions: 1) maximum LAI must not exceed 7.5 m^2 m^{-2}, and 2) the monthly mean LAI values must increase progressively from February to April. MODIS time-series that did not meet the filter criteria were therefore excluded from subsequent analysis.

4.2.3. Data Assimilation Linked Ecosystem Carbon crop (DALECc) model

DALECc model description

To simulate the impacts of meteorological conditions on crop growth and yield, we apply the DALECc model at the filtered 1 km MODIS LAI points within each region. DALECc is the C allocation scheme used in the more detailed SPAc model (Sus *et al.*, 2010), which has previously been described and evaluated at the plot/field scales in Chapters 2 and 3.

The DALECc model structure (see Chapter 3: Figure 3.3) consists of C pools/stores that are linked by allocation fluxes (i.e. rate of C allocated to plant tissues) or litterfall fluxes (i.e. rate of C removed from tissues). The model simulates cropland ecosystem C mass-balance and allocation at daily time-steps when driven by predictions of gross primary production (GPP), which is simulated using the Aggregated Canopy Model (ACM, Williams *et al.*, 1997). The net primary production (NPP) is estimated based on the GPP remaining after subtracting autotrophic respiration. In this research, we fix the autotrophic respiration fraction for winter wheat to 0.44 (Monje and Bugbee, 1998). The NPP is then partitioned according to a crop-specific C allocation scheme, which consists of an empirically-derived look-up table (see Penning de Vries *et al.*, 1989) defining the specific fractions of NPP that are allocated to the plant organs (i.e. foliage, stem, storage and root). The allocation fractions assigned at each time-step are a function of developmental stage (DS), ranging from -1 (sowing) to 2 (maturity). The DS is calculated based on the accumulation of daily development rates (DR), which in turn are determined from the key developmental responses: temperature $f(T)$, photoperiod $f(P)$ and vernalisation $f(V)$ (Streck *et al.*, 2003; Sus *et al.*, 2010).

$$DR = DR_{max} \times f(T) \times f(P) \times f(V) \qquad \text{Equation 4.1}$$

where DR_{max} is the maximum possible developmental rate parameter. It is assumed that DR_{max} is different in the pre-anthesis (DR_{pre}, i.e. vegetative stages, where DS <1) and post-anthesis (DR_{post}, i.e. reproductive stages, where DS >1) phases (Streck *et al.*, 2003). Furthermore, in the vegetative stages DR is calculated using $f(T)$, $f(P)$ and $f(V)$ (until emergence only), whereas only $f(T)$ is used during the reproductive stage.

In addition to estimating the regional yield, DALECc was also used to quantify the net C fluxes. Specifically, we estimate the daily net ecosystem exchange (NEE), i.e. NEE equals NPP minus heterotrophic respiration. The heterotrophic respiration is the sum of the temperature dependant respiration fluxes from animals and microbes.

ACM photosynthesis model description

ACM operates within DALECc to provides estimates of GPP from daily inputs of global radiation (MJ m^{-2} day^{-1}), atmospheric CO_2 (ppm), leaf area index (LAI, m^2 m^{-2}) and maximum and minimum temperature (°C). To generate GPP from these drivers, ACM consists of a series of aggregation equations that use a set of fixed variables and 10 unitless coefficients (see Appendix sections B1 and B2 for further details). These coefficients, previously calibrated for winter wheat crops (as detailed in Chapter 3), create a response surface that scales the daily accumulation of half-hourly SPAc GPP in order to predict whole-canopy GPP using only coarse-scale (daily) driving data. In essence, ACM is designed to capture and emulate the detail behaviour of the SPAc leaf-level photosynthesis routines whilst operating at a reduced temporal scale (i.e. daily instead of half-hourly time-steps).

4.2.4. DALECc phenology calibration

We adjust the DALECc simulation of developmental rate based on the MODIS LAI time-series. Specifically, this calibration entailed adjusting the maximum developmental rate during pre-anthesis only (DR_{pre}), i.e. the DR_{post} parameter remained fixed. The crop development is partly expressed through LAI, which is proportional to the foliar C pool (via leaf carbon per area). Therefore, varying the DR_{pre} parameter changes the developmental rate; thus impacting the DALECc LAI estimates during the vegetative period that can be directly compared to MODIS LAI.

We use a Metropolis-Hastings Markov Chain Monte Carlo (MHMCMC) approach (e.g. Xu *et al.*, 2006; Hill *et al.*, 2012; Ziehn *et al.*, 2012; Bloom and Williams, 2015; amongst others) to calibrate DR_{pre}. Where the likelihood function for the DR_{pre} value x given the MODIS LAI values c, $p(c|x)$, can be expressed as follows:

$$p(c|x) = e^{-0.5 \cdot \sum_i \frac{(M(x)-c)^2}{\sigma_{modis}^2}} \quad \text{Equation 4.2}$$

where $M(x)$ is the DALECc LAI based on the DR_{pre} value x, and σ_{modis} is the Gaussian uncertainty assigned to the MODIS LAI: σ_{modis} was set to 2.0 m^2 m^{-2} based on a previous analysis between MODIS LAI and field measurements of LAI at winter wheat sites available through the Global FLUXNET database (fluxnet.ornl.gov). In accordance with Bayes' theorem, based on the likelihood function $p(c|x)$ the probability density function (PDF) of x given MODIS LAI values c, $p(x|c)$, can be expressed as follows:

$$p(x|c) \propto p(c|x) \cdot p(x) \quad \text{Equation 4.3}$$

where, $p(x)$ is the prior probability of x. We prescribe a log-uniform prior DR_{pre} of 0.04 (as detailed in Streck *et al.*, 2003) along with minimum and maximum values, set to 0.009 and 0.5, respectively. This DR_{pre} range was determined from some preliminary runs whereby the bounds were progressively increased until the accepted parameter space was unconstrained. To determine $p(x|c)$ (i.e. the range of likely DR_{pre} values), we use the MHMCMC to draw 5000 samples of x, from which the probability distribution $p(x|c)$

can be adequately approximated.

Per region, we apply this MHMCMC calibration of DR_{pre} at each of the knowledge-based filtered 1 km points. A single regional posterior DR_{pre} is then retrieved per year by selecting the median value from the most likely DR_{pre} parameter in the distribution of samples generated at each of the 1 km points. And so, we assume a fixed DR_{pre} parameter per region for each year.

4.2.5. Experimental design and evaluation

We evaluate the linear fit of the regional DEFRA yield to the mean maximum MODIS LAI based on the slope and R^2 regression statistic (least-squares coefficient of determination). This analysis was also carried out both with and without the knowledge-based filtering applied to the MODIS LAI in MATLAB (version: R2012a).

To assess the performance of DALECc, we initially aggregated the model outputs (i.e. from 1 km grid-scale to regional-scale) by calculating the mean maximum LAI, mean yield and the mean cumulative NEE (i.e. the sum of daily NEE between sowing and harvest date) of the grid scale estimates for each region and year (Figure 4.1). Metrics were then calculated to quantify the relationship between the mean maximum LAI values and the mean maximum MODIS LAI from the knowledge-based filtered points; whereas the regional mean yield estimates were compared to the DEFRA yield. In addition to the R^2 value, these metrics included the root-mean-square-error (RMSE) describing the average estimated-measured differences and the normalised mean bias (NMB) quantifying model over- or under-estimations. In order to evaluate the use of MODIS LAI as a model constraint, we compared the aggregated model outputs when DALECc was run with the nominal (i.e. prior) DR_{pre} and posterior DR_{pre} separately (i.e. before and after the DR_{pre} calibration).

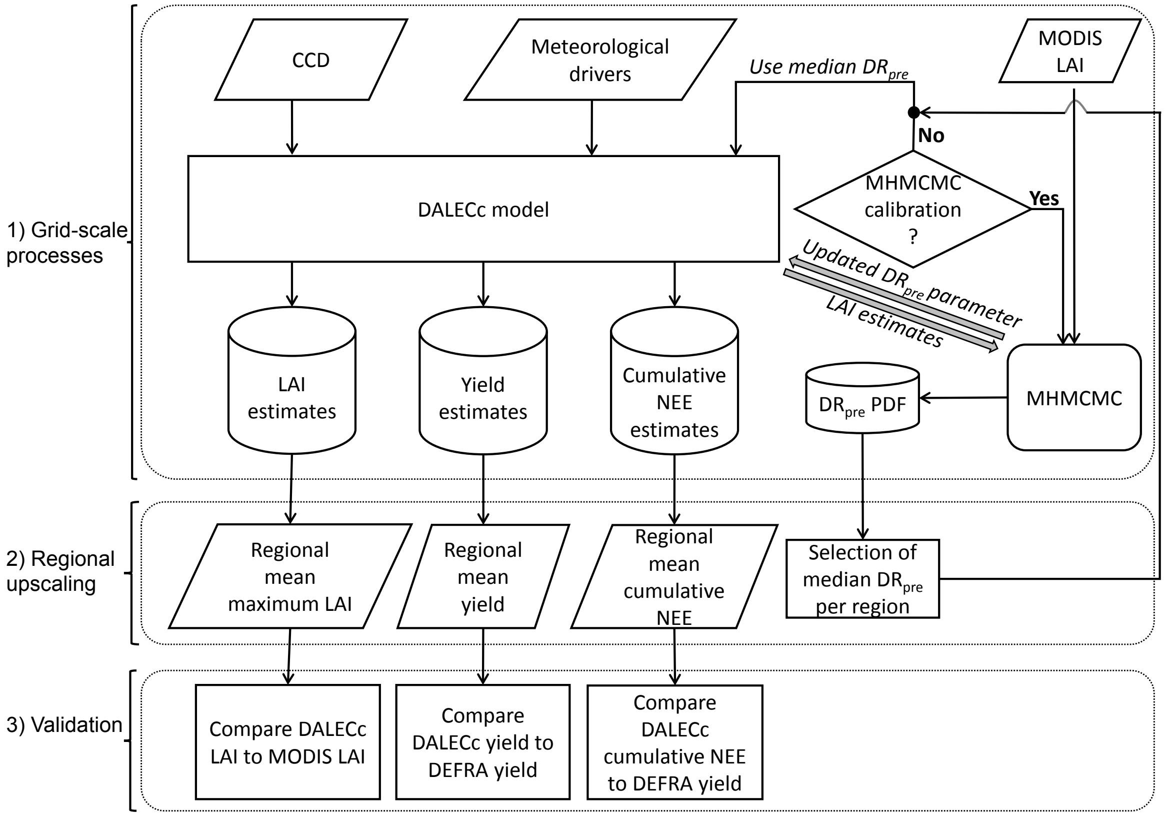

Figure 4.1: Schematic summarising the model-data fusion framework for combining and evaluating the use of DALECc and MODIS LAI for the regional estimation of crop yields. 1) Grid-scale (1 km) processing involved generating drivers and initialising the DALECc model: extraction of sowing and harvest dates from a Crop Calendar Dataset (CCD) and daily meteorological drivers (temperature and short-wave radiation) from the CHESS dataset. If the development rate during pre-anthesis parameter (DR_{pre}) is being calibrated, we combine the DALECc LAI from an ensemble of runs with MODIS LAI within a Metropolis-Hastings Markov Chain Monte Carlo (MHMCMC) data assimilation algorithm, which generates a probability distribution function (PDF) of likely DR_{pre} values. Alternately, DALECc can be run once using the regional median value from a previously generated PDF of DR_{pre} values. 2) DALECc outputs at the grid cells are regionally upscaled by selecting the mean LAI and yield values. From the MHMCMC PDF the median of the most likely DR_{pre} value per year was selected as the calibrated value and re-used to run DALECc. 3) Validation of the DALECc LAI and yield estimates by comparing to MODIS regional mean LAI and DEFRA yield statistics, respectively.

4.3. Results

The linear correlation between DEFRA yield statistics and the mean maximum MODIS LAI is first evaluated here. Second, the DALECc model estimates of LAI, yield and cumulative NEE are presented both with and without the DR_{pre} calibration.

4.3.1. Empirical analysis of MODIS LAI to DEFRA yield statistics

The mean maximum MODIS LAI had a weak correlation (mean $R^2 = 0.27$) with the DEFRA yield statistics (Figure 4.2 and Table 4.1). This correlation was only slightly improved when applying the knowledge-based filtering (mean $R^2 = 0.29$). The Eastern England region, which had the largest proportion of wheat crop area, had a correlation of $R^2 = 0.34$ (unfiltered) and $R^2 = 0.37$ (filtered).

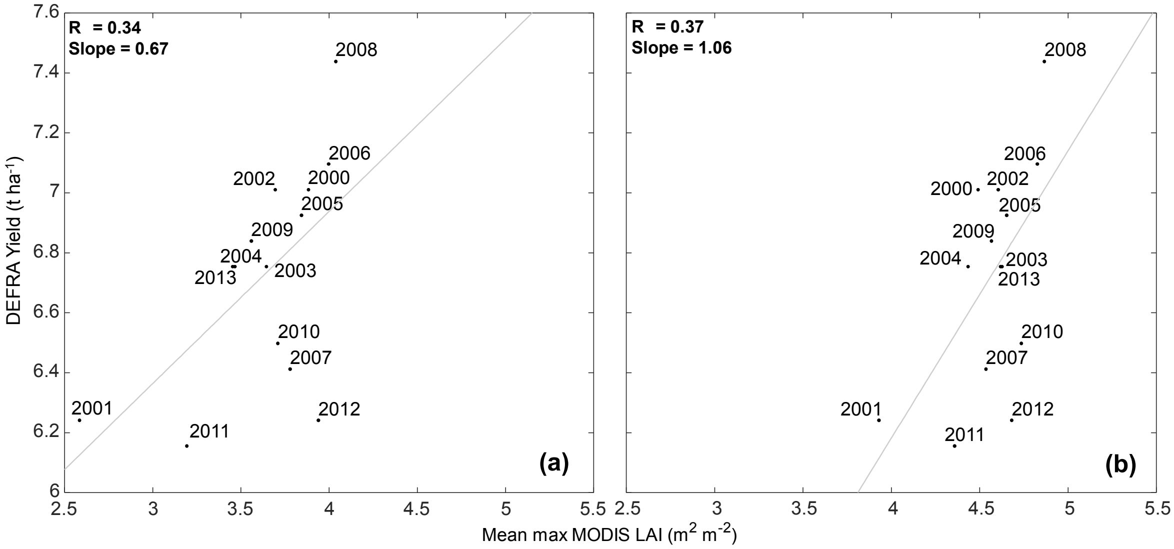

Figure 4.2: Regression analysis between DEFRA yield and the mean maximum MODIS LAI shown for the Eastern England from 2000 to 2013, including a comparison between the fitted line (grey) for (a) unfiltered and (b) filtered MODIS LAI points.

Table 4.1: Regression analysis statistics from comparing DEFRA yield to the mean maximum MODIS LAI from 2000 to 2013. Including the percentage coverage of dominant (> 50%) wheat area per region as estimated by merging multi-temporal census data and a comparison between the number of unfiltered and filtered MODIS LAI points. Weighted averages, reported for the R^2 and slope of the linear fit, are calculate based on the number of unfiltered and filtered points.

		Unfiltered MODIS			Filtered MODIS		
Region	Estimated Percentage coverage (per region)	MODIS points used per year	R^2	Slope	MODIS points used per year (average)	R^2	Slope
North East	2%	183	0.52	1.11	152	0.59	1.01
West Midlands	3%	471	0.10	0.43	388	0.17	0.62
Yorkshire & Humber	4%	808	0.01	-0.19	416	0.00	0.05
South East	4%	993	0.25	0.79	148	0.28	1.04
East Midlands	13%	2402	0.17	0.74	1447	0.18	0.74
Eastern England	29%	6501	0.34	0.67	3372	0.37	1.06
Weighted average	-	-	0.27	0.63	-	0.29	0.88

From the linear fit for both the unfiltered and filtered points the year 2012 was a notable outlier where the mean maximum MODIS LAI overestimated the yield for all six regions. Although not explicitly tabulated in this paper, as a further investigation we removed the DEFRA yield and MODIS LAI for 2012 and regenerated the linear fit. With the removal of the 2012 data, the correlation was greatly improved with a mean R^2 of 0.52 (unfiltered) and 0.53 (filtered). This increase in correlation with the removal of 2012 data was largest for the West Midlands region, where the R^2 increased from 0.10 to 0.57 (unfiltered) and from 0.17 to 0.57 (filtered).

Although the overall increase in the correlation between the mean maximum MODIS LAI and DEFRA data was small, the knowledge-based filtering resulted in a large reduction in the number of MODIS LAI points. Specifically with the mean annual number of points used in this analysis decreasing by 48%.

4.3.2. DALECc estimates

LAI estimates

From initialising DALECc with the prior DR_{pre} value the correlation between the mean maximum model LAI to that of the MODIS LAI (for the filtered points only) was poor with a mean R^2 of 0.05 (Figure 4.3 and Table 4.2). The RMSE was high (mean RMSE = 2.59 m^2 m^{-2}) and all regions showed a positive NMB (+26% ≤ NMB ≤ +91%) indicating that the aggregated DALECc outputs over-estimated the MODIS mean maximum LAI by an average of 80%.

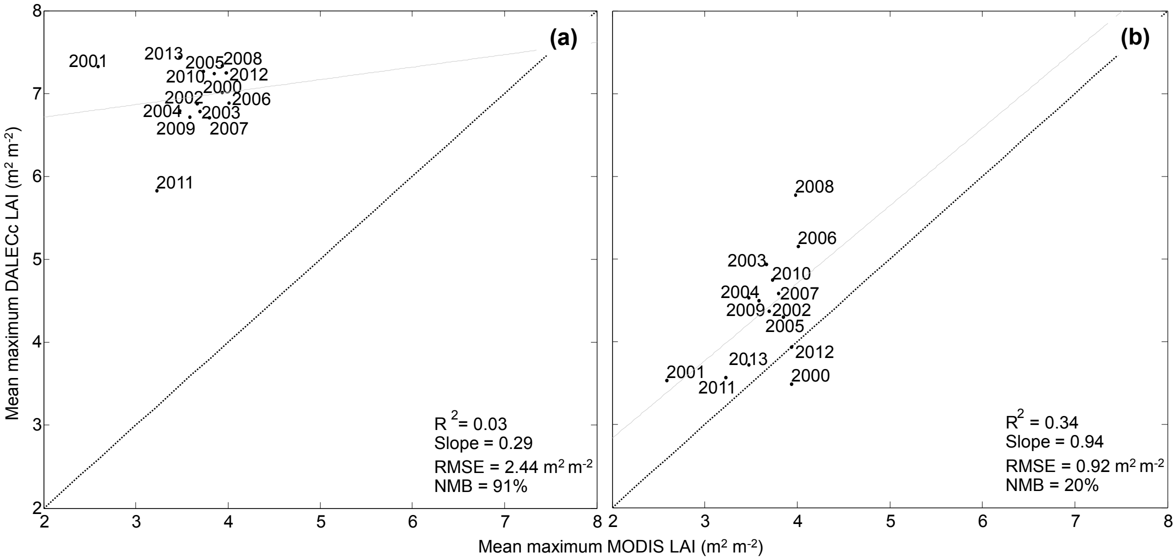

Figure 4.3: Regression analysis between mean maximum DALECc LAI and mean maximum MODIS LAI shown for the Eastern England from 2000 to 2013. Plot includes the fitted (grey) and 1:1 (black dashed) lines to show a comparison between the (a) prior and (b) posterior calibrations of the DR_{pre} parameter.

Table 4.2: Regional regression-based analysis of DALECc mean maximum LAI to MODIS mean maximum LAI, including a comparison between prior and post calibrations of the DR_{pre} parameter. Metrics include: linear fit statistics (R^2 and slope), root-mean-square-error (RMSE) and normalised mean bias (NMB). Weighted averages are calculate based on the number of filtered MODIS points (see Table 4.1).

	Prior DR_{pre}				**Post DR_{pre}**			
Region	**R^2**	**Slope**	**RMSE (m^2 m^{-2})**	**NMB (%)**	**R^2**	**Slope**	**RMSE (m^2 m^{-2})**	**NMB (%)**
North East	0.51	0.98	1.92	28	0.25	0.83	0.85	4
West Midlands	0.18	0.45	2.26	36	0.03	0.26	0.67	-4
Yorkshire & Humber	0.15	0.49	1.84	26	0.02	-0.37	1.25	8
South East	0.03	-0.37	2.23	47	0.41	1.23	0.95	-19
East Midlands	0.00	-0.10	3.34	90	0.50	1.17	0.51	9
Eastern England	0.03	0.29	2.44	91	0.34	0.94	0.92	20
Weighted average	0.05	0.22	2.59	80	0.34	0.86	0.83	14

From running DALECc at each of the points with the posterior DR_{pre} value there was a large improvement in the correlation (mean $R^2 = 0.34$) when compared to that from using the prior DR_{pre}. Using the posterior DR_{pre} also resulted in a large reduction in the mean RMSE, from 2.59 m^2 m^{-2} (prior DR_{pre}) to 0.83 m^2 m^{-2} (posterior DR_{pre}). This reduction in error coincides with a decrease in bias, with the mean NMB reducing from +80% to +14%. This reduction in bias is also indicated by an increase in slope from 0.22 to 0.86 for the prior and posterior DR_{pre} parameters, respectively. Hence, the model-data fusion resulted in a significant improvement in LAI simulations when compared to MODIS.

Comparing simulated and recorded yield estimates

From using the prior DR_{pre} value the correlation between the aggregated DALECc yield estimates and the regional DEFRA yield data was poor, with a mean R^2 of 0.07 (Figure 4.4 and Table 4.3). The mean RMSE was 0.73 t ha^{-1} and all regions showed a negative NMB (-14% ≤ NMB ≤ -3%, mean NMB = -11%) indicating that the aggregated DALECc mean annual yield under-estimated the DEFRA yield.

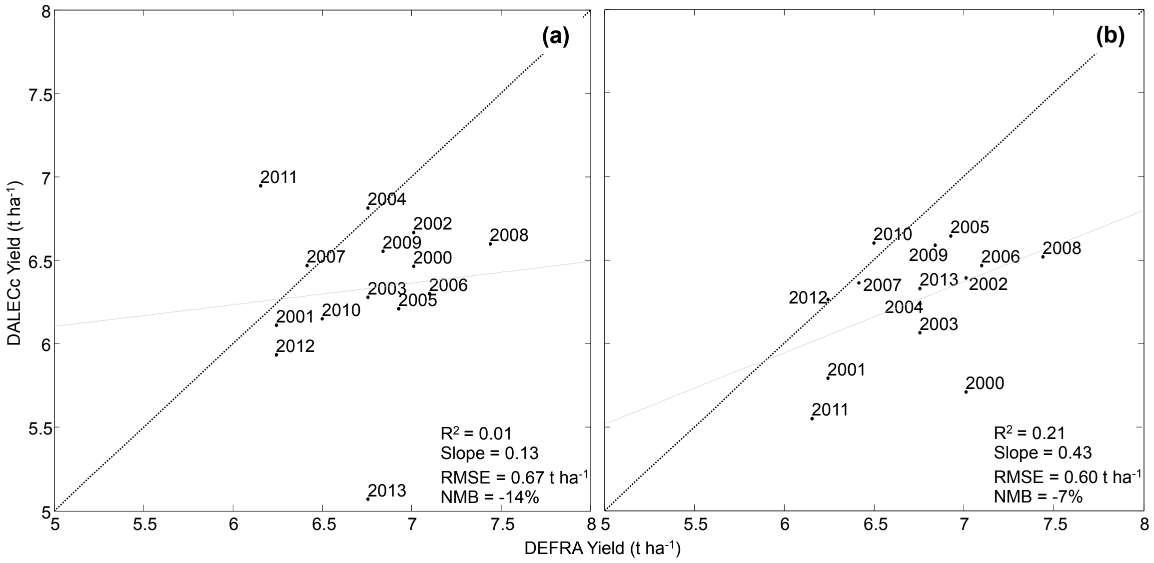

Figure 4.4: Regression analysis between the regional mean yields estimated by DALECc and the DEFRA yield statistics for the Eastern England region from 2000 to 2013. Plot includes the fitted (grey) and 1:1 (black) lines to show a comparison between the (a) prior and (b) posterior calibrations of the DR_{pre} parameter.

Table 4.3: Regional regression-based analysis between the regional mean yields estimated by DALECc to DEFRA yield statistics, including a comparison between prior and post calibrations of the DR_{pre} parameter. Weighted averages are calculate based on the number of filtered MODIS points (see Table 4.1).

	Prior DR_{pre}				Post DR_{pre}			
Region	**R^2**	**Slope**	**RMSE ($t\ ha^{-1}$)**	**NMB (%)**	**R^2**	**Slope**	**RMSE ($t\ ha^{-1}$)**	**NMB (%)**
North East	0.51	0.70	0.69	-8	0.25	0.83	0.85	4
West Midlands	0.18	0.32	0.42	-3	0.03	0.26	0.67	-4
Yorkshire & Humber	0.15	0.35	0.79	-10	0.02	0.37	1.25	8
South East	0.11	0.20	0.79	-11	0.00	0.06	1.04	3
East Midlands	0.03	0.09	0.85	-10	0.07	0.37	0.84	-6
Eastern England	0.01	0.13	0.67	-14	0.21	0.43	0.60	-7
Weighted average	0.07	0.18	0.73	-11	0.12	0.39	0.78	-4

From using the posterior DR_{pre} parameter, there was a slight increase in the mean correlation coefficient between the DALECc and DEFRA yield (mean $R^2 = 0.12$) when compared to that of the prior DR_{pre}. Across all regions, except for the East Midlands and Eastern England, the mean RMSE was increased – with the overall mean RMSE increasing from 0.71 t ha^{-1} to 0.73 t ha^{-1} for the prior and posterior DR_{pre}, respectively. Nonetheless, using the posterior DR_{pre} parameter reduced the overall negative bias in the DALECc yield estimates ($-7\% \leq \text{NMB} \leq 8\%$, mean NMB = -4%). There was also an increase in the mean slope of the linear fit from 0.16 (prior DR_{pre}) to 0.40 (posterior

DR_{pre}). Overall, the model-data fusion of LAI improved the bias and slope, whilst the RMSE was only slightly increased. Additionally, the DALECc yield estimates for 2012 had a much higher agreement with the DEFRA yield when compared to that of the annual mean maximum MODIS LAI.

Comparing cumulative NEE to recorded yield estimates

From comparing the at-harvest cumulative sum of NEE to the DEFRA yield (Figure 4.5 and Table 4.4), there was an overall increase in the correlation coefficient from using the prior DR_{pre} (mean $R^2 = 0.09$) to the posterior DR_{pre} (mean $R^2 = 0.22$). This increase in correlation was most notable for the East Midlands and Eastern England regions, where the mean R^2 increased by 33% and 19%, respectively. For all regions, large differences in the slope of the slope of the linear fit were also observed, with the mean slope reversing from positive (0.29), using the prior DR_{pre}, to a negative regression (-0.74) when using the posterior prior DR_{pre}.

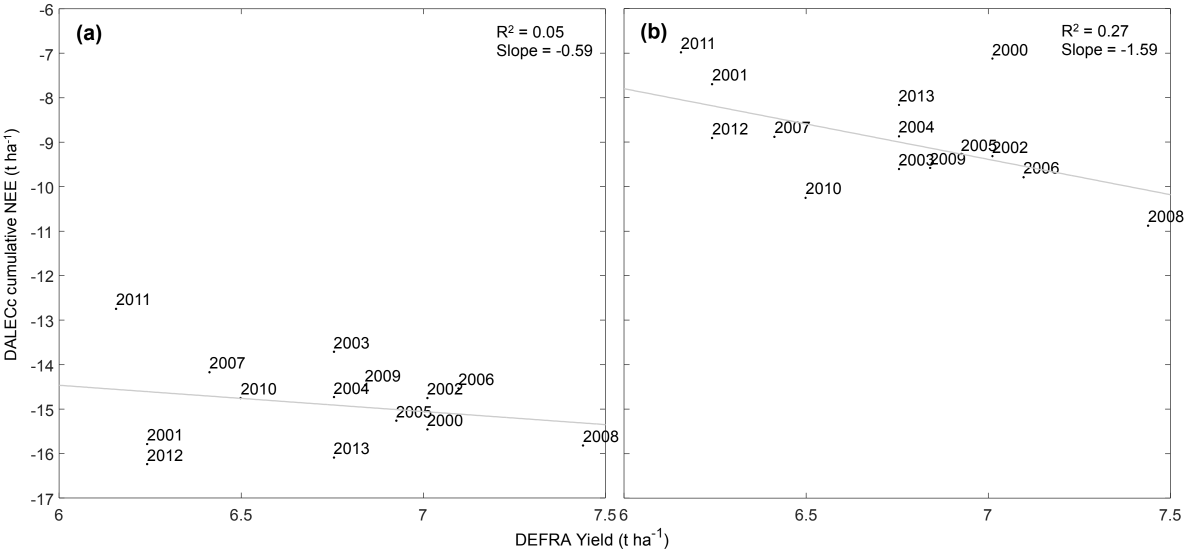

Figure 4.5: Regression analysis between the regional mean cumulative NEE estimated by DALECc and the DEFRA yield statistics for the Eastern England from 2000 to 2013. Plot includes the fitted line (grey) showing a comparison between the (a) prior and (b) posterior calibrations of the DR_{pre} parameter.

Table 4.4: Regional regression-based analysis between the regional mean cumulative (sowing-harvest) NEE estimated by DALECc to DEFRA yield statistics, including a comparison between prior and post calibrations of the DR_{pre} parameter. Weighted averages are calculate based on the number of filtered MODIS points (see Table 4.1).

	Prior DR_{pre}		**Post DR_{pre}**	
Region	**R^2**	**Slope**	**R^2**	**Slope**
North East	0.13	0.74	0.23	-1.17
West Midlands	0.24	1.37	0.22	-0.11
Yorkshire & Humber	0.11	1.07	0.09	0.47
South East	0.19	1.23	0.15	-0.07
East Midlands	0.07	0.58	0.21	-0.37
Eastern England	0.05	-0.59	0.27	-1.59
Weighted average	0.09	0.29	0.22	-0.74

4.4. Discussion

The relationship between the DEFRA yield and the mean maximum MODIS LAI is first discusses. Second, the use of the MODIS LAI for constraining the model estimates is evaluated. Third, a discussion of the limitations and recommendations of the model and spatial datasets used is provided.

4.4.1. Empirical relationship between regional yield and MODIS LAI

This study demonstrated a linear relationship between the mean maximum MODIS LAI and DEFRA yield statistics across a 14-year period. For cereal crops the time of peak LAI coincides with that of flowering and grain filling (Mkhabela *et al.*, 2011), therefore yield is closely correlated with maximum LAI (Forbes and Watson, 1992). And so, the results presented here are consistent with past research, such as that in Mkhabela *et al.* (2011) and Franch *et al.* (2015), which report a correlation between EO-derived maximum vegetation indices and crop yields.

For the year 2012 there was a substantial deviation from the mean maximum MODIS LAI and DEFRA yield relationship as the linear fit over-estimated the yield. On further examination we found that the removal of the 2012 data from this analysis improves the filtered MODIS LAI and DEFRA yield correlation by an average of 45%. This outlier can be attributed to relatively low yields in 2012 that were a consequence of unfavourable weather. These poor meteorological conditions, which lead to high levels of disease during the spring and summer months, included low sunlight levels during the grain filling period (DEFRA, 2012). Given the relatively coarse spatial resolution (1 km) of the MODIS product, it is unlikely that this LAI time-series would have fully resolved these adverse conditions that were specific to the crop vegetation.

Knowledge-based filtering was applied to the MODIS data, which involved removing MODIS points with a corresponding LAI time-series that did not represent the timing of winter wheat canopy development. From applying this filtering only relatively small improvements for each region were achieved in the MODIS LAI and DEFRA yield correlation. However, the filtering also reduced the number of points used per year by an average of 48%. Therefore, since the filtering maintained the MODIS LAI and DEFRA yield relationship, we consider this filtering to be a fundamental step for improving the computational efficiency of the subsequent model-data processing framework. A reduction in computational demand would be particular favourable if, for instance, the MHMCMC algorithm was extended to calibrate multiple model parameters simultaneously or a larger ensemble of model iterations were required to generate accepted parameter estimates.

4.4.2. Using DALECc and MODIS LAI for regional yield estimation

The performance of the DALECc prior and posterior DR_{pre} parameters were evaluated on an individual basis. Using the prior DR_{pre} value we demonstrated a mean error in yield of 0.71 t ha^{-1} when compared to DEFRA data. Similar research in Balkovič *et al.* (2013), involving a European-wide crop model implementation over an 11-year period (1997–2007), reported an average RMSE in winter wheat yield estimates of 1.20 t ha^{-1}. DALECc therefore compares favourably with these more complex models.

The yield was under-estimated by DALECc for all regions; whereas the mean maximum LAI was over-estimated when compared to the MODIS LAI. Since yield is proportional to maximum LAI (Forbes and Watson, 1992), we would have hypothesized that if LAI was over-estimated so too would be the yield; therefore this result was unexpected. This inconsistency can be attributed to the development-linked C allocation scheme used by

DALECc. In the early developmental stages – during the vegetative phase – a relatively large proportion of the net primary productivity is allocated to the leaves of the crop; whereas allocation to the storage organ (i.e. the grain) does not dominate until the later reproductive phase. DALECc also simulates senescence due to self-shading, which is a function of leaf area, i.e. senescence occurs if LAI is higher than a threshold value (set to 4.0 m^2 m^{-2}). Consequently, high LAI (i.e. above the threshold value) increases the rate of senescence and effectively shortens the later reproductive period, thus causing less C to be allocated to the storage organ.

We previously noted that from the mean maximum MODIS LAI and DEFRA yield analysis the MODIS LAI over-estimated the yield for the year 2012. However, this anomaly did not occur in the DALECc yield estimates. The DALECc drivers include daily global radiation and therefore would have accounted for the low sunlight levels during the grain filling period, which was partly responsible for the relatively low 2012 wheat yields (DEFRA, 2012).

Using the posterior DR_{pre} parameter slightly increased the error in the yield estimates (mean RMSE = 0.73 t ha^{-1}); however, when compared to results from using the prior DR_{pre} value, the bias in the yield estimates was reduced for the majority of regions. This overall reduction in bias coincides with a reduction in the bias of the LAI estimates when compared to the MODIS LAI for all regions. As previously noted, by causing the crop to senesce too early (via self-shading from increasing LAI) the prior DR_{pre} parameter had the consequence of reducing the yield. However, by calibrating the DR_{pre} parameter we reduced the rate of crop development during the vegetative period thus decreasing the rate of senescence. Decreasing the senescence rate had the impact of extending the reproductive phase of the crop, which in turn allowed more C to be allocated to the storage organ. Specifically, with the prior DR_{pre}, the simulated vegetative and reproductive phase durations were 95 and 22 days, respectively. However, with the posterior DR_{pre}, the vegetative period was reduced to 50 days and the reproductive phase was increased to 34 days.

In addition to the DALECc yield estimates, we compared the simulated cumulative NEE (i.e. sum of daily NEE estimates between sowing and harvest) to the DEFRA yield. It would have been hypothesised that since a proportion of the NPP is allocated to the storage organ there would be a relationship between the NEE and DEFRA yield. Since the posterior DR_{pre} parameter allowed more C to be allocated to the storage organ a weak negative correlation was observed; where a decrease in the cumulative NEE (i.e. increase in the ecosystem's C uptake) corresponded to larger DEFRA yields. However, this trend was not observed when using the prior DR_{pre} where a smaller proportion of C is allocated to the storage organ.

4.4.3. Limitations and recommendations

DALECc model

The model-data fusion method was successful at reducing the errors and positive biases in the DALECc and MODIS LAI correlation for all regions. Therefore, the over-estimation of DALECc LAI (i.e. without constraining the phenology) highlights limitations with the nominal parametrisations used for simulating winter wheat; particularly those governing the developmental rate during the vegetative period. However, since the DALECc developmental parameters have only been evaluated at field-scales (see Sus *et al.*, 2010; Wattenbach *et al.*, 2010), a regional-scale application of the model using the same parameterisations would have been expected to be uncertain.

The weak correlation between the DALECc and DEFRA yield – existing both with and without the calibration of DR_{pre} – indicates that the model is unable to capture the inter-annual variability in yield. During the reproductive phase (i.e. during maximum C allocation to the storage organ) the DALECc daily developmental rate is determined by the temperature response function, which uses fixed cardinal temperatures. However, at regional-scales cropland landscapes present a broad range of cultivated wheat species, each having different temperature thresholds (i.e. minimum, maximum and optimal temperature) requirements for development. This variability in temperature sensitivity causes uncertainty when calculating the developmental rate during yield formation. Specifically, from calibrating the DayCent model, Rafique *et al.* (2015) demonstrated that corn yield estimates were highly sensitive to a maximum temperature dependency parameter. Therefore, an approach for resolving this limitation in DALECc would include extending the model-data fusion approach to calibrate the maximum developmental rate during post-anthesis (i.e. DR_{post}), which would effectively scale the temperature response function.

Land cover and EO data

Through merging 2000, 2004 and 2010 Agcensus datasets, in order to generate a single dataset determining wheat producing areas, we assumed that the regional crop growing areas were fixed across the time period (2000-2013) used in this analysis. However, due to a host of socioeconomic factors, including those related to the Common Agricultural Policy, we accept that this assumption was an over simplification of the dynamics of UK croplands. Therefore, the use of additional temporal datasets on wheat crop producing areas would be expected to reduce the uncertainty, due to land cover misclassification, in the analysis of the MODIS LAI and model estimates.

Given the relatively small UK field sizes, the 1 km MODIS LAI, used in the knowledge-based filtering, would have consisted of a mixture of reflectance responses from different vegetation types and land cover classes. And so, covering the dominant crop growing areas delineated from the multi-temporal census data, we would recommend the use of data from higher resolution EO sensors (e.g. SPOT-6/7 or Landsat-8 with a spatial resolution of 6 m and 30 m, respectively). Image-based classification approaches could then be applied to the higher resolution EO scenes, which could also be combined with ancillary map data, to resolve the crop coverage on a per-field basis (e.g. Hill *et al.*, 2011; Löw *et al.*, 2013).

In addition to the intra-pixel heterogeneity of the 1 km MODIS data, the global LAI product was designed for all vegetation types (i.e. not specifically for agricultural vegetation) and the LAI for crops is generally under-estimated (Fang *et al.*, 2011; Duveiller *et al.*, 2013). Therefore, using the MODIS LAI to calibrate the DR_{pre} parameter would have introduced uncertainty into the model. Nonetheless, given the relatively short revisit time (i.e. every 8 days) and large area coverage, we consider the use of the MODIS product to be effective at tracking crop phenology. An alternative approach, such as that detailed in Huang *et al.* (2015; 2016), would be to adjust the MODIS LAI time-series with LAI estimates derived from high resolution EO sensors (e.g. 30 m resolution Landsat-TM 5). This multi-sensor integration could potentially generate an updated LAI time-series that simultaneously resolves the spatial heterogeneity of UK cropland landscapes whilst capturing the key phenological stages. However, due to a lack of standardised LAI products, deriving LAI from high resolution EO sensor data requires extensive field-scale observations (Huang *et al.*, 2015), which is seldom available – particularly for a regional-scale application.

It is anticipated that forthcoming EO sensors, most notably the launch of the Sentinel-2 satellite pair (Torres *et al.*, 2012), will address the spatial-temporal resolution trade-offs of EO data by increasing the observational frequencies whilst maintaining high spatial resolutions. The optical Sentinel-2 sensors are also expected to include LAI maps (see Martimor *et al.*, 2007) and therefore would be readily available for use in the model-data framework described in this research.

4.5. Conclusion

Through the integration of crop model outputs with MODIS LAI and agricultural census data, this research presents a framework for the regional estimation of UK winter wheat yields. We demonstrate that there is a relationship (mean $R^2 = 0.29$) between regionally averaged mean maximum MODIS LAI and official yield statistics in the UK. Although negatively biased for all regions (mean NMB = -12%), the accuracy of the regionally aggregated model yield estimates was reasonable (mean RMSE = 0.71 t ha^{-1}) when evaluated using the yield data. We investigated the use of the MODIS LAI time-series for adjusting the crop model parameter that determines the developmental rate during the vegetative stages. From using the MODIS LAI as a constraint, negative biases in the model yield estimates were reduced for the majority of the regions (mean NMB = -5%), however the estimation error was slightly increased (mean RMSE = 0.73 t ha^{-1}). This error increase is likely due to the scale mismatch between UK field sizes and the 1 km MODIS LAI. Consequently, we consider the model-data fusion approaches detailed here to be a benchmark when evaluating the inclusion of finer-scale EO-derived data that would be expected to capture UK agriculture more accurately.

4.6. Summary

A model-data fusion framework for generating UK winter wheat crop yield estimates at regional-scales has been presented. Multi-annual crop model yield estimates, generated using the ACM photosynthesis calibration detailed in Chapter 3, were spatially aggregated from 1 km to UK regions and evaluated using the yield data. These aggregated crop model yield estimates were negatively biased with a RMSE of 0.71 t ha^{-1}. The use of 1 km resolution MODIS LAI time-series is further evaluated for constraining the model simulation of canopy development. Constraining the model with MODIS LAI reduced the negative bias in regional yield estimates by 50%, however the RMSE increased to 0.73 t ha^{-1}. Due to sub-pixel heterogeneity, it is likely that the 1 km MODIS LAI is insufficient at resolving crops fields that are characteristic of UK agriculture. To this end, the next chapter (Chapter 5), aims to quantify the errors associated with the spatial and temporal resolution of EO sensors for resolving crop growth at UK field-scales.

CHAPTER 5

Earth observation spatial and temporal resolution requirements for crop growth monitoring at UK field-scales

5.1. Introduction

Data derived from satellite Earth observation (EO) sensors can be a valuable tool for providing timely and synoptic information on crops over large geographical extents (Dente *et al.*, 2008; Rembold *et al.*, 2015). Consequently, EO sensors have been exploited to support crop monitoring since the launch of Landsat 1 in 1972 (Bauer and Cipra, 1973). Continual developments in EO sensors, and associated technologies, has led to increasing volumes of EO data available at higher spatial and temporal resolutions, which in turn has given rise to multiple cropland usages of EO data. Atzberger (2013) discusses EO cropland applications, including yield forecasting, phenological monitoring and the mapping of crop types and distributions. These applications span a range of spatial and temporal scales, therefore the careful consideration of the spatial and temporal resolutions of EO sensors is essential when meeting the demands of a particular application (Xie *et al.*, 2008; Duveiller and Defourny, 2010; Mulla, 2013; Whitcraft *et al.*, 2015).

Spatial resolution determines the capability of an EO sensor for accurately recording the spatial detail of crops at field-scales, such as that which could support precision agricultural management applications (Mulla, 2013). Specifically, spatial resolution is defined throughout this thesis as the ground sampling distance (GSD) that is within the sensor's instantaneous field of view (IFOV, Lillesand *et al.*, 2008). Furthermore, spatial resolution determines the area covered by the smallest pixel; therefore spatial resolution is inversely proportional to pixel size, i.e. as spatial resolution improves the coverage of the smallest pixel decreases (Mulla, 2013).

The range of typical EO sensor spatial resolutions can broadly be defined as high (< 10 m; e.g. SPOT-6/7, Pleiades-1) to medium (10 - 250 m; e.g. Landsat-7/8) and low (250–5000 m; e.g. MODIS, AVHRR). Globally, cropland landscapes present a mosaic of fields that vary in size, shape and fragmentation. And so, for a given cropland application, the spatial resolution requirements are dependent on the geographical location (Duveiller *et al.*, 2008; Duveiller and Defourny, 2010). For instance, using 250 m resolution MODIS data, Wardlow *et al.* (2007) discriminated individual fields that were at least 32.4 ha in size in an area located in the United States' Central Great Plains region. Additionally, Fritz *et al.* (2008) demonstrated that the MODIS data was suitable for mapping field sizes of around 75 ha in a dominant crop producing region in Russia. However, in some areas, the pixels derived from coarse-scale (i.e. relative to the field sizes) MODIS data can comprise of a mixture of land cover types, which complicates the accurate retrieval of biophysical variables from EO data (Delecolle *et al.*, 1992; de Wit and van Diepen, 2007). In particular, the use of medium to low spatial resolution sensors is typically insufficient for retrieving biophysical variables at field sizes less than 25 ha due to sub-pixel heterogeneity (Doraiswamy *et al.*, 2004). These smaller fields, such as those across the European Union (EU-28) where the average size of an agricultural holding is only 14.4 ha (Eurostat, 2013), require EO data from medium to high spatial resolution sensors.

Due to technical constraints, an increase in the spatial resolution of an EO sensor is typically at the expense of a reduction in temporal resolution. The temporal resolution of an EO sensor is further complicated by the degree of overlap between image swaths from adjacent orbits, which varies with latitude. However, for simplicity, the research presented in this chapter defines temporal resolution as the absolute temporal resolution – equal to the time taken by the satellite EO sensor platform to complete one orbital cycle (Maini and Agrawal, 2014). High temporal resolution EO sensors, such as MODIS near-daily surface reflectance products, are essential for monitoring crop phenology in order to capture the key developmental stages (Launay and Guerif, 2005; Duveiller *et al.*, 2008). In addition to the temporal resolution, the capabilities of optical EO sensors for acquiring a sufficiently clear view of a croplands is often severely limited by cloud cover (Moran *et al.*, 1997; Whitcraft *et al.*, 2015). Although the presence of clouds within an EO scene can be detected and masked out (see Zhu and Woodcock, 2012), this results in irregular gaps in observations throughout the crop growing season.

Generally, the degree of cloud cover varies temporally, for instance clouds have significant diurnal cycles with maximum coverage in the afternoon (Cairns, 1995) and seasonal cycles with a maximum during the summer (Wylie *et al.*, 2005). Clouds also exhibit spatial trends, with the mean annual coverage being higher around the equator and temperate latitudes when compared to that of the tropics (Rossow and Schiffer, 1999). And so, when considering the optimum EO acquisition strategy for a multi-temporal crop monitoring activity it is necessary to determine the extents to which cloud cover varies over a particular landscape throughout a growing season. Whitcraft *et al.* (2015) investigated the frequency of which an optical EO sensors can probabilistically obtain a cloud-free view of global croplands. The analysis by Whitcraft *et al.* (2015) included determining the likelihood of cloud cover based on daily 1 km MODIS reflectance quality assurance (QA) cloud flags over a 10-year period.

It is anticipated that forthcoming optical EO sensors will address the spatial-temporal resolution trade-offs of EO data. Specifically, the European Space Agency (ESA) Sentinel-2 sensor will operate in a dual-platform configuration (i.e. Sentinel-2A & 2B; Torres *et al.*, 2012), which will essentially increase the temporal resolution whilst maintaining high spatial resolutions of up to 10 m in four spectral bands (Verrelst *et al.*, 2015). In spite of this, high temporal resolution and long-term archives generated by coarser sensors, such as MODIS and MERIS, would still be of value when performing a multi-annual analysis of crops over specific areas (Duveiller *et al.*, 2012; Brown *et al.*, 2013; Löw *et al.*, 2013; Mulla, 2013). These EO datasets could also be used, for instance, for initialising and constraining (via a data assimilation framework) a regional-scale crop model application for carbon (C) fluxes and yield estimates, such as that evaluated in Chapters 2 and 4. However, the effectiveness of such assimilation schemes is largely dependent on accurately specifying the uncertainty of both the model and EO data (Williams *et al.*, 2005; Zhao *et al.*, 2013).

This study characterises errors associated with the spatial and temporal resolution of optical EO sensors for targeting field-scale cereal crop growth monitoring applications across UK landscapes. This analysis first involved quantifying the spatial resolution errors associated with using medium to low resolution EO sensors for resolving UK fields. This error was determined by spatially aggregating pixels within fine spatial resolution EO imagery in order to produce a continuum of images with progressively coarser pixel sizes. The spectral detail of the aggregated images was then sampled on a per-field basis and compared to that of the original fine-scale image. Second, by resampling the output from a crop-specific C cycle model (DALECc, see Chapter 3), the impacts of EO temporal resolution when monitoring winter wheat crop growth were simulated. The likely spatial and temporal impacts of cloud cover on the optical EO time-series was further investigated. The key research questions addressed in this research were:

1) What is the minimum EO sensor spatial resolution required to monitor crops at field-scales that are characteristic of UK agriculture?

2) How does temporal resolution and likely cloud cover influence the effectiveness of optical EO sensors for tracking winter wheat crop canopy development over cropland landscapes?

3) What are the expected benefits of ESA's Sentinel-2 satellite pair (i.e. Sentinel-2A and B) for multi-temporal crop monitoring at UK field-scales?

The novelty of this research is an analysis of both the spatial and temporal resolution of EO sensors that are required for monitoring field-scale crop growth – specifically across UK landscapes. Furthermore, the use of outputs from the calibrated DALECc model provides a synthetic time-series of realistic observations that could be further sampled to mimic EO sensor temporal resolution and cloud cover.

5.2. Methods and data

In this section, a brief overview of the areas selected for analysis is first provided. Second, the pre-processing applied to the optical EO imagery is detailed, including the retrieval of LAI estimates, pixel aggregation and the field-scale sampling of pixel values using a field mask derived for each of the areas. Third, the development of a synthetic LAI time-series, designed to mimic the typical EO sensors temporal resolution, is described along with estimates of daily cloud cover over the cropland areas.

5.2.1. Selection of Areas of Interest (AOI)

A total of 24 Areas of Interest (AOIs) – each covering a 6 x 6 km area of the UK – were used in this analysis (Figure 5.1). Four AOIs were selected within six key wheat producing UK administrative regions: East Midlands, West Midlands, Yorkshire & the Humber, North East, South East and Eastern England. The selection of the AOIs was based on a two-fold criteria: first, areas were identified where wheat crop production was greater than 50% of the total arable cropland area. These areas were based on a 2010 Agcensus dataset (as used in Chapter 4), which was developed by the University of Edinburgh Data Library and consisted of DEFRA Agricultural Census results aggregated to 2 km grid squares. Second, in order to minimise uncertainties due to atmospheric affects, the optical EO data (SPOT-6) of the AOIs had to be 100% cloud-free at the time of acquisition.

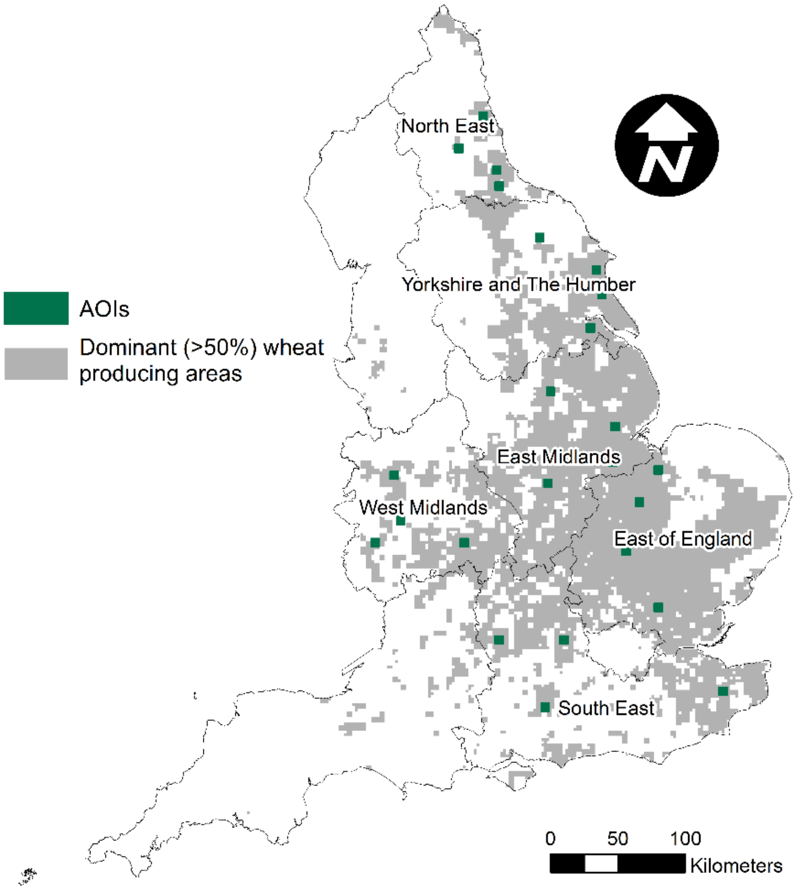

Figure 5.1: Map showing the locations of 24 Areas of Interest (AOIs) each covering a 6 x 6 km area of a dominant (> 50%) UK wheat producing region.

5.2.2. SPOT-6 image processing

Image pre-processing

The SPOT-6 (Satellite Pour l'Observation de la Terre) Ortho product imagery was sourced from Airbus Defence and Space under an ESA Category-1 agreement. This data, which was subset to the spatial extents of each AOI, comprised of georeferenced (OSGB 1936/British National Grid) multi-spectral SPOT-6 optical imagery at a spatial resolution of 5 m. Only one image acquisition date was selected per AOI. The SPOT-6 image acquisition dates used ranged from the 3rd May to 18th July 2013, which coincide with the key vegetative and reproductive phases of UK wheat crops (Sylvester-Bradley *et al.*, 2008).

Pre-processing applied to the SPOT-6 data included conversion of the raw radiometric digital numbers at each pixel to top-of-atmosphere radiance for each band using the absolute radiometric calibration coefficients available in the imagery metadata. This conversion was performed using Equation 2.1 shown in Chapter 2. Topographic normalisation was then applied to the SPOT-6 subsets, which involved reducing differences in the scene illumination that were due to the slope and aspect of terrain relative to the solar elevation and azimuth. This procedure was carried out in ERDAS Imagine (version: 2013) using a Lambertian Reflection model (Smith *et al.*, 1980; Colby, 1991). Inputs to this model included solar elevation and azimuth, also available from the image metadata, and Ordnance Survey (OS) Terrain 5 m digital elevation data, which was used to estimate slope and aspect. Since only one imagery scene per AOI is used in this analysis, no further pre-processing was applied to normalise atmospheric conditions in the SPOT-6 subsets – as would otherwise be required for a multi-date comparison (Kalubarme *et al.*, 2003). It is also assumed that atmospheric affects are uniform across each of the 6 x 6 km AOIs.

LAI retrieval

LAI is a good indicator of crop status and is among the most common vegetation canopy variables that are retrieved from EO data (Casa *et al.*, 2012). Therefore, the SPOT-6 subsets were used to generate LAI maps for each of the AOIs (for example see East of England, AOI 1; Figure 5.2). This LAI was retrieved empirically by first calculating the Weighted Difference Vegetation Index (WDVI, Clevers, 1988; 1991). The WDVI is an orthogonal index used to reduce the effect of soil reflectance, which influences the relationship between the scene reflectance and LAI. For each SPOT scene, the WDVI was calculated using:

$$WDVI = R_{NIR} - \gamma . R_{VIS} \qquad \text{Equation 5.1}$$

where R_{NIR} and R_{VIS} correspond to the reflectance values in the near-infrared and visible red sensor wavebands, respectively. The ratio of reflectance in the near-infrared and visible red wavebands (R_{NIR}: R_{VIS}) for bare soil (i.e. before crop emergence) is shown as γ. Results in Revill *et al.* (2013, presented in Chapter 2 of this thesis) demonstrated a range in γ values from 0.75 to 1.98 across multiple cereal crop sites. Therefore, in this study, the mean γ value (1.37) is used in Equation 5.1. The LAI was then retrieved based on an assumed linear relationship with the WDVI:

$$LAI = m.WDVI + c \qquad \text{Equation 5.2}$$

where m and c are the slope and intercept coefficients of the linear fit between the WDVI and LAI. The coefficient values used (m = 0.23, c = -1.57) were also previously derived in Chapter 2 based on the relationship between WDVI to LAI fields measurements.

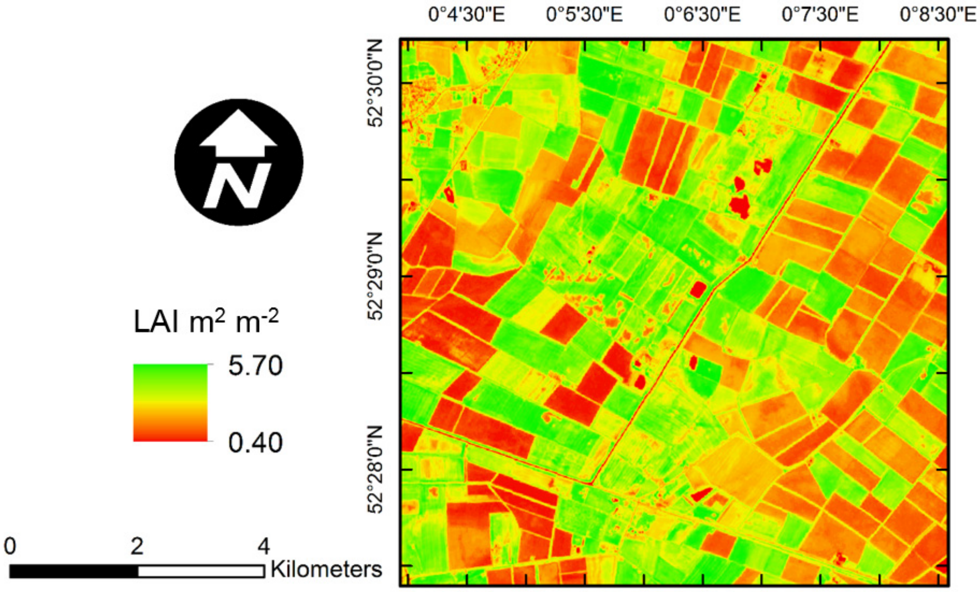

Figure 5.2: Example Leaf area index (LAI) map generated for AOI 1 in the East of England region.

5.2.3. Generating field masks

A binary field mask was generated to identify target areas (i.e. agricultural fields, see Table 5.1) within each AOI for subsequent overlay analysis with the SPOT-6 LAI estimates. This field mask was generated using OS MasterMap (OSMM) Topography Layer vector data. The OSMM data, which covers the UK at fine spatial scales (1:1 250 to 1:10 000), was extracted and clipped to the extents of each AOI. Based on the OSMM attribute information, the polygons were then filtered using ESRI's ArcMap (version: 10.1) GIS software spatial querying tools. This filtering specifically entailed selecting polygons that had a 'Theme' classification of 'Land' and a 'Legend' classification as 'Natural surface'. This selection of target areas was further refined by removing land that was less than 1 ha. A buffer zone of -5 m was then applied to the remaining land polygons in order to minimise the influence of hedgerows and ensure a representative within-field spectral sample when combined with the LAI estimates.

Table 5.1: Number and average size (including 5/95-percentile range) of all fields delineated by the crop masks generated for each of the Areas of Interest (AOI).

Region	AOI	Number of fields	Average field size and 5/95-percentile range (hectares)
North East	1	432	3.58 (1.12/8.23)
	2	453	5.8 (1.18/18.55)
	3	369	7.07 (1.11/25.07)
	4	316	5.96 (1.19/14.95)
Yorkshire and The Humber	1	295	10.43 (1.34/30.67)
	2	516	5.05 (1.12/14.90)
	3	285	11.26 (1.36/31.15)
	4	302	10.23 (1.17/34.96)
West Midlands	1	443	5.76 (1.20/16.63)
	2	625	3.90 (1.11/9.45)
	3	591	4.02 (1.12/10.88)
	4	545	4.76 (1.19/11.10)
East Midlands	1	425	6.80 (1.19/22.17)
	2	480	5.65 (1.26/14.68)
	3	327	9.22 (1.25/24.87)
	4	283	10.24 (1.13/34.93)
Eastern England	1	285	10.88 (1.40/35.75)
	2	157	19.64 (1.08/102.29)
	3	254	12.49 (1.22/41.03)
	4	276	10.62 (1.17/34.67)
South East	1	275	6.87 (1.13/26.16)
	2	333	7.14 (1.13/25.14)
	3	298	4.67 (1.09/14.37)
	4	307	8.41 (1.16/31.08)
Median	**-**	**322**	**6.97 (1.17/24.97)**
Average	**-**	**370**	**7.93 (1.18/26.40)**

5.2.4. LAI data aggregation and sampling

Pixel aggregation

In order to determine the uncertainty from using medium to coarse-scale EO data, for each AOI, pixels from the fine scale SPOT-6 LAI image (referred to hereafter as the base image) were spatially aggregated (Figure 5.3). This spatial aggregation, achieved through the averaging of neighbouring pixels, was increasingly applied from 10 to 1000 m in increments of 5 m. And so, including the 5 m base image, this process resulted in a continuum of 200 EO-derived LAI maps of increasingly coarser pixels, which were used to emulate data acquired from EO sensors of differing spatial resolution.

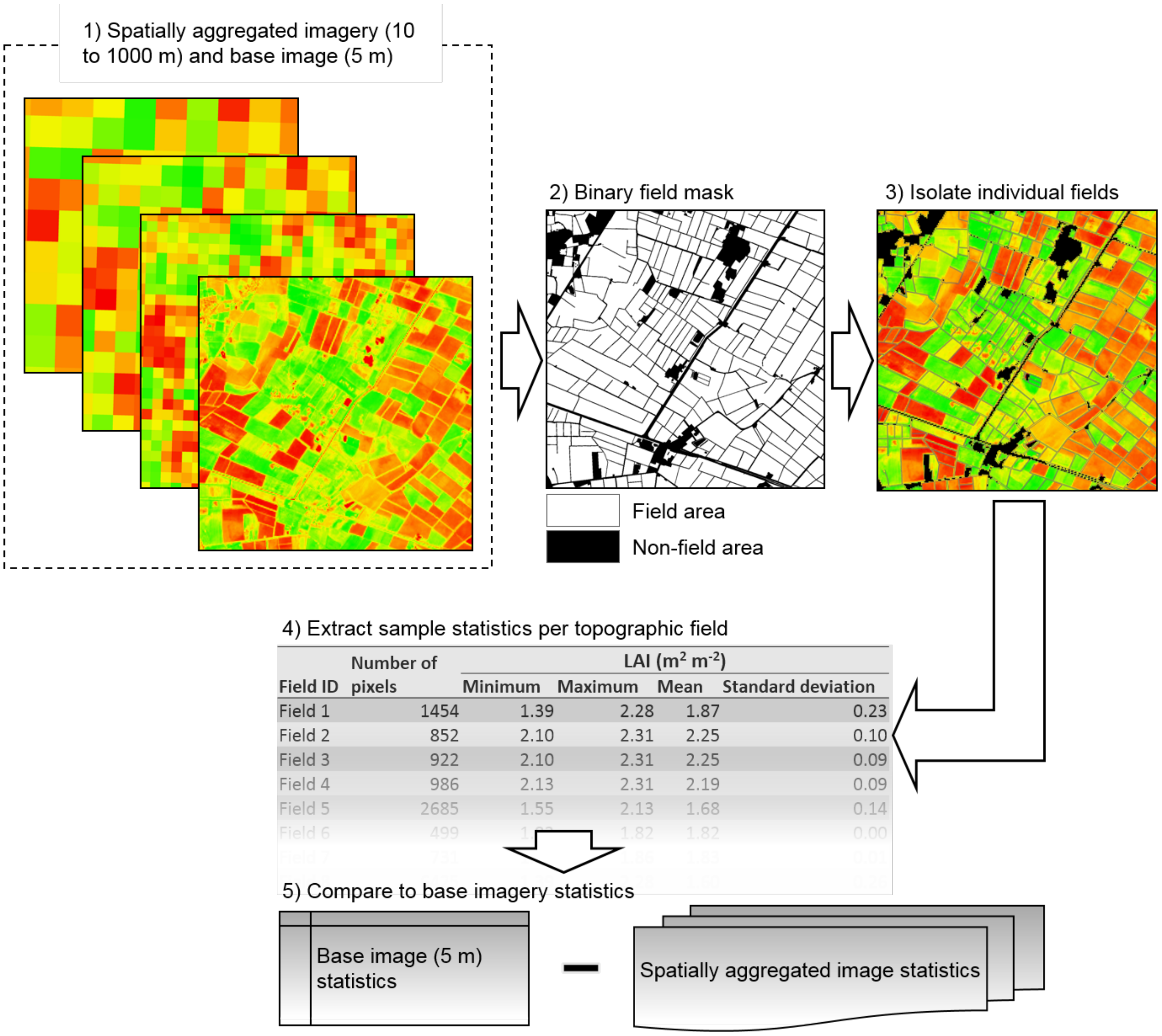

Field ID	Number of pixels	LAI (m^2 m^{-2})			
		Minimum	Maximum	Mean	Standard deviation
Field 1	1454	1.39	2.28	1.87	0.23
Field 2	852	2.10	2.31	2.25	0.10
Field 3	922	2.10	2.31	2.25	0.09
Field 4	986	2.13	2.31	2.19	0.09
Field 5	2685	1.55	2.13	1.68	0.14
Field 6	499	[illegible]	1.82	1.82	0.00
Field 7	731	[illegible]	1.86	1.83	0.01

Figure 5.3: Schematic outlining the processing steps used to quantify the uncertainty of within-field LAI estimates when using images of increasing pixel sizes. This processing framework included: 1) spatially aggregating a fine-scale (5 m) base image to produce a continuum of images with increasingly coarser pixel sizes (from 10 to 1000 m). 2) A field mask, generated from Ordnance Survey MasterMap data, is used to delineate fields. 3) All images were combined with the field mask to isolate target fields within the AOIs. 4) Statistics were generated from sampling LAI pixels within each of the target fields. 5) Statistics generated from each of the aggregated images are compared to the base image to calculate differences in within-field LAI estimates from using larger pixels.

Per-field sampling and analysis

Through GIS overlay analysis of the field mask with the continuum of LAI maps, pixel statistics were produced for each of the AOIs (Figure 5.3). The statistics generated for each of the target fields in the crop masks, included the pixel population, standard deviation, minimum and maximum and mean LAI values. This set of field statistics was tabulated for all LAI maps, including that of the base image. Furthermore, when sampling individual fields, the applied GIS analysis selected pixels that either wholly or partially covered a given field (i.e. as opposed to sampling pixels within the field only, see Figure 5.4). And so, this sampling strategy ensured that a given field was covered by a minimum of one pixel regardless of the pixel size relative to that of the field.

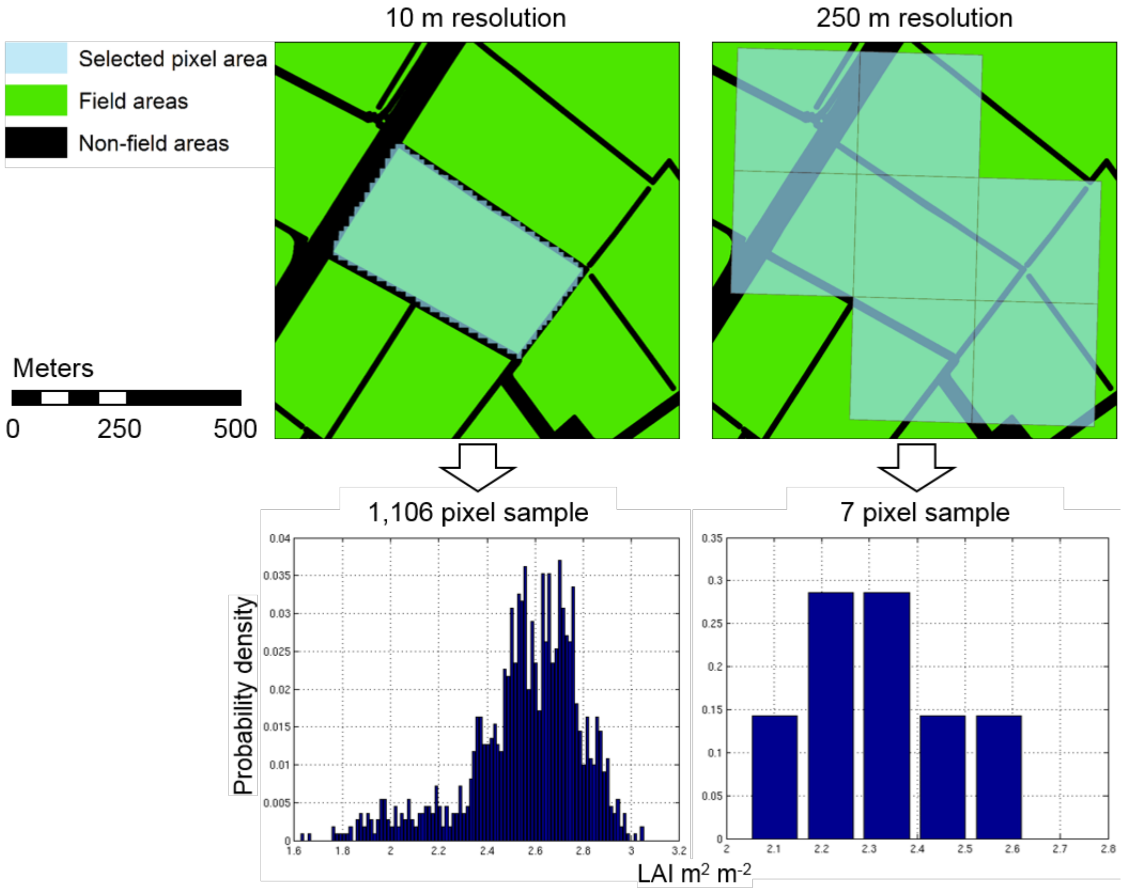

Figure 5.4: Example images from within the East of England region demonstrating the sampling strategy used to select pixel (pale blue boxes) overlaying a given field. Shown for 10 m (left) and 250 m (right) pixel sizes. Pixel sample values are also shown as probability distributions.

The statistic from sampling the aggregated images were systematically compared to those of the base image (i.e. base image minus aggregated image), thus providing an evaluation of the differences in mean field values due to increasing pixel sizes. The mean absolute difference between the base LAI map and the aggregated image maps is used to calculate a percentage error on a per-field basis:

$$LAI\ error\ (\%) = \left|\frac{(base\ image - aggregated\ image)}{base\ image}\right| \times 100 \qquad \text{Equation 5.3}$$

Using the calculated mean LAI error, recommendations are made regarding pixel size requirements for the operational monitoring of UK field crops. High spatial resolution sensors (i.e. smaller pixel sizes) would increase the likelihood of resolving the field-scale detail. However, due to the spatial-temporal resolution trade-offs of EO sensors, inferring a recommended maximum pixel size (i.e. minimum resolution) would be more useful. This mean maximum pixel size, calculated for each region, was selected as the pixel size at which the rate of increase in LAI error with increasing pixel size becomes less than or equal to zero. And so, beyond this quantified pixel size, it was assumed that values from larger pixels were no larger representative of the fields.

5.2.5. Simulating EO temporal resolution and cloud cover

Generating synthetic LAI time-series

A synthetic experiment was carried out to determine the influence of EO sensor temporal resolution when monitoring winter wheat canopy development – expressed through changes in LAI. Daily LAI estimates were first generated using the process-based Data Assimilation Linked Ecosystem Carbon crop (DALECc) model. Using meteorological drivers and daily photosynthesis estimated from the calibrated Aggregated Canopy Model (ACM, see Chapter 3 for further details), DALECc simulates C allocated according to a crop-specific C partitioning scheme. And so, since the model has been parameterised and validated based on observations at multiple winter wheat sites, DALECc can produce realistic estimates of daily LAI. This LAI time-series (referred to henceforth as '$\mathrm{LAI}_{\mathrm{truth}}$') was simulated between the average sowing and harvest dates of UK winter wheat – 31st September (sowing date) and 27th July (harvest date) – according to a Crop Calendar Dataset developed by Sacks *et al.* (2010).

The $\mathrm{LAI}_{\mathrm{truth}}$ was generated at 1 km points for each of the 6 x 6 km AOIs (i.e. 36 LAI times-series per AOI) by driving DALECc using the 1 km gridded Climate, Hydrology and Ecology research Support System (CHESS) data developed by the Centre for Ecology and Hydrology (CEH, 2014). The $\mathrm{LAI}_{\mathrm{truth}}$ dataset was then resampled by removing LAI values to mimic the typical temporal resolution of current optical EO sensors. Three additional LAI time-series were generated, each with a different LAI temporal frequency: every 10, 16 and 26 days (referred to as $\mathrm{LAI}_{\mathrm{truth-10}}$ $\mathrm{LAI}_{\mathrm{truth-16}}$ and $\mathrm{LAI}_{\mathrm{truth-26}}$), which correspond to the temporal resolutions of the Sentinel-2, Landsat-7/8 and SPOT-6/7 EO sensors, respectively.

Estimating likelihood of cloud cover

To determine the likely impact of cloud cover on an optical EO sensors time-series used to monitor crop development, the daily probability of a clear-sky view (i.e. no cloud cover) was estimated for within each of the AOIs. Daily cloud observations covering the spatial and temporal extents of this study were non-existent, therefore the probability of cloud cover was estimated from a MODIS EO data product using a similar approach to that of

Whitcraft *et al.* (2015). Specifically, this method included analysing 11-years (2001-2011) of daily 250 m resolution MODIS Terra Surface Reflectance (MOD09GQ) quality assurance (QA) data (Figure 5.5). For each year, the QA layer information on cloud state (i.e. ‘cloudy’ or ‘clear’ flag) data was used to determine all cloudy 250 m pixels for a given day of year. From repeating this procedure over the multi-annual period, 11 cloud cover observations existed for each day of year. Then, for each of these days, the probability of obtaining a clear-sky observation (referred to hereafter as ‘P_{clear}’) was calculated by dividing the number of clear-sky observations by the total number of observations:

$$P_{\text{clear(day)}} = \frac{\text{number of clear sky observations}}{\text{total number of observations}} \qquad \text{Equation 5.4}$$

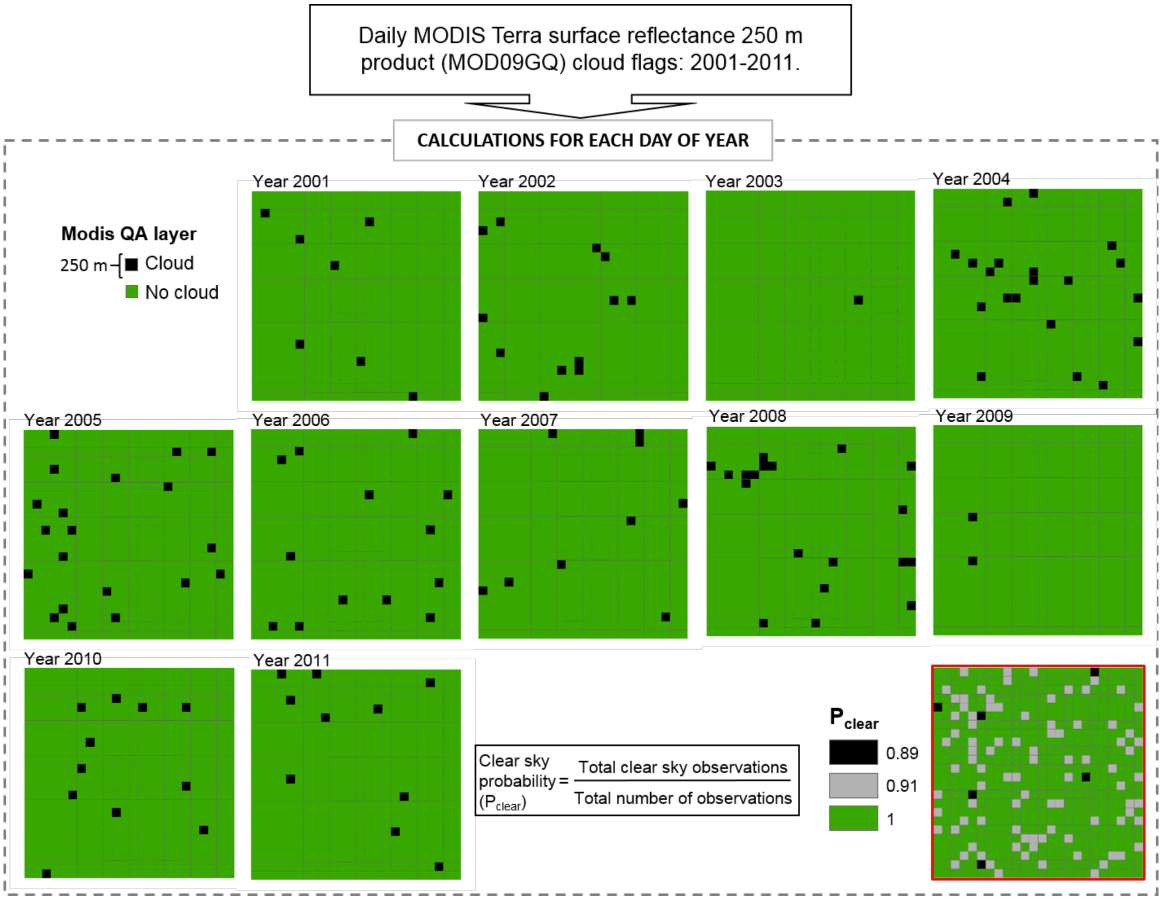

Figure 5.5: Schematic detailing the processing chain used to calculate the probability of cloud-free (P_{clear}) observation: example shown for the East of England region (AOI 1). The 250 m MODIS Terra Surface Reflectance (MOD09GQ) quality assurance (QA) data is used to determine all clear (and cloudy) days between 2001 and 2011. For each day of year, P_{clear} is calculated by dividing the number of clear observations by the total number of observations (adapted from: Whitcraft *et al.*, 2015).

The daily P_{clear} values were combined with the $LAI_{truth-10}$, $LAI_{truth-16}$ and $LAI_{truth-26}$ datasets to mimic reductions in EO acquisitions due to cloud cover obscurity. This processing step involved removing the LAI values on days that had a corresponding P_{clear} value of less than 1. Therefore, this filtering assumed a ‘worst case scenario’ where only

LAI observations were retained on days that were certain to be cloud-free based on daily cloud observations over an 11-year period. Furthermore, due to the difference in grid cell sizes (i.e. 250 m and 1 km), combining the P_{clear} values with the LAI time-series essentially disaggregated the 1 km points within the AOIs, and thus increased the number of LAI sample points within each AOI – from 36 to 576 points.

All the $LAI_{truth-10}$, $LAI_{truth-16}$ and $LAI_{truth-26}$ synthetic datasets, both with and without the P_{clear} filtering were gap-filled (via linear interpolation) so that the values could be directly compared to the original LAI_{truth} datasets (Figure 5.6). Metrics were generated, such as the normalised root-mean-square-error (RMSE), in order to quantify the impacts of EO temporal resolution, combined with likely cloud cover, for monitoring winter wheat growth over UK landscapes.

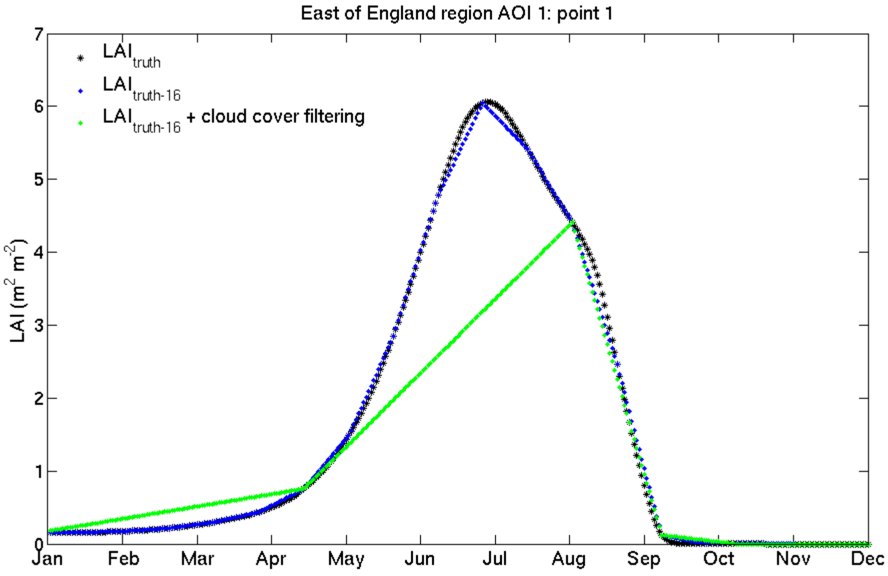

Figure 5.6: Example plot from the East of England region (AOI 1) comparing DALECc model. daily LAI estimates (black asterisks, LAI_{truth}) to a 16-day linearly interpolated sample (blue dots, $LAI_{truth-16}$) along with the 16-day interpolation of LAI observations filtered for likely cloud cover (green dots, $LAI_{truth-16}$ + cloud cover filtering).

5.3. Results

The results from estimating the errors associated with reductions in EO sensor spatial resolution when resolving UK fields is first presented. Second, the quantified errors due to EO temporal resolution and cloud cover obscurity are provided.

5.3.1. LAI estimation with pixel size

Generally, from comparing the base image statistics to each of the aggregated images, the error and uncertainty in LAI estimates increased with increasing pixel size for all regions

(Figure 5.7). The recommended maximum pixel size had a mean value of 165 m – ranging from 100 m (West Midlands) to 225 m (East Midlands). Based on the 5/95-percentile range, these recommended maximum pixel sizes corresponded to a mean LAI uncertainty of 3.27%, which ranged from 0.85% (East of England) to 6.63% (East Midlands).

The increase in mean LAI error between the recommended maximum pixel size and the largest pixel size (1000 m) were relatively small: ranging from only 0.24% (East Midlands) to 5.01% (West Midlands). However, the uncertainty progressively increased from the recommended maximum pixel size. In particular, from sampling the 1000 m sized pixels the average 5/95-percentile range was 17.86%, with this value ranging from 6.78% (East of England) to 29.44% (East Midlands).

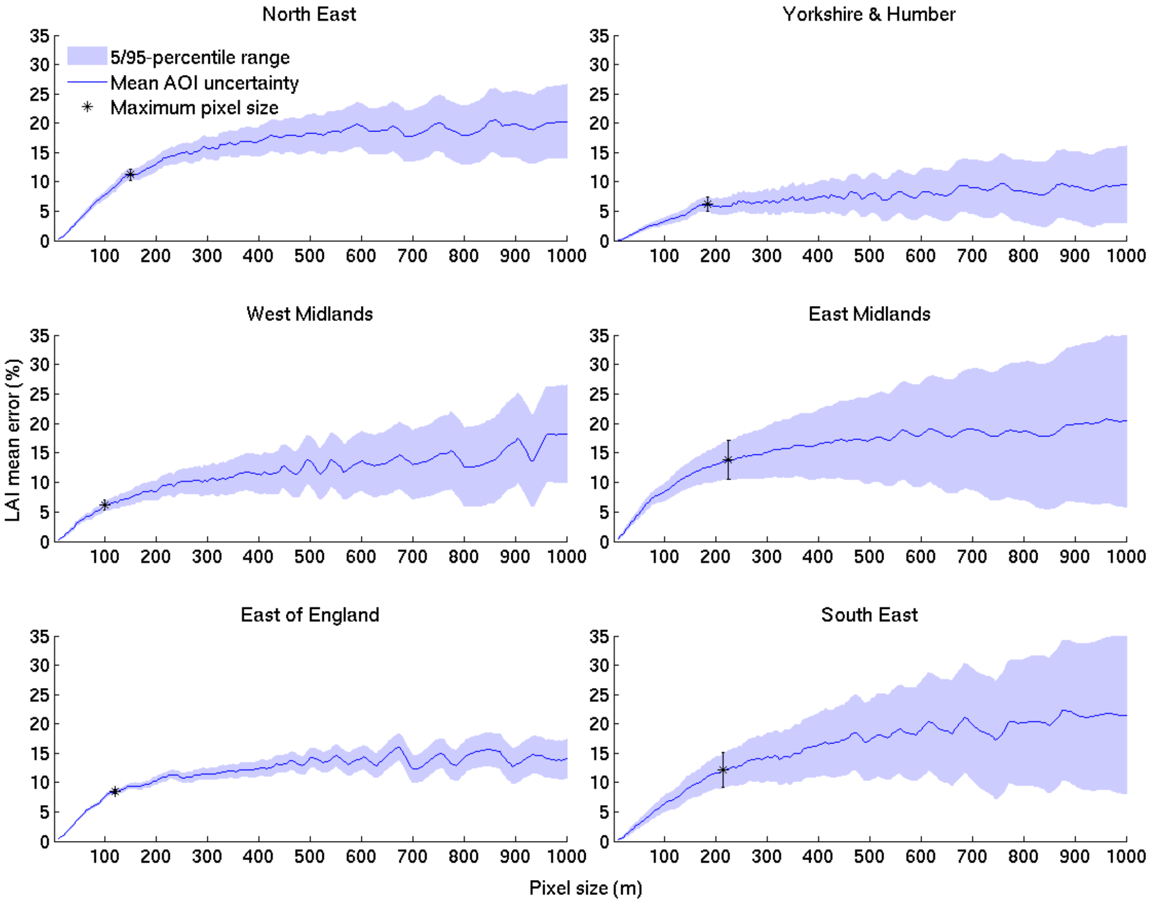

Figure 5.7: Plots of the mean error in field-scale LAI estimates (blue line) with increasing pixel size. Mean uncertainty is estimated by comparing field-scale LAI estimates between the base image (5 m pixel size) and spatially aggregated images that are then averaged across four areas of interest (AOI). The 5/95th-percentile range (blue shading) is estimated from the per-field values from AOIs. The recommended maximum pixel size (black asterisk) marks the point where the rate of increase in uncertainty with grid size is less than or equal to 0.

5.3.2. Evaluating EO temporal resolution and cloud cover

Each of the linearly interpolated $LAI_{truth-10}$, $LAI_{truth-16}$ and $LAI_{truth-26}$ time-series were compared to the original LAI_{truth} datasets and used to calculate a regional mean normalised

RMSE (Table 5.2). Without the cloud cover filtering the mean normalised RMSE values were generally consistent across all regions with an average of 0.15%, 0.81% and 5.16% for the $LAI_{truth-10}$, $LAI_{truth-16}$ and $LAI_{truth-26}$ time-series, respectively. Applying the cloud cover filtering significantly increased errors when comparing the LAI time-series to the LAI_{truth} dataset with the mean normalised RMSE increasing to 28%, 48% and 63% for the $LAI_{truth-10}$, $LAI_{truth-16}$ and $LAI_{truth-26}$, respectively. Furthermore, with the cloud cover filtering, all three time-series had greater regional variability; where the mean error was generally larger in the North East and Yorkshire & Humber when compared to the West Midlands and South East regions.

Table 5.2: Comparison of the regional mean normalised root-mean-square (RMSE) from comparing daily LAI values to three LAI time-series that differ in the frequency of observations: every 10 ($LAI_{truth-10}$), 16 ($LAI_{truth-16}$) and 26-days ($LAI_{truth-26}$). Comparisons are also made when removing potentially cloudy days from the three time-series.

	Mean normalised RMSE					
Region	**$LAI_{truth-10}$**	**$LAI_{truth-16}$**	**$LAI_{truth-26}$**	**$LAI_{truth-10\ +\ cloud}$**	**$LAI_{truth-16\ +\ cloud}$**	**$LAI_{truth-26\ +\ cloud}$**
North East	0.144	0.833	5.032	66.865	58.749	96.590
Yorkshire & the Humber	0.137	0.787	5.923	28.490	56.594	93.044
West Midlands	0.142	0.759	5.668	3.591	27.637	33.322
East Midlands	0.150	0.809	5.153	27.130	68.709	73.887
Eastern England	0.155	0.859	3.726	16.184	25.413	27.219
South East	0.148	0.789	5.474	27.463	50.596	51.513
Average	**0.146**	**0.806**	**5.163**	**28.287**	**47.950**	**62.596**

5.4. Discussion

The estimated errors due to EO sensor spatial and temporal resolutions are first discussed in the context of operational UK field-scale crop monitoring. Second, the research findings are used to discuss the likely benefits of the Sentinel-2 satellite pair for UK crop monitoring applications. Third, the caveats and limitations of this analysis are highlighted.

5.4.1. EO errors and uncertainty

Spatial resolution errors

Fine scale EO imagery was spatially aggregated to generate a continuum of progressively larger pixels in order to approximate images acquired from medium to coarse-scale EO sensors. By sampling the aggregated image pixels within target fields, it was possible to tracks errors associated with using lower spatial resolution EO sensors to retrieve values from UK fields. The calculated mean maximum pixel size (i.e. the coarsest spatial resolution required to adequately resolve fields) ranged from 100 to 225 m. And so, it can be inferred that UK field sizes are generable indiscernible using EO sensors with a spatial resolution of less than 225 m. This range in coarsest pixel size is also comparable to that approximated by Duveiller and Defourny (2010) where these sizes ranged from 120 to 300 m for regions located in China, Belgium, France and the Netherlands.

Temporal resolution and cloud cover

A synthetic LAI time-series was generated by removing daily LAI estimates, generated using the DALECc model, in order to mimic the typical temporal resolutions of EO sensors. A comparison of the sampled and linearly interpolated LAI to the original daily time-series indicated that an observation frequency of only 26 days – corresponding to a relatively low temporal resolution EO sensor – can capture crop canopy development with an error of only 5.16%.

In an operation context, it would be expected that the frequency of optical EO acquisitions would be reduced due to cloud cover obscurity. Therefore, days that were likely to be cloudy during the crop growing season were removed from the resampled LAI datasets. By accounting for the likely cloud cover, errors in the interpolated LAI time-series can be as high as 63% for the 26-day LAI dataset. Furthermore, even when using a higher 10-day temporal resolution EO sensor the errors would be expected to increase from 0.15% to 28% due to cloud cover. This result indicates that the accuracy of using EO data for monitoring UK crop growth is much more sensitive to cloud cover when compared to that of the temporal resolution of the sensor.

5.4.2. Benefits of the dual Sentinel-2 constellation

The launch of the second Sentinel-2 satellite (i.e. Sentinel-2B) – planned for mid-2016 – is expected to improve operational crop monitoring when compared to the capabilities offered by current high spatial resolution sensors. Each of the Sentinel-2 sensors will provide multi-spectral observations with a spatial resolution of 10 m (for four visible and near-infrared bands), 20 m (for six red-edge/shortwave-infrared bands) and 60 m (for three atmospheric correction bands). Based on the error analysis for resolving the detail within typical UK field sizes, these spatial resolutions correspond to a mean error of 1.24% (10 m), 2.47% (20 m) and 5.93% (60 m).

The operational Sentinel-2 satellite pair are designed to deliver observations covering the terrestrial land surface every five days. Assuming cloud-free conditions, this temporal resolution will provide an average of 68 observations within the average UK winter wheat growing season – i.e. 31st September (sowing date) and 27th July (harvest date). Consequently, from analysing the temporal resolution errors, this large number of observations would correspond to a low mean error of only 0.1% when comparing between the daily estimates and the linearly interpolated 5-day estimates. However, when accounting for image obscurity due to cloud cover over the UK cropland areas, this mean error could increase to 23%. With the cloud cover, the number of available Sentinel-2 acquisitions within the growing season could potentially be reduced to only 17, which is equivalent to an EO sensor with a temporal resolution of 20 days. The temporal analysis results of this research are within the bounds of that estimated in Verrelst *et al.* (2015) where, considering the presence of cloud cover, the Sentinel-2 satellites are expected to deliver imagery every 15-30 days.

Based on the temporal and spatial resolutions, it is likely that Sentinel-2 would become a major source of future EO data. However, given the spatial and temporal extents of past and present sensors, the use of archived EO data from would still be of value. For instance, in the context of precision agriculture, Mulla (2013) mentions that fine scale EO data – such as that from Landsat, SPOT and QuickBird – would allow an analysis of fields over multiple crop growth seasons/years in order to identify potential managements zones. This archived EO data can be further combined with real-time data (i.e. Sentinel-2) in order to refine the locations of the management zones. An accurate quantification of the likely spatial and temporal resolution errors, as detailed in this research, is also valuable when combining EO data with models within a data assimilation framework (Ines *et al.*, 2013;

Revill *et al.*, 2013, see Chapter 2; Sus *et al.*, 2013; Zhao *et al.*, 2013; Li *et al.*, 2014; Huang *et al.*, 2016).

5.4.3. Research caveats

This research has an explicit focus on the spatial and temporal resolution errors when using EO sensor for monitoring crop growth at the field-scale. However, a major source of error and uncertainty is typically introduced in the retrieval of LAI (Doraiswamy *et al.*, 2004; Fang *et al.*, 2011; Casa *et al.*, 2012), which was not considered in this analysis. For instance, the empirical LAI retrieval approach was based on a calibration that was derived from LAI observations at the field sites detailed in Chapter 2. And so, since the coefficients used in equations 5.1 and 5.2 were based on a statistical relationship at alternative fields sites, they may not be valid for the cropland areas investigated in this study. In spite of this, Wei *et al.* (2015) discusses the importance of EO-derived normalised difference vegetation index (NDVI), calculated using the red and near-infrared wavebands only, for monitoring crop phenology.

The premise of the temporal resolution analysis is based on the absolute temporal resolution, i.e. the number of days between two consecutive EO acquisitions of exactly the same area at the same viewing geometry. However, there is often overlap between images acquired from adjacent orbits and EO sensors can also be pointed accordingly to image the same area in different orbits (NRC, 2014). Therefore, the actual temporal resolution of EO sensors is typically higher than that reproduced in the synthetic LAI time-series.

In the simulation of potential cloud cover, observations on days that were flagged as cloudy, based on an 11-year analysis of MODIS 250 m QA layer data, were removed from the synthetic LAI time-series. This is a gross simplification for two reasons: first, if a given day of year is flagged as cloudy even once over the entire 11-year period then it is removed from the LAI time-series. This procedure assumes a worse-case scenario in which only days that were 100% cloud-free throughout the period were retained in the LAI dataset. This analysis could have been extended to include probability thresholds to evaluate the impacts of cloud cover obscurity. For instance, Whitcraft *et al.* (2015) used probability thresholds of 70%, 80% and 90% for of clear-sky observations during four key phenological dates. However, Whitcraft *et al.* (2015) used MODIS QA data at 1 km resolution which is likely to exceed the size of some cloud elements. Second, the cloud cover analysis is also simplified due to the assumption of the entire 250 m MODIS pixel being occupied by cloud. As cloud cover is typically fragmented, realistically it is possible that a fraction of a 250 m pixel area on a given day of year would encompass areas that are sufficiently cloud-free.

This research demonstrates that cloud cover can potentially result in observations gaps in an optical EO time-series used to monitor crop growth stages. However, the use of crop canopy variables derived from Synthetic Aperture Radar (SAR) sensors can provide fine-scale observations and, using active microwave signals, they are unaffected by clouds. And so, as demonstrated in Chapter 2, this research recommends the combined use of high resolution optical and SAR EO sensor data, which will effectively increase the frequency of observations within the growing season.

5.5. Conclusion

Determining the appropriate spatial and temporal resolutions of an EO sensor is of fundamental importance for meeting the requirements of a particular agricultural application. In the context of operational crop growth monitoring at typical UK field-scales (estimated as 7.93 ha), this research approximates errors linked to the typical spatial and temporal resolutions of current optical EO sensor missions. The minimum EO spatial resolution of around 165 m is required to resolve UK fields – although higher resolutions would be expected to reduce the error and uncertainty in the per-field estimates. When accounting for cloudy days, which could potentially obscure observations, EO sensors with a 26-day absolute temporal resolution (e.g. SPOT-6/7) could have errors up to 63%. However, due to overlap of the imaged area between adjacent orbits of the EO instrument platform, the actual temporal resolution of the sensor would be much higher. The degree of cloud cover estimated in this analysis is likely to be over-estimated; correspondingly, the error associated with crop monitoring would be lower. When extrapolating this analysis framework to data that could be derived from the dual Sentinel-2 sensors, the likely errors were estimated to be only 1.24% and 23% for the spatial and temporal resolution of the Sentinel-2 mission, respectably.

5.6. Summary

Where the previous chapter (Chapter 4) discussed the scale mismatch between 1 km MODIS LAI data and UK field sizes, this research quantifies the errors associated with optical EO sensor spatial and temporal resolution – specifically for UK field-scale crop monitoring. Generally, this analysis has demonstrated that an EO sensor with a spatial resolution of greater than 225 m is required to resolve the within-field detail. When accounting for likely cloud cover, EO sensors with a temporal resolution of 26 days could have errors of up to 63%.

CHAPTER 6

Summary: Discussions, Recommendations and Conclusions

6.1. Key research outcomes

In this section the original key questions, as outlined in Chapter 1 (Section 1.6), are restated, followed by a summary of the results and discussions from research Chapters 2 to 5.

6.1.1. Impact of assimilating EO data on simulated C fluxes

In Chapter 2, leaf area index (LAI) estimates, derived from optical (SPOT-2/4) and SAR (ERS-2) Earth observation (EO) data, were assimilated into the Soil-Plant-Atmosphere crop (SPAc) model. The ensemble Kalman Filter (EnKF) sequential data assimilation (DA) algorithm was used to update the simulation of LAI estimates. Improvements in the simulated net ecosystem exchange (NEE) fluxes with the assimilation of optical and SAR EO-derived LAI estimates – both individually and synergistically – were evaluated based on a comparison to FLUXNET eddy-covariance data. The following research questions were answered:

1) To what extent can the assimilation of EO-derived LAI improve NEE flux estimates of winter cereal crops at the field-scale?
2) Is the model DA framework valid for multiple European cropland sites?

From assimilating all EO LAI estimates the simulation of the at-harvest cumulative NEE fluxes was improved by an average of 69% when compared to the estimate error without the DA of LAI. However, a greater improvement in the cumulative NEE of 79% was achieved from assimilating the SAR LAI only (i.e. as opposed to the combination of optical and SAR estimates). This improvement suggests that the model framework, including the parameterisation and LAI retrieval calibration coefficients, are sufficiently accurate and can reliably enhance the forecasting of winter wheat C fluxes at multiple European crop sites of differing climatic conditions.

6.1.2. Evaluating simplified modelling approaches

The impacts of reduced crop model complexity, including the spatio-temporal resolution of meteorological driving data, are investigated in Chapter 3. The simplified Aggregated Canopy Model (ACM) was used, which requires only minimal parameters and runs at daily time-steps. ACM is calibrated based on the output of the more detailed SPAc model that operates at half-hourly time-steps whilst simulating leaf-level processes. The calibration was applied across eight European winter wheat sites and was further evaluated when using gridded atmospheric re-analysis drivers (i.e. as opposed to local meteorological observations), in order to answer the questions:

1) How does model complexity influence estimates of photosynthesis?

2) How do single-site and multi-site photosynthesis calibrations compare across European cereal crop sites?

3) How do the complex and simple model photosynthesis estimates compare when

driven by atmospheric re-analysis data?

The calibrated ACM model generally had a consistently high correlation to SPAc photosynthesis estimates. Therefore, a reduction in model complexity, including temporal resolution (i.e. half-hourly to daily time-steps), does not significantly diminish the overall accuracy of photosynthesis estimates at daily timescales. From comparing between outputs from the single-site and multi-site ACM calibrations to SPAc estimates, accuracy and biases in ACM photosynthesis estimates were consistent in magnitude. And so, a generic and robust ACM calibration for winter wheat photosynthesis was produced. With both models driven with atmospheric re-analysis data, the ACM photosynthesis estimates also had a high agreement with the SPAc model. Therefore, the propagation of driver data uncertainty impacted the two models to a similar degree.

6.1.3. Model-data fusion for regional upscaling

In Chapter 4, a model-data fusion framework was evaluated for the estimation of winter wheat yields at six UK regions between the years 2000 to 2013. The DALECc model – driven by photosynthesis estimates from the ACM multi-site calibration detailed in Chapter 3 – was used to produce regional crop yield estimates that are validated using official yield statistics. Through a calibration of canopy development, coarse-scale (1 km) MODIS EO LAI estimates were also used to constrain the DALECc estimates to answer the questions:

1) What is the empirical relationship between MODIS LAI and crop yields across UK regions?
2) What is the accuracy of grid-scale crop model yield estimates when aggregated to regional-scales?
3) Can MODIS LAI be used to constrain and improve the model estimates of yield?

A weak linear relationship (mean $R^2 = 0.29$) existed between the mean maximum MODIS LAI and yield data. For cereal crops the time of peak LAI coincides with that of flowering and grain filling (Mkhabela *et al.*, 2011), therefore yield can be correlated with maximum LAI (Forbes and Watson, 1992). The DALECc model yield had a mean error of 0.71 t ha^{-1} when compared to official yield statistics over the 13-year period. The use of the MODIS LAI was not successful in reducing errors in DALECc yield estimates, which is likely due to sub-pixel heterogeneity in response to scale mismatches between the 1 km LAI product and relatively small UK field sizes. However, a decrease in the model biases was achieved using the LAI data for the majority of regions. This overall reduction in bias also coincided with a reduction in the bias of the DALECc LAI estimates when compared to the MODIS LAI.

6.1.4. EO data spatial and temporal resolution requirements for crop growth monitoring

Errors linked to EO sensor spatial and temporal resolution for UK crop monitoring were quantified. The spatial resolution errors were determined by aggregating high resolution (5 m) LAI pixels to reproduce estimates from medium (10-250 m) to coarse-scale (> 250 m) EO sensors. Using a field mask, per-field samples were made from the aggregated images and compared to those from the original fine-scale data. Analysing temporal resolution errors involved resampling daily LAI estimates from the DALECc model (calibrated and evaluated in Chapters 2 and 3) to mimic the observation frequencies of current sensors. The LAI data was also filtered to remove observations on potentially cloudy days. The data was then compared to the original daily times-series in order to evaluate the impacts of reducing the observation frequency. The following questions were answered:

1) What is the minimum EO sensor spatial resolution required to monitor crops at field-scales that are characteristic of UK agriculture?

2) How does temporal resolution and likely cloud cover influence the effectiveness of optical EO sensors for tracking winter wheat growth over cropland landscapes?

3) What are the expected benefits of the dual Sentinel-2 satellite constellation (i.e. Sentinel-2A and 2B) for multi-temporal crop monitoring at UK field-scales?

The calculated mean maximum pixel size (i.e. the coarsest spatial resolution required to adequately resolve fields) ranged from 100 to 225 m. This range in coarsest pixel size is also comparable to that approximated by Duveiller and Defourny (2010) where sizes ranged from 120 to 300 m for multiple European regions. Errors in using optical EO data for crop growth monitoring over UK croplands were 28%, 48% and 63% for a temporal resolution of 10 days (e.g. Sentinel-2), 16 days (e.g. Landsat-7/8) and 26 days (e.g. SPOT-6/7), respectively.

Based on the spatial resolution errors analysis, the 10 m spatial resolution of Sentinel-2 EO data would be expected to have a mean error of 1.0% with a 5/95-percentile range of ±0.5%. Therefore, the spatial resolution of Sentinel-2 would be expected to accurately resolve the spatial detail within typical UK field sizes. The forthcoming launch of the second Sentinel-2 satellite will effectively increase the current temporal resolution – from 10 to 5 days. And so, based on the temporal analysis accounting for potential cloud cover, a 5-day temporal resolution corresponds to an error of 23.3% when monitoring winter wheat crop growth.

6.2. Research findings: opportunities for industry

The EO data processing and modelling approaches evaluated in this thesis demonstrate benefits to support the monitoring of crop growth and yield in an operational and commercial context. The generalised framework detailed in Chapter 5 could be applied to any cropland landscape to determine the optical EO spatial and temporal resolutions required to resolve field-scale detail. This information can then be used to monitor the within-field spatial variability in crop growth condition (e.g. Figure 6.1), data on which would be required to support decision-making in applications of precision agriculture

(Mulla, 2013). For instance, EO data could be used to distinguish sub-regions of fields that could be used as management zones that could each receive customised inputs of fertilisers and herbicides. The analysis of additional imagery throughout a crop season could then be used to modify the extents of management zones and update the inputs. Furthermore, Hedley (2015) estimates that using spatio-temporal crop condition maps in conjunction with GPS-enabled automated guidance technologies, used by agricultural vehicles, can increase management efficiencies by up to 15% to 30% (e.g. through reducing overlaps and gaps when applying fertilisers).

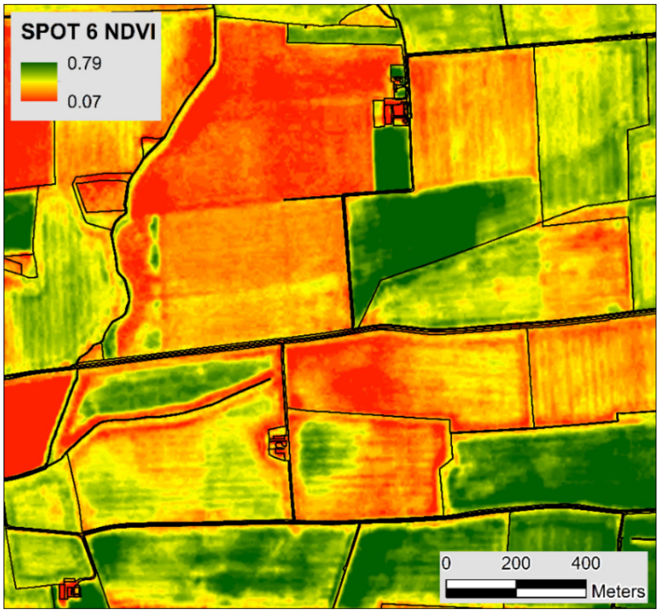

Figure 6.1: Example SPOT-6 normalised difference vegetation index (NDVI) image indicating the spatial variability of crop growth at the field-scale (source: Airbus Defence and Space).

The benefits of EO data in supporting the agri-business sector will be further enhanced by the fully operational Sentinel-1 and Sentinel-2 (SAR and optical) EO satellite pairs, data from which will also be available for commercial use free of charge. The high spatial and temporal resolutions offered by these Sentinel sensors will potentially develop upon the current cropland monitoring capabilities. And so, these developments could improve information on crop production through the timely delivery of information on crop status, crop area and yield forecasts (Bontemps *et al.*, 2015). In particular, the use of Sentinel data would be a valuable contribution to the Group on Earth Observation's Global Agricultural Monitoring (GEOGLAM) framework (Justice and Becker-Reshef, 2007). GEOGLAM is a G20-mandated activity for crop monitoring using EO data (Soares *et al.*, 2011; Whitcraft *et al.*, 2015), which specifically aims to integrate satellite EO data and ground observations to provide services, including the regular monitoring of both climatic variables and condition of multiple crop types at local, national and global scales (GEOGLAM, 2015).

Although EO sensors can determine the crop condition at a given point in time, the field-scale spatial variability in yield is due to a combination of factors, including water stress, nutrients, rooting depth, soil properties, drainage, weather, pests and management (Thorp *et al.*, 2008). The use of the detailed SPAc model can capture some of the causes of yield variability that are related to weather and management. Specifically, the simulated developmental rate, and subsequent carbon allocation to yield, is calculated based on daily observations of temperature and radiation. The overall length and timing of the crop growing period is further dependant on the sowing and harvesting dates. As demonstrated in Chapter 2, available fine scale EO data can be sequentially assimilated into SPAc (or

DALECc) in order to update the model state variables. Crop models, applied at points within a field to generate daily estimates, can therefore compliment the information inferred from EO sensors and further contribute towards the precision farming toolkit.

Although areas of development were highlighted with the SPAc and DALECc models, particularly with regards to C allocation to grain (as discussed in Chapters 2 and 4), the use of models combined with EO data can potentially provide a powerful framework for the reliable forecasting of crop yields that would have considerable economic benefits at a range of spatial scales. For instance, the regional-scale analysis detailed in Chapter 4 demonstrated the use of only coarse-scale EO data for reducing biases in yield estimates. At regional to national-scales, in terms of global agricultural markets, crop prices are volatile due to fluctuations in crop production – in response to climate variability (López-Lozano *et al.*, 2015). And so, crop yield forecasts at regional-scales are essential for providing objective information that can be used to ensure national food security whilst minimising economic risks.

6.3. Recommendations for future research

Chapter 2 demonstrated the sequential DA of high resolution EO data for improving the performance of the SPAc model. Furthermore, the photosynthesis simulated by SPAc can be reproduced the using a simpler model – ACM (detailed in Chapter 3) – that operates at daily (as opposed to half-hourly) time-steps; thus reducing driver requirements and decreasing the computational demand. And so, based on these findings, a future research direction would be to apply the same sequential DA scheme to update the DALECc C allocation model when driven using ACM photosynthesis estimates. Since ACM can also generate photosynthesis when driven with spatially aggregated meteorological data, this sequential DA approach could offer a more practical solution for estimating C fluxes at alternative crop sites where information on management inputs is less well known.

Research in chapter 4 evaluates the regional-scale application of DALECc, driven with the ACM photosynthesis multi-site calibration (detailed in Chapter 3). MODIS LAI was also used to constrain the DALECc simulation of canopy development. Reductions in the model biases were achieved; however, due to the average UK field size (estimated as 7.93 ha, see Chapter 5: Table 5.1) it is likely that the 1 km spatial resolution of MODIS LAI was largely insufficient for resolving the field-scale detail. And so, the research in Chapter 4 was considered a benchmark for future research involving the use of higher spatial resolution EO sensor data, which would resolve the field-scale detail more accurately.

In addition to LAI, existing EO products with regional to global coverage include MODIS daily (and 8-daily) surface reflectance at 250 m spatial resolutions. Although the spatial resolution of this MODIS data is less than the minimum resolution required for UK crop monitoring, which was estimated as 225 m (see Chapter 5), it is expected that significant improvements could be achieved when compared to the 1 km LAI data used in Chapter 4. However, the MODIS reflectance product – comprising of data centred on the red and near-infrared wavebands – cannot be directly assimilated into DALECc and would require the retrieval of LAI through either empirical or physical-based models.

Retrieving accurate LAI estimates from EO data is challenging and typically limits the validity of a DA scheme when applied at regional-scales and alternative crop types (Doraiswamy *et al.*, 2004; Fang *et al.*, 2011). Chapter 2 demonstrated the use of an empirical algorithm for retrieving LAI based on a relationship between EO data and ground measured LAI. However, since this empirical relationship was established locally it may not be valid over large areas (Yuping *et al.*, 2008). As an alternative to this empirical approach, further studies could investigate the coupling of DALECc to a radiative transfer model, which can be parameterised to simulate the key absorption and scattering properties of light within a crop canopy. Through a knowledge of the illumination geometry, radiative transfer models, such as the Scattering by Arbitrary Inclined Leaves (SAIL; Verhoef, 1984, 1985) model, essentially incorporates an understanding of the processes that link canopy biophysical variables to canopy reflectance (Baret *et al.*, 2000). And so, future research could involve the coupling of DALECc to a calibrated and inverted radiative transfer model (e.g. Koetz *et al.*, 2005; Yuping *et al.*, 2008; Ma *et al.*, 2013). Thus, this radiative transfer model inversion could allow for the direct use of EO reflectance data to simulate LAI, which could then be used to update the DALECc model estimates.

Research in Chapter 5 hypothesized the impacts of temporal gaps in optical EO data, including that due to cloud cover, when monitoring crop growth across UK landscapes. Furthermore, in Chapter 4, the 8-day composite MODIS LAI estimates were filtered to remove days that were flagged as cloudy. However, both studies could include an evaluation of filtering algorithms used for the gap-filling of LAI time-series. For instance, the Savitzky-Golay filter (SG, Savitzky and Golay, 1964) has been commonly applied to smooth the noise in MODIS LAI and NDVI data products used to monitor crop growth (e.g. Fang *et al.*, 2011; Xu *et al.*, 2011; Zhao *et al.*, 2013; Huang *et al.*, 2015; Wei *et al.*, 2015; Yao *et al.*, 2015; Huang *et al.*, 2016).

Accurately determining the uncertainty of EO data, along with the crop model uncertainty, is an important pre-requisite for sequential DA schemes. Therefore, the research detailed in Chapter 5 – investigating uncertainty linked to optical EO sensor spatial and temporal resolutions – could be extended to using within a sequential DA scheme. Specifically, noise could be added to the synthetic LAI time-series estimates to mimic the uncertainties due to spatial heterogeneity. This LAI data, further filtered to reflect EO sensor temporal resolution and cloud cover obscurity, could then be assimilated into the DALECc model. This DA approach potentially provides a powerful synthetic analysis, which could allow for the evaluation of uncertainty, combined with the timings and frequencies of assimilated estimated, on simulated crop canopy development and yield.

Crop models have typically been calibrated and evaluated to simulate the dynamics of crop growth under optimum environmental conditions, i.e. business-as-usual scenarios (Zhao et al., 2013). For instance, the SPAc and DALECc models evaluated in this thesis simulate the maximum possible development of crops as a function of temperature, photoperiod and vernalisation (see Chapter 4: Section 4.2.3). However, other factors, including soil moisture, can also influence the developmental rate of crops (Penning de

Vries *et al.*, 1989; Sus *et al.*, 2012). And so, additional research could investigate the impacts of adverse conditions, such as drought, on crop model estimates.

6.4. Summary conclusions

The research chapters (Chapters 2 to 5) of this thesis addressed the key issues associated with the spatial and temporal upscaling of crop model estimates of C fluxes and stocks. These issues broadly included evaluating approaches for combining models with EO data, investigating the model complexity and determining EO data resolution requirements for operational crops monitoring over UK landscapes. The conclusions from this research can be summarised as: first, the assimilation of fine-scale optical and radar EO data can improve crop model estimates of daily and cumulative C fluxes. However, the individual assimilation of radar data (i.e. without being combined with optical data) resulted in further enhancements in the C flux estimates. Second, a simplified model of cereal crop photosynthesis – simulating canopy-scale processes at daily time-steps – can be calibrated to reproduce estimates generated from a more complex, and thus more computationally intensive model, which simulates leaf-level processes at half-hourly time-steps. Furthermore, a high agreement existed between the two models, and with independent photosynthesis estimates, when both models were driven with 1.0° resolution (≈ 11.13 km) gridded meteorological data. Third, coarse-scale (1 km) EO data can be used to constrain models and reduce biases in regional-scale estimates of canopy development and yield. However, the use of higher resolution EO sensors would be expected to improve the yield estimates. And fourth, a minimum EO spatial resolution of around 165 m is required to resolve the average field-scale detail of UK croplands. Furthermore, Monitoring crop growth using EO sensors with a 26-day temporal resolution resulted in a mean error of 5%; however, accounting for likely cloud cover increased this error to 63%.

References

Alexandratos, N., Bruinsma, J., 2012. World Agriculture Towards 2030/2050: The 2012 Revision. In: Organisation, F.a.A. (Ed.), Rome.

Allen, R.G., Pereira, L.S., Raes, D., Smith, M., 1998. Crop evapotranspiration - Guidelines for computing crop water requirements - FAO Irrigation and drainage paper 56. FAO - Food and Agriculture Organization of the United Nations, Rome.

Asseng, S., Ewert, F., Rosenzweig, C., Jones, J.W., Hatfield, J.L., Ruane, A.C., Boote, K.J., Thorburn, P.J., Rotter, R.P., Cammarano, D*., et al.*, 2013. Uncertainty in simulating wheat yields under climate change. Nature Clim. Change 3, 827-832.

Asseng, S., Foster, I.A.N., Turner, N.C., 2011. The impact of temperature variability on wheat yields. Global Change Biology 17, 997-1012.

Atzberger, C., 2013. Advances in Remote Sensing of Agriculture: Context Description, Existing Operational Monitoring Systems and Major Information Needs. Remote Sensing 5, 949-981.

Baghdadi, N., Boyer, N., Todoroff, P., El Hajj, M., Bégué, A., 2009. Potential of SAR sensors TerraSAR-X, ASAR/ENVISAT and PALSAR/ALOS for monitoring sugarcane crops on Reunion Island. Remote Sensing of Environment 113, 1724-1738.

Bajzelj, B., Richards, K.S., Allwood, J.M., Smith, P., Dennis, J.S., Curmi, E., Gilligan, C.A., 2014. Importance of food-demand management for climate mitigation. Nature Clim. Change 4, 924-929.

Baldocchi, D., Falge, E., Gu, L., Olson, R., Hollinger, D., Running, S., Anthoni, P., Bernhofer, C., Davis, K., Evans, R*., et al.*, 2001. FLUXNET: A New Tool to Study the Temporal and Spatial Variability of Ecosystem Scale Carbon Dioxide, Water Vapor, and Energy Flux Densities. Bulletin of the American Meteorological Society 82, 2415-

2434.

Baldocchi, D.D., 2003. Assessing the eddy covariance technique for evaluating carbon dioxide exchange rates of ecosystems: past, present and future. Global Change Biology 9, 479-492.

Balkovič, J., van der Velde, M., Schmid, E., Skalský, R., Khabarov, N., Obersteiner, M., Stürmer, B., Xiong, W., 2013. Pan-European crop modelling with EPIC: Implementation, up-scaling and regional crop yield validation. Agricultural Systems 120, 61-75.

Baret, F., Weiss, M., Troufleau, D., Prevot, L., Combal, B., 2000. Maximum information exploitation for canopy characterisation by remote sensing. Aspects of Applied Biology 60, 71-82.

Baronti, S., Del Frate, F., Paloscia, S., Pampaloni, P., Schiavon, G., Solimini, D., 1993a. SAR polarimetric features of agricultural areas. Geoscience and Remote Sensing Symposium, 1993. IGARSS '93. Better Understanding of Earth Environment, International 1, 27-29.

Baronti, S., Del Frate, F., Paloscia, S., Pampaloni, P., Schiavon, G., Solimini, D., 1993b. SAR polarimetric features of agricultural areas. Geoscience and Remote Sensing Symposium, 1993. IGARSS '93. Better Understanding of Earth Environment., International, pp. 27-29 vol.21.

Bauer, M.E., Cipra, J.E., 1973. Identification of Agricultural Crops by Computer Processing of ERTS MSS Data. LARS Technical Reports. Laboratory for Applications of Remote Sensing.

Becker-Reshef, I., Vermote, E., Lindeman, M., Justice, C., 2010. A generalized regression-based model for forecasting winter wheat yields in Kansas and Ukraine using MODIS data. Remote Sensing of Environment 114, 1312-1323.

Bloom, A.A., Williams, M., 2015. Constraining ecosystem carbon dynamics in a data-limited world: integrating ecological "common sense" in a model–data fusion framework. Biogeosciences 12, 1299-1315.

Bolton, D.K., Friedl, M.A., 2013. Forecasting crop yield using remotely sensed vegetation indices and crop phenology metrics. Agricultural and Forest Meteorology 173, 74-84.

Bondeau, A., Smith, P.C., Zaehle, S., Schaphoff, S., Lucht, W., Cramer, W., Gerten, D., Lotze-Campen, H., Müller, C., Reichstein, M*., et al.*, 2007. Modelling the role of agriculture for the 20th century global terrestrial carbon balance. Global Change Biology 13, 679-706.

Bontemps, S., Arias, M., Cara, C., Dedieu, G., Guzzonato, E., Hagolle, O., Inglada, J., Morin, D., Rabaute, T., Savinaud, M*., et al.*, 2015. "Sentinel-2 for agriculture": Supporting global agriculture monitoring. Geoscience and Remote Sensing Symposium (IGARSS), 2015 IEEE International, pp. 4185-4188.

Boote, K.J., Jones, J.W., White, J.W., Asseng, S., Lizaso, J.I., 2013. Putting mechanisms into crop production models. Plant, Cell & Environment 36, 1658-1672.

Bouman, B.A.M., 1995. Crop modelling and remote sensing for yield prediction. Netherlands Journal of Agricultural Science 43, 143 - 161.

Brown, J.C., Kastens, J.H., Coutinho, A.C., Victoria, D.d.C., Bishop, C.R., 2013. Classifying multiyear agricultural land use data from Mato Grosso using time-series MODIS vegetation index data. Remote Sensing of Environment 130, 39-50.

Brown, M.E., de Beurs, K.M., 2008. Evaluation of multi-sensor semi-arid crop season parameters based on NDVI and rainfall. Remote Sensing of Environment 112, 2261-2271.

Cairns, B., 1995. Diurnal variations of cloud from ISCCP data. Atmospheric Research 37, 133-146.

Campbell, G.S., Norman, J.M., 1989. The description and measurement of plant canopy structure. In: Russell, G., Marshall, B. (Eds.), Plant Canopies: Their Growth, Form and Function. Cambridge University Press, Cambridge, UK, pp. 1-19.

Casa, R., Varella, H., Buis, S., Guérif, M., De Solan, B., Baret, F., 2012. Forcing a wheat crop model with LAI data to access agronomic variables: Evaluation of the impact of model and LAI uncertainties and comparison with an empirical approach. European Journal of Agronomy 37, 1-10.

CEH, 2014. Daily temperature range, Near-Surface Air Temperature, Surface Downwelling Shortwave Radiation. Centre for Ecology and Hydrology.

Ceschia, E., Béziat, P., Dejoux, J.F., Aubinet, M., Bernhofer, C., Bodson, B., Buchmann, N., Carrara, A., Cellier, P., Di Tommasi, P., *et al.*, 2010. Management effects on net ecosystem carbon and GHG budgets at European crop sites. Agriculture, Ecosystems & Environment 139, 363-383.

Challinor, A.J., Watson, J., Lobell, D.B., Howden, S.M., Smith, D.R., Chhetri, N., 2014. A meta-analysis of crop yield under climate change and adaptation. Nature Clim. Change advance online publication.

Challinor, A.J., Wheeler, T.R., Craufurd, P.Q., Slingo, J.M., Grimes, D.I.F., 2004. Design and optimisation of a large-area process-based model for annual crops. Agricultural and Forest Meteorology 124, 99-120.

Chen, B., Coops, N.C., Fu, D., Margolis, H.A., Amiro, B.D., Barr, A.G., Black, T.A., Arain, M.A., Bourque, C.P.A., Flanagan, L.B., *et al.*, 2011. Assessing eddy-covariance flux tower location bias across the Fluxnet-Canada Research Network based on remote sensing and footprint modelling. Agricultural and Forest Meteorology 151, 87-100.

Ciais, P., Gervois, S., Vuichard, N., Piao, S.L., Viovy, N., 2011. Effects of land use change and management on the European cropland carbon balance. Global Change Biology 17, 320-338.

Clevers, J.G.P.W., 1988. The derivation of a simplified reflectance model for the estimation of leaf area index. Remote Sensing of Environment 25, 53-69.

Clevers, J.G.P.W., 1991. Application of the WDVI in estimating LAI at the generative stage of barley. ISPRS Journal of Photogrammetry and Remote Sensing 46, 37-47.

Clevers, J.G.P.W., Baker, C., van Leeuwen, H.J.C., Bouman, B.A.M., 1994. A framework for monitoring crop growth by combining directional and spectral remote sensing information. Remote Sensing of Environment 50, 161-170.

Colby, J., 1991. Topographic Normalization in Rugged Terrain. Photogrammetric Engineering and Remote Sensing 57, 531-537.

Conrad, C., Fritsch, S., Zeidler, J., Rücker, G., Dech, S., 2010. Per-Field Irrigated Crop Classification in Arid Central Asia Using SPOT and ASTER Data. Remote Sensing 2, 1035.

Coucheney, E., Buis, S., Launay, M., Constantin, J., Mary, B., García de Cortázar-Atauri, I., Ripoche, D., Beaudoin, N., Ruget, F., Andrianarisoa, K.S*., et al.*, 2015. Accuracy, robustness and behavior of the STICS soil–crop model for plant, water and nitrogen outputs: Evaluation over a wide range of agro-environmental conditions in France. Environmental Modelling & Software 64, 177-190.

De Wit, A., Duveiller, G., Defourny, P., 2012. Estimating regional winter wheat yield with WOFOST through the assimilation of green area index retrieved from MODIS observations. Agricultural and Forest Meteorology 164, 39-52.

de Wit, A.J.W., van Diepen, C.A., 2007. Crop model data assimilation with the Ensemble

Kalman filter for improving regional crop yield forecasts. Agricultural and Forest Meteorology 146, 38-56.

DEFRA, 2012. Farming Statistics Provisional crop areas, yields and livestock populations At June 2013, United Kingdom. Farming Statistics, Department for Environment, Food and Rural Affairs, p. 21.

DEFRA, 2013. Farming Statistics Provisional crop areas, yields and livestock populations At June 2013, United Kingdom. Farming Statistics, Department for Environment, Food and Rural Affairs, p. 21.

DEFRA, 2015. Structure of the agricultural industry in England and the UK at June: annual time series: 1983 to 2015.

Delecolle, R., Maas, S.J., Guerif, M., Baret, F., 1992. Remote sensing and crop production models: present trends. ISPRS Journal of Photogrammetry and Remote Sensing, pp. 145-161.

Dente, L., Satalino, G., Mattia, F., Rinaldi, M., 2008. Assimilation of leaf area index derived from ASAR and MERIS data into CERES-Wheat model to map wheat yield. Remote Sensing of Environment 112, 1395-1407.

Doraiswamy, P.C., Hatfield, J.L., Jackson, T.J., Akhmedov, B., Prueger, J., Stern, A., 2004. Crop condition and yield simulations using Landsat and MODIS. Remote Sensing of Environment 92, 548-559.

Doraiswamy, P.C., Sinclair, T.R., Hollinger, S., Akhmedov, B., Stern, A., Prueger, J., 2005. Application of MODIS derived parameters for regional crop yield assessment. Remote Sensing of Environment 97, 192-202.

Dorigo, W.A., Zurita-Milla, R., de Wit, A.J.W., Brazile, J., Singh, R., Schaepman, M.E., 2007. A review on reflective remote sensing and data assimilation techniques for enhanced agroecosystem modeling. International Journal of Applied Earth Observation and Geoinformation 9, 165-193.

Duveiller, G., Baret, F., Defourny, P., 2012. Remotely sensed green area index for winter wheat crop monitoring: 10-Year assessment at regional scale over a fragmented landscape. Agricultural and Forest Meteorology 166–167, 156-168.

Duveiller, G., Baret, F., Defourny, P., 2013. Using Thermal Time and Pixel Purity for Enhancing Biophysical Variable Time Series: An Interproduct Comparison. Geoscience and Remote Sensing, IEEE Transactions on 51, 2119-2127.

Duveiller, G., Defourny, P., 2010. A conceptual framework to define the spatial resolution requirements for agricultural monitoring using remote sensing. Remote Sensing of Environment 114, 2637-2650.

Duveiller, G., Defourny, P., Gerard, B., 2008. A Method to Determine the Appropriate Spatial Resolution Required for Monitoring Crop Growth in a given Agricultural Landscape. Geoscience and Remote Sensing Symposium, 2008. IGARSS 2008. IEEE International, pp. III - 562-III - 565.

Eckhardt, D.W., Verdin, J.P., Lyford, G.R., 1990. Automated update of an irrigated lands GIS using SPOT HRV imagery. Photogrammetric Engineering & Remote Sensing 56, 1515-1522.

Entekhabi, D., Njoku, E.G., O'Neill, P.E., Kellogg, K.H., Crow, W.T., Edelstein, W.N., Entin, J.K., Goodman, S.D., Jackson, T.J., Johnson, J*., et al.*, 2010. The Soil Moisture Active Passive (SMAP) Mission. Proceedings of the IEEE 98, 704-716.

EOSDIS, 2009. Earth Observing System ClearingHouse (ECHO) / Reverb Version 10.X. Greenbelt, MD.

Eurostat, 2013a. Key farm variables: area, livestock (LSU), labour force and standard output (SO) by agricultural size of farm (UAA), legal status of holding and NUTS 2 regions.

Eurostat, 2013b. Land cover and land use, landscape (LUCAS). European Commission.

Eurostat, 2015. Crop statistics (from 2000 onwards). European Commission.

Evensen, G., 2003. The Ensemble Kalman Filter: theoretical formulation and practical implementation. Ocean Dynamics 53, 343-367.

Ewert, F., van Ittersum, M.K., Heckelei, T., Therond, O., Bezlepkina, I., Andersen, E., 2011. Scale changes and model linking methods for integrated assessment of agri-environmental systems. Agriculture, Ecosystems & Environment 142, 6-17.

Fang, H., Liang, S., Hoogenboom, G., 2011. Integration of MODIS LAI and vegetation index products with the CSM–CERES–Maize model for corn yield estimation. International Journal of Remote Sensing 32, 1039-1065.

FAO, 2002. Second Expert Meeting on Harmonizing Forest-Related Definitions for Use by Various Stakeholders. Second Expert Meeting on Harmonizing Forest-Related Definitions for Use by Various Stakeholders. FAO, Rome.

FAO, 2015a. Production / Crops. FAOSTAT. Food and Agricultural Organisaiton of the United Nations.

FAO, 2015b. Production quantities by country. In: FAO (Ed.), Food and Agricultural Organisation of the United Nations Statistical Division.

Farquhar, G.D., von Caemmerer, S., 1982. Modelling of Photosynthetic Response to Environmental Conditions. In: Lange, O.L., Nobel, P.S., Osmond, C.B., Ziegler, H. (Eds.), Physiological Plant Ecology II. Springer Berlin Heidelberg, pp. 549-587.

Ferrazzoli, P., Guerriero, L., Quesney, A., Taconet, O., Wigneron, J.P., 1999a.

Investigating the capability of C-band radar to monitor wheat characteristics. Geoscience and Remote Sensing Symposium, 1999. IGARSS '99 Proceedings. IEEE 1999 International, pp. 723-725 vol.722.

Ferrazzoli, P., Guerriero, L., Quesney, A., Taconet, O., Wigneron, J.P., 1999b. Investigating the capability of C-band radar to monitor wheat characteristics. Geoscience and Remote Sensing Symposium, 1999. IGARSS '99 Proceedings. IEEE 1999 International 2, 723-725.

Finnigan, J.J., Clement, R., Malhi, Y., Leuning, R., Cleugh, H.A., 2003. A Re-Evaluation of Long-Term Flux Measurement Techniques Part I: Averaging and Coordinate Rotation. Boundary-Layer Meteorology 107, 1-48.

Fischer, A., Kergoat, L., Dedieu, G., 1997. Coupling satellite data with vegetation functional models: Review of different approaches and perspectives suggested by the assimilation strategy. Remote Sensing Reviews 15, 283-303.

Foley, J.A., DeFries, R., Asner, G.P., Barford, C., Bonan, G., Carpenter, S.R., Chapin, F.S., Coe, M.T., Daily, G.C., Gibbs, H.K*., et al.*, 2005. Global Consequences of Land Use. Science 309, 570-574.

Foley, J.A., Ramankutty, N., Brauman, K.A., Cassidy, E.S., Gerber, J.S., Johnston, M., Mueller, N.D., O'Connell, C., Ray, D.K., West, P.C*., et al.*, 2011. Solutions for a cultivated planet. Nature 478, 337-342.

Forbes, J.C., Watson, R.D., 1992. Plants In Agriculture. Cambridge University Press.

Fox, A., Williams, M., Richardson, A.D., Cameron, D., Gove, J.H., Quaife, T., Ricciuto, D., Reichstein, M., Tomelleri, E., Trudinger, C.M*., et al.*, 2009. The REFLEX project: Comparing different algorithms and implementations for the inversion of a terrestrial ecosystem model against eddy covariance data. Agricultural and Forest Meteorology

149, 1597-1615.

Franch, B., Vermote, E.F., Becker-Reshef, I., Claverie, M., Huang, J., Zhang, J., Justice, C., Sobrino, J.A., 2015. Improving the timeliness of winter wheat production forecast in the United States of America, Ukraine and China using MODIS data and NCAR Growing Degree Day information. Remote Sensing of Environment 161, 131-148.

Fritz, S., Massart, M., Savin, I., Gallego, J., Rembold, F., 2008. The use of MODIS data to derive acreage estimations for larger fields: A case study in the south-western Rostov region of Russia. International Journal of Applied Earth Observation and Geoinformation 10, 453-466.

Fritz, S., See, L., McCallum, I., You, L., Bun, A., Moltchanova, E., Duerauer, M., Albrecht, F., Schill, C., Perger, C*., et al.*, 2015. Mapping global cropland and field size. Global Change Biology 21, 1980-1992.

Gelman, A., Rubin, D.B., 1992. Inference from Iterative Simulation Using Multiple Sequences. Statistical Science 7, 457-472.

GEOGLAM, 2015. About the GEOGLAM Initiative.

Godfray, H.C.J., Beddington, J.R., Crute, I.R., Haddad, L., Lawrence, D., Muir, J.F., Pretty, J., Robinson, S., Thomas, S.M., Toulmin, C., 2010. Food Security: The Challenge of Feeding 9 Billion People. Science 327, 812-818.

Gordon, L.J., Finlayson, C.M., Falkenmark, M., 2010. Managing water in agriculture for food production and other ecosystem services. Agricultural Water Management 97, 512-519.

Hansen, J.W., 2002. Realizing the potential benefits of climate prediction to agriculture: issues, approaches, challenges. Agricultural Systems 74, 309-330.

Hawkins, E., Osborne, T.M., Ho, C.K., Challinor, A.J., 2013. Calibration and bias correction of climate projections for crop modelling: An idealised case study over Europe. Agricultural and Forest Meteorology 170, 19-31.

Hedley, C., 2015. The role of precision agriculture for improved nutrient management on farms. Journal of the Science of Food and Agriculture 95, 12-19.

Hill, T.C., Quaife, T., Williams, M., 2011. A data assimilation method for using low-resolution Earth observation data in heterogeneous ecosystems. J. Geophys. Res. 116, D08117.

Hill, T.C., Ryan, E., Williams, M., 2012. The use of CO2 flux time series for parameter and carbon stock estimation in carbon cycle research. Global Change Biology 18, 179-193.

Hollinger, D.Y., Richardson, A.D., 2005. Uncertainty in eddy covariance measurements and its application to physiological models. Tree Physiology 25, 873-885.

Huang, J., Sedano, F., Huang, Y., Ma, H., Li, X., Liang, S., Tian, L., Zhang, X., Fan, J., Wu, W., 2016. Assimilating a synthetic Kalman filter leaf area index series into the WOFOST model to improve regional winter wheat yield estimation. Agricultural and Forest Meteorology 216, 188-202.

Huang, J., Tian, L., Liang, S., Ma, H., Becker-Reshef, I., Huang, Y., Su, W., Zhang, X., Zhu, D., Wu, W., 2015. Improving winter wheat yield estimation by assimilation of the leaf area index from Landsat TM and MODIS data into the WOFOST model. Agricultural and Forest Meteorology 204, 106-121.

Ines, A.V.M., Das, N.N., Hansen, J.W., Njoku, E.G., 2013. Assimilation of remotely sensed soil moisture and vegetation with a crop simulation model for maize yield prediction. Remote Sensing of Environment 138, 149-164.

Inoue, Y., Kurosu, T., Maeno, H., Uratsuka, S., Kozu, T., Dabrowska-Zielinska, K., Qi, J., 2002. Season-long daily measurements of multifrequency (Ka, Ku, X, C, and L) and full-polarization backscatter signatures over paddy rice field and their relationship with biological variables. Remote Sensing of Environment 81, 194-204.

IPCC, 2007. Contribution of Working Group III to the Fourth Assessment Report of the Intergovernmental Panel on Climate Change, 2007. In: B. Metz, O.R.D., P.R. Bosch, R. Dave, L.A. Meyer (Ed.), IPCC Fourth Assessment Report: Climate Change 2007, Cambridge, United Kingdom and New York, NY, USA.

Jiao, X., McNairn, H., Shang, J., Liu, J., 2010. The Sensitivity of multi-frequency (X, C and L-band) Radar backscatter signatures to bio-physical variables (LAI) over corn and soybean fields. In: Wagner W., Székely, B. (eds.), ISPRS TC VII Symposium - 100 Years ISPRS, Vienna, Austria, July 5-7, 2010, IAPRS, XXXVIII.

Johnson, J.A., Runge, C.F., Senauer, B., Foley, J., Polasky, S., 2014. Global agriculture and carbon trade-offs. Proceedings of the National Academy of Sciences 111, 12342-12347.

Jones, H.G., 1992. Plants and Microclimate. Cambridge University Press, Cambridge.

Jones, J.W., Hoogenboom, G., Porter, C.H., Boote, K.J., Batchelor, W.D., Hunt, L.A., Wilkens, P.W., Singh, U., Gijsman, A.J., Ritchie, J.T., 2003. The DSSAT cropping system model. European Journal of Agronomy 18, 235-265.

Justice, C.O., Becker-Reshef, I., 2007. Report from the workshop on developing a strategy for global agricultural monitoring in the framework of Group on Earth Observations (GEO). UN FAO.

Kalubarme, M.H., Potdar, M.B., Manjunath, K.R., Mahey, R.K., Siddhu, S.S., 2003. Growth profile based crop yield models: A case study of large area wheat yield modelling and its extendibility using atmospheric corrected NOAA AVHRR data. International Journal of Remote Sensing 24, 2037-2054.

Kerr, Y.H., Waldteufel, P., Richaume, P., Wigneron, J.P., Ferrazzoli, P., Mahmoodi, A., Al Bitar, A., Cabot, F., Gruhier, C., Juglea, S.E.*, et al.*, 2012. The SMOS Soil Moisture Retrieval Algorithm. Geoscience and Remote Sensing, IEEE Transactions on 50, 1384-1403.

Knorr, W., Heimann, M., 2001. Uncertainties in global terrestrial biosphere modeling: 1. A comprehensive sensitivity analysis with a new photosynthesis and energy balance scheme. Global Biogeochemical Cycles 15, 207-225.

Knyazikhin, Y., Martonchik, J.V., Myneni, R.B., Diner, D.J., Running, S.W., 1998. Synergistic algorithm for estimating vegetation canopy leaf area index and fraction of absorbed photosynthetically active radiation from MODIS and MISR data. Journal of Geophysical Research: Atmospheres 103, 32257-32275.

Koetz, B., Baret, F., Poilvé, H., Hill, J., 2005. Use of coupled canopy structure dynamic and radiative transfer models to estimate biophysical canopy characteristics. Remote Sensing of Environment 95, 115-124.

Kogan, F., Kussul, N., Adamenko, T., Skakun, S., Kravchenko, O., Kryvobok, O., Shelestov, A., Kolotii, A., Kussul, O., Lavrenyuk, A., 2013. Winter wheat yield forecasting in Ukraine based on Earth observation, meteorological data and biophysical models. International Journal of Applied Earth Observation and Geoinformation 23, 192-203.

Krinner, G., Viovy, N., de Noblet-Ducoudré, N., Ogée, J., Polcher, J., Friedlingstein, P., Ciais, P., Sitch, S., Prentice, I.C., 2005. A dynamic global vegetation model for studies of the coupled atmosphere-biosphere system. Global Biogeochemical Cycles 19, GB1015.

Kuppel, S., Peylin, P., Chevallier, F., Bacour, C., Maignan, F., Richardson, A.D., 2012. Constraining a global ecosystem model with multi-site eddy-covariance data.

Biogeosciences Discussions 9, 3317-3380.

Launay, M., Guerif, M., 2005. Assimilating remote sensing data into a crop model to improve predictive performance for spatial applications. Agriculture, Ecosystems & Environment 111, 321-339.

Laur, H., Bally, P., Meadows, P., Sánchez, J., Schättler, B., Lopinto, E., Esteban, D., 2004. ERS SAR Calibration: Derivation of σ^o in ESA ERS SAR PRI Products. In: ESA/ESRIN (Ed.).

Li, Y., Zhou, Q., Zhou, J., Zhang, G., Chen, C., Wang, J., 2014. Assimilating remote sensing information into a coupled hydrology-crop growth model to estimate regional maize yield in arid regions. Ecological Modelling 291, 15-27.

Lillesand, T., Kiefer, R.W., Chipman, J., 2008. Remote Sensing and Image Interpretation. John Wiley & Sons.

Lobell, D.B., 2013. Errors in climate datasets and their effects on statistical crop models. Agricultural and Forest Meteorology 170, 58-66.

Lobell, D.B., Burke, M.B., 2010. On the use of statistical models to predict crop yield responses to climate change. Agricultural and Forest Meteorology 150, 1443-1452.

Lobell, D.B., Thau, D., Seifert, C., Engle, E., Little, B., 2015. A scalable satellite-based crop yield mapper. Remote Sensing of Environment.

Lokupitiya, E., Denning, S., Paustian, K., Baker, I., Schaefer, K., Verma, S., Meyers, T., Bernacchi, C.J., Suyker, A., Fischer, M., 2009. Incorporation of crop phenology in Simple Biosphere Model (SiBcrop) to improve land-atmosphere carbon exchanges from croplands. Biogeosciences Discuss. 6, 17.

López-Lozano, R., Duveiller, G., Seguini, L., Meroni, M., García-Condado, S., Hooker, J., Leo, O., Baruth, B., 2015. Towards regional grain yield forecasting with 1 km-resolution EO biophysical products: Strengths and limitations at pan-European level. Agricultural and Forest Meteorology 206, 12-32.

Löw, F., Michel, U., Dech, S., Conrad, C., 2013. Impact of feature selection on the accuracy and spatial uncertainty of per-field crop classification using Support Vector Machines. ISPRS Journal of Photogrammetry and Remote Sensing 85, 102-119.

Lu, D., Mausel, P., Brondizio, E., Moran, E., 2002. Assessment of atmospheric correction methods for Landsat TM data applicable to Amazon basin LBA research. International Journal of Remote Sensing 23, 2651-2671.

Luo, Y., Keenan, T.F., Smith, M., 2015. Predictability of the terrestrial carbon cycle. Global Change Biology 21, 1737-1751.

Ma, H., Huang, J., Zhu, D., Liu, J., Su, W., Zhang, C., Fan, J., 2013. Estimating regional winter wheat yield by assimilation of time series of HJ-1 CCD NDVI into WOFOST–ACRM model with Ensemble Kalman Filter. Mathematical and Computer Modelling 58, 759-770.

MacBean, N., Peylin, P., 2014. Biogeochemistry: Agriculture and the global carbon cycle. Nature 515, 351-352.

Macelloni, G., Paloscia, S., Pampaloni, P., Marliani, F., Gai, M., 2001. The relationship between the backscattering coefficient and the biomass of narrow and broad leaf crops. Geoscience and Remote Sensing, IEEE Transactions on 39, 873-884.

Mahey, R.K., Singh, R., Sidhu, S.S., Narang, R.S., Dadhwal, V.K., Parihar, J.S., Sharma, A.K., 1993. Pre-harvest state level wheat acreage estimation using IRS-IA LISS-I data in Punjab (India). International Journal of Remote Sensing 14, 1099-1106.

Maini, A.K., Agrawal, V., 2014. Satellite Technology: Principles and Applications. Wiley-Blackwell, West Sussex.

Malmstrom, C.M., Thompson, M.V., Juday, G.P., Los, S.O., Randerson, J.T., Field, C.B., 1997. Interannual variation in global-scale net primary production: Testing model estimates.

Martimor, P., Arino, O., Berger, M., Biasutti, R., Carnicero, B., Del Bello, U., Fernandez, V., Gascon, F., Silvestrin, P., Spoto, F*., et al.*, 2007. Sentinel-2 optical high resolution mission for GMES operational services. Geoscience and Remote Sensing Symposium, 2007. IGARSS 2007. IEEE International, pp. 2677-2680.

Martre, P., Wallach, D., Asseng, S., Ewert, F., Jones, J.W., Rötter, R.P., Boote, K.J., Ruane, A.C., Thorburn, P.J., Cammarano, D*., et al.*, 2015. Multimodel ensembles of wheat growth: many models are better than one. Global Change Biology 21, 911-925.

McNairn, H., Brisco, B., 2004. The application of C-band polarimetric SAR for agriculture: a review. Canadian Journal of Remote Sensing 30, 525-542.

McNairn, H., Champagne, C., Shang, J., Holmstrom, D. and Reichert, G., 2008. Integration of optical and Synthetic Aperture Radar (SAR) imagery for delivering operational annual crop inventories. ISPRS Journal of Photogrammetry and Remote Sensing 64, 434-449.

McNairn, H., Decker, V., Murnaghan, K., 2002. The sensitivity of C-band polarimetric SAR to crop condition. *Geoscience and Remote Sensing Symposium, 2002. IGARSS '02. 2002 IEEE International 3*, 1471 - 1473.

McNairn, H., Shang, J., Champagne, C., Jiao, X., 2009. TerraSAR-X and RADARSAT-2 for crop classification and acreage estimation. Geoscience and Remote Sensing Symposium,2009 IEEE International,IGARSS 2009, pp. II-898-II-901.

MEA, 2005. Ecosystems and human well-being Island Press, Washington, D.C., USA

Mkhabela, M.S., Bullock, P., Raj, S., Wang, S., Yang, Y., 2011. Crop yield forecasting on the Canadian Prairies using MODIS NDVI data. Agricultural and Forest Meteorology 151, 385-393.

Monje, O., Bugbee, B., 1998. Adaptation to high CO2 concentration in an optimal environment: radiation capture, canopy quantum yield and carbon use efficiency. Plant, Cell & Environment 21, 315-324.

Monteith, J.L., Unsworth, M.H., 1990. Principles of environmental physics. E. Arnold, London and New York.

Moran, M.S., Inoue, Y., Barnes, E.M., 1997. Opportunities and limitations for image-based remote sensing in precision crop management. Remote Sensing of Environment 61, 319-346.

Moulin, S., Bondeau, A., Delecolle, R., 1998. Combining agricultural crop models and satellite observations: From field to regional scales. International Journal of Remote Sensing 19, 1021-1036.

Mulla, D.J., 2013. Twenty five years of remote sensing in precision agriculture: Key advances and remaining knowledge gaps. Biosystems Engineering 114, 358-371.

Newlands, N.K., Espino-Hernández, G., Erickson, R.S., 2012. Understanding Crop Response to Climate Variability with Complex Agroecosystem Models. International Journal of Ecology 2012.

NRC, 2014. Temporal Resolution. Natural Resources Canada (NRC), Canadian Government.

Osborne, B., Saunders, M., Walmsley, D., Jones, M., Smith, P., 2010. Key questions and uncertainties associated with the assessment of the cropland greenhouse gas balance. Agriculture, Ecosystems & Environment 139, 293-301.

Osborne, T., Rose, G., Wheeler, T., 2013. Variation in the global-scale impacts of climate change on crop productivity due to climate model uncertainty and adaptation. Agricultural and Forest Meteorology 170, 183-194.

Osborne, T.M., Wheeler, T.R., 2013. Evidence for a climate signal in trends of global crop yield variability over the past 50 years. Environ. Res. Lett. 8.

Paloscia, S., 2002. A summary of experimental results to assess the contribution of SAR for mapping vegetation biomass and soil moisture. Canadian Journal of Remote Sensing 28, 246-261.

Penning de Vries, F.W.T., Jansen, D.M., ten Berge, H.F.M., Bakema, A.H., 1989. Simulation of ecophysiological processes in several annual crops. Simulation Monographs, Pudoc, Wageningen, Netherlands.

Pittman, K., Hansen, M.C., Becker-Reshef, I., Potapov, P.V., Justice, C.O., 2010. Estimating Global Cropland Extent with Multi-year MODIS Data. Remote Sensing 2, 1844.

Porter, Semenov, M.A., 2005. Crop responses to climatic variation. Philos. Trans. R. Soc. B Biol. Sci. 360, 14.

Power, A.G., 2010. Ecosystem services and agriculture: tradeoffs and synergies. Philosophical Transactions of the Royal Society B: Biological Sciences 365, 2959-2971.

Quaife, T., Lewis, P., De Kauwe, M., Williams, M., Law, B.E., Disney, M., Bowyer, P., 2008. Assimilating canopy reflectance data into an ecosystem model with an Ensemble Kalman Filter. Remote Sensing of Environment 112, 1347-1364.

Rafique, R., Kumar, S., Luo, Y., Kiely, G., Asrar, G., 2015. An algorithmic calibration approach to identify globally optimal parameters for constraining the DayCent model.

Ecological Modelling 297, 196-200.

Ramankutty, N., Evan, A.T., Monfreda, C., Foley, J.A., 2008. Farming the planet: 1. Geographic distribution of global agricultural lands in the year 2000. Global Biogeochemical Cycles 22, n/a-n/a.

Reichstein, M., Bahn, M., Ciais, P., Frank, D., Mahecha, M.D., Seneviratne, S.I., Zscheischler, J., Beer, C., Buchmann, N., Frank, D.C*., et al.*, 2013. Climate extremes and the carbon cycle. Nature 500, 287-295.

Reichstein, M., Falge, E., Baldocchi, D., Papale, D., Aubinet, M., Berbigier, P., Bernhofer, C., Buchmann, N., Gilmanov, T., Granier, A*., et al.*, 2005. On the separation of net ecosystem exchange into assimilation and ecosystem respiration: review and improved algorithm. Global Change Biology 11, 1424-1439.

Rembold, F., Meroni, M., Urbano, F., Royer, A., Atzberger, C., Lemoine, G., Eerens, H., Haesen, D., 2015. Remote sensing time series analysis for crop monitoring with the SPIRITS software: new functionalities and use examples. Frontiers in Environmental Science 3.

Revill, A., Bloom, A.A., Williams, M., 2016. Impacts of reduced model complexity and driver resolution on cropland ecosystem photosynthesis estimates. Field Crops Research 187, 74-86.

Revill, A., Sus, O., Barrett, B., Williams, M., 2013. Carbon cycling of European croplands: A framework for the assimilation of optical and microwave Earth observation data. Remote Sensing of Environment 137, 84-93.

Roberts, J.S., 2010. Dew Point Temperature. Encyclopedia of Agricultural, Food, and Biological Engineering, Second Edition. Taylor & Francis, pp. 286-291.

Robertson, P.G., Gross, K.L., Hamilton, S.K., Landis, D.A., Schmidt, T.M., Snapp, S.S., Swinton, S.M., 2014. Farming for Ecosystem Services: An Ecological Approach to Production Agriculture. BioScience.

Rossow, W.B., Schiffer, R.A., 1999. Advances in Understanding Clouds from ISCCP. Bulletin of the American Meteorological Society 80, 2261-2287.

Rötter, R.P., Palosuo, T., Kersebaum, K.C., Angulo, C., Bindi, M., Ewert, F., Ferrise, R., Hlavinka, P., Moriondo, M., Nendel, C*., et al.*, 2012. Simulation of spring barley yield in different climatic zones of Northern and Central Europe: A comparison of nine crop models. Field Crops Research 133, 23-36.

Sacks, W.J., Deryng, D., Foley, J.A., Ramankutty, N., 2010. Crop planting dates: an analysis of global patterns. Global Ecology and Biogeography 19, 607-620.

Savitzky, A., Golay, M.J.E., 1964. Smoothing and Differentiation of Data by Simplified Least Squares Procedures. Analytical Chemistry 36, 1627-1639.

Schmid, H.P., 1994. Source areas for scalars and scalar fluxes. Boundary-Layer Meteorology 67, 293-318.

Shang, J., McNairn, H., Champagne, C., Jiao, X., 2009. Application of Multi-Frequency Synthetic Aperture Radar (SAR) in Crop Classification. In: Jedlovec, G. (Ed.), *Advances in Geoscience and Remote Sensing*, Canada, pp. 557 - 567.

Sheffield, J., Goteti, G., Wood, E.F., 2006. Development of a 50-Year High-Resolution Global Dataset of Meteorological Forcings for Land Surface Modeling. Journal of Climate 19, 3088-3111.

Singh, A.K., Tripathy, R., Chopra, U.K., 2008. Evaluation of CERES-Wheat and CropSyst models for water–nitrogen interactions in wheat crop. Agricultural Water Management 95, 776-786.

Smith, J., Lin, T.L., Ranson, K., 1980. The Lambertian assumption and Landsat data.

Photogrammetric Engineering and Remote Sensing 46, 1183-1189.

Smith, M.J., Purves, D.W., Vanderwel, M.C., Lyutsarev, V., Emmott, S., 2013. The climate dependence of the terrestrial carbon cycle, including parameter and structural uncertainties. Biogeosciences 10, 583-606.

Smith, P., Bustamante, M., Ahammad, H., Clark, H., Dong, H., Elsiddig, E.A., Haberl, H., Harper, R., House, J., Jafari, M*., et al.*, 2014. Agriculture, Forestry and Other Land Use (AFOLU). In: Edenhofer, O., R. Pichs-Madruga, Y. Sokona, E. Farahani, S. Kadner, K. Seyboth, A. Adler, I. Baum, S. Brunner, P. Eickemeier, B. Kriemann, J. Savolainen, S. Schlömer, C. von Stechow, T. Zwickel and J.C. Minx (Ed.), Climate Change 2014: Mitigation of Climate Change. Contribution of Working Group III to the Fifth Assessment Report of the Intergovernmental Panel on Climate Change. Cambridge University Press, Cambridge, United Kingdom and New York, NY, USA.

Smith, P., Lanigan, G., Kutsch, W.L., Buchmann, N., Eugster, W., Aubinet, M., Ceschia, E., Béziat, P., Yeluripati, J.B., Osborne, B*., et al.*, 2010. Measurements necessary for assessing the net ecosystem carbon budget of croplands. Agriculture, Ecosystems & Environment 139, 302-315.

Smith, P., Martino, Z., Gwary, H.J., Kumar, P., McCarl, B., Ogle, S., O'Mara, F., Rice, C., Scholes, B., Sirotenko, O., 2007. Contribution of Working Group III to the Fourth Assessment Report of the Intergovernmental Panel on Climate Change, 2007. In: B. Metz, O.R.D., P.R. Bosch, R. Dave, L.A. Meyer (Ed.), IPCC Fourth Assessment Report: Climate Change 2007, Cambridge, United Kingdom and New York, NY, USA.

Smith, R., Adams, J., Stephens, D., Hick, P., 1995. Forecasting wheat yield in a Mediterranean-type environment from the NOAA satellite. Australian Journal of Agricultural Research 46, 113-125.

Soares, J., Williams, M., Jarvis, I., Bingfang, W., Leo, O., Fabre, P., Huynh, F., Kosuth, P., Lepoutre, D., Parihar, J.S*., et al.*, 2011. Strengthening Global Agricultural Monitoring, Improving Sustainable Data for Worldwide Food Security & Commodity Market Transparency. Proposal "The G20 Global Agricultural Monitoring" initiative.

Spadavecchia, L., Williams, M., Law, B.E., 2011. Uncertainty in predictions of forest carbon dynamics: separating driver error from model error. Ecological Applications 21, 1506-1522.

Streck, N., Weiss, A., Xue, Q., Stephen Baenziger, P., 2003a. Improving predictions of developmental stages in winter wheat: a modified Wang and Engel model. Agricultural and Forest Meteorology 115, 139-150.

Streck, N.A., Weiss, A., Baenziger, P.S., 2003b. A Generalized Vernalization Response Function for Winter Wheat. Agronomy Journal 95, 155-159.

Sus, O., Heuer, M.W., Meyers, T.P., Williams, M., 2012. A data assimilation framework for constraining upscaled cropland carbon flux seasonality and biometry with MODIS. Biogeosciences Discuss. 9, 11139-11177.

Sus, O., Heuer, M.W., Meyers, T.P., Williams, M., 2013. A data assimilation framework for constraining upscaled cropland carbon flux seasonality and biometry with MODIS. Biogeosciences 10, 2451-2466.

Sus, O., Williams, M., Bernhofer, C., Beziat, P., Buchmann, N., Ceschia, E., Doherty, R., Eugster, W., Grunwald, T., Kutsch, W*., et al.*, 2010. A linked carbon cycle and crop developmental model: Description and evaluation against measurements of carbon fluxes and carbon stocks at several European agricultural sites. Agriculture, ecosystems and environment. 139, 402-418.

Sylvester-Bradley, R., Berry, P., Blake, J., Kindred, D., Spink, J., Bingham, I., McVittie, J., Foulkes, J., 2008. The Wheat Growth Guide. Agriculture and Horticulture Development Board (AHDB), London, p. 32.

Tang, J., Zhuang, Q., 2009. A global sensitivity analysis and Bayesian inference framework for improving the parameter estimation and prediction of a process-based Terrestrial Ecosystem Model. Journal of Geophysical Research: Atmospheres 114, D15303.

Thorp, K.R., DeJonge, K.C., Kaleita, A.L., Batchelor, W.D., Paz, J.O., 2008. Methodology for the use of DSSAT models for precision agriculture decision support. Computers and Electronics in Agriculture 64, 276-285.

Tilman, D., Balzer, C., Hill, J., Befort, B.L., 2011. Global food demand and the sustainable intensification of agriculture. Proceedings of the National Academy of Sciences 108, 20260-20264.

Tilman, D., Fargione, J., Wolff, B., D'Antonio, C., Dobson, A., Howarth, R., Schindler, D., Schlesinger, W.H., Simberloff, D., Swackhamer, D., 2001. Forecasting Agriculturally Driven Global Environmental Change. Science 292, 281-284.

Torres, R., Snoeij, P., Geudtner, D., Bibby, D., Davidson, M., Attema, E., Potin, P., Rommen, B., Floury, N., Brown, M., *et al.*, 2012. GMES Sentinel-1 mission. Remote Sensing of Environment 120, 9-24.

Tubiello, F.N., Soussana, J.-F., Howden, S.M., 2007. Crop and pasture response to climate change. Proceedings of the National Academy of Sciences 104, 19686-19690.

Tucker, C.J., Holben, B.N., Elgin, J.H., McMurtrey, J.E., 1980. Relationships of spectral data to grain-yield variations. Photogrammetric Engineering & Remote Sensing 46.

Ulaby, F.T., Allen, C.T., Eger Iii, G., Kanemasu, E., 1984. Relating the microwave backscattering coefficient to leaf area index. Remote Sensing of Environment 14, 113-133.

Valade, A., Vuichard, N., Ciais, P., Ruget, F., Viovy, N., Gabrielle, B., Huth, N., Martiné, J.-F., 2013. ORCHIDEE-STICS, a process-based model of sugarcane biomass production: calibration of model parameters governing phenology. GCB Bioenergy, n/a-n/a.

Verhoef, W., 1984. Light scattering by leaf layers with application to canopy reflectance modeling: The SAIL model. Remote Sensing of Environment 16, 125-141.

Verhoef, W., 1985. Earth observation modeling based on layer scattering matrices. Remote Sensing of Environment 17, 165-178.

Verrelst, J., Rivera, J.P., Veroustraete, F., Muñoz-Marí, J., Clevers, J.G.P.W., Camps-Valls, G., Moreno, J., 2015. Experimental Sentinel-2 LAI estimation using parametric, non-parametric and physical retrieval methods – A comparison. ISPRS Journal of Photogrammetry and Remote Sensing 108, 260-272.

Wang, E., Engel, T., 1998. Simulation of phenological development of wheat crops. Agricultural Systems 58, 1-24.

Wardlow, B.D., Egbert, S.L., Kastens, J.H., 2007. Analysis of time-series MODIS 250 m vegetation index data for crop classification in the U.S. Central Great Plains. Remote Sensing of Environment 108, 290-310.

Waring, R.H., Landsberg, J.J., Williams, M., 1998. Net primary production of forests: a constant fraction of gross primary production? Tree Physiology 18, 129-134.

Wattenbach, M., Sus, O., Vuichard, N., Lehuger, S., Gottschalk, P., Li, L., Leip, A., Williams, M., Tomelleri, E., Kutsch, W.L., *et al.*, 2010. The carbon balance of European croplands: A cross-site comparison of simulation models. Agriculture, Ecosystems & Environment 139, 419-453.

Wei, W., Wu, W., Li, Z., Yang, P., Zhou, Q., 2015. Selecting the Optimal NDVI Time-Series Reconstruction Technique for Crop Phenology Detection. Intelligent

Automation & Soft Computing, 1-11.

Whitcraft, A., Becker-Reshef, I., Justice, C., 2015a. A Framework for Defining Spatially Explicit Earth Observation Requirements for a Global Agricultural Monitoring Initiative (GEOGLAM). Remote Sensing 7, 1461-1481.

Whitcraft, A.K., Vermote, E.F., Becker-Reshef, I., Justice, C.O., 2015b. Cloud cover throughout the agricultural growing season: Impacts on passive optical earth observations. Remote Sensing of Environment 156, 438-447.

Williams, M., E.B Rastetter, D.N Fernandes, M.L. Goulden, G.R. Shaver, Johnson, L.C., 1997. Predicting gross primary productivity in terrestrial ecosystems. Ecological Applications 7, 882 - 894.

Williams, M., Law, B.E., Anthoni, P.M., Unsworth, M.H., 2001. Use of a Simulation Model and Ecosystem Flux Data to Examine Carbon-Water Interactions in Ponderosa Pine. Tree Physiology 21, 287-298.

Williams, M., Rastetter, E.B., Fernandes, D.N., Goulden, M.L., Wofsy, S.C., Shaver, G.R., Melillo, J.M., Munger, J.W., Fan, S.M., Nadelhoffer, K.J., 1996. Modelling the soil-plant-atmosphere continuum in a Quercus–Acer stand at Harvard Forest: the regulation of stomatal conductance by light, nitrogen and soil/plant hydraulic properties. Plant, Cell & Environment 19, 911-927.

Williams, M., Richardson, A.D., Reichstein, M., Stoy, P.C., Peylin, P., Verbeeck, H., Carvalhais, N., Jung, M., Hollinger, D.Y., Kattge, J., *et al.*, 2009. Improving land surface models with FLUXNET data. Biogeosciences 6, 1341-1359.

Williams, M., Schwarz, P.A., Law, B.E., Irvine, J., Kurpius, M.R., 2005. An improved analysis of forest carbon dynamics using data assimilation. Global Change Biology 11, 89-105.

Wong, M.T.F., Asseng, S., 2006. Determining the Causes of Spatial and Temporal Variability of Wheat Yields at Sub-field Scale Using a New Method of Upscaling a Crop Model. Plant and Soil 283, 203-215.

Wood, S., Sebastian, K and Scherr S.J., 2000. Pilot Analysis of Global Ecosystems: Agroecosystems Technical Report. World Resources Institute and International Food Policy Research Institute, Washington, DC.

Wu, S., Huang, J., Liu, X., Fan, J., Ma, G., Zou, J., Li, D., Chen, Y., 2012. Assimilating MODIS-LAI into Crop Growth Model with EnKF to Predict Regional Crop Yield Computer and Computing Technologies in Agriculture V. Springer Boston, pp. 410-418.

Wylie, D., Jackson, D.L., Menzel, W.P., Bates, J.J., 2005. Trends in Global Cloud Cover in Two Decades of HIRS Observations. Journal of Climate 18, 3021-3031.

Xiao, J., Zhuang, Q., Law, B.E., Baldocchi, D.D., Chen, J., Richardson, A.D., Melillo, J.M., Davis, K.J., Hollinger, D.Y., Wharton, S., *et al.*, 2011. Assessing net ecosystem carbon exchange of U.S. terrestrial ecosystems by integrating eddy covariance flux measurements and satellite observations. Agricultural and Forest Meteorology 151, 60-69.

Xie, Y., Sha, Z., Yu, M., 2008. Remote sensing imagery in vegetation mapping: a review. Journal of Plant Ecology 1, 9-23.

Xu, T., White, L., Hui, D., Luo, Y., 2006. Probabilistic inversion of a terrestrial ecosystem model: Analysis of uncertainty in parameter estimation and model prediction. Global Biogeochemical Cycles 20, GB2007.

Xu, W., Jiang, H., Huang, J., 2011. Regional Crop Yield Assessment by Combination of a Crop Growth Model and Phenology Information Derived from MODIS. Sensor Letters 9, 981-989.

Yang, W., Tan, B., Dong, H., Rautiainen, M., Shabanov, N.V., Wang, Y., Privette, J.L., Huemmrich, K.F., Fensholt, R., Sandholt, I*., et al.*, 2006. MODIS leaf area index products: from validation to algorithm improvement. Geoscience and Remote Sensing, IEEE Transactions on 44, 1885-1898.

Yao, F., Tang, Y., Wang, P., Zhang, J., 2015. Estimation of maize yield by using a process-based model and remote sensing data in the Northeast China Plain. Physics and Chemistry of the Earth, Parts A/B/C 87–88, 142-152.

Yuping, M., Shili, W., Li, Z., Yingyu, H., Liwei, Z., Yanbo, H., Futang, W., 2008. Monitoring winter wheat growth in North China by combining a crop model and remote sensing data. International Journal of Applied Earth Observation and Geoinformation 10, 426-437.

Zhang, W., Ricketts, T.H., Kremen, C., Carney, K., Swinton, S.M., 2007. Ecosystem services and dis-services to agriculture. Ecological Economics 64, 253-260.

Zhang, X., Izaurralde, R.C., Manowitz, D.H., Sahajpal, R., West, T.O., Thomson, A.M., Xu, M., Zhao, K., LeDuc, S.D., Williams, J.R., 2015. Regional scale cropland carbon budgets: Evaluating a geospatial agricultural modeling system using inventory data. Environmental Modelling & Software 63, 199-216.

Zhao, Y., Chen, S., Shen, S., 2013. Assimilating remote sensing information with crop model using Ensemble Kalman Filter for improving LAI monitoring and yield estimation. Ecological Modelling 270, 30-42.

Zheng, H., Li, Y., Chen, J.M., Wang, T., Huang, Q., Huang, W.X., Li, S.M., Yuan, W.P., Zheng, X., Zhang, S.P*., et al.*, 2014. A global carbon assimilation system based on a dual optimization method. Biogeosciences Discuss. 11, 14269-14317.

Zhengwei, Y., Liping, D., Genong, Y., Zeqiang, C., 2011. Vegetation condition indices for crop vegetation condition monitoring. Geoscience and Remote Sensing Symposium (IGARSS), 2011 IEEE International, pp. 3534-3537.

Zhu, Z., Woodcock, C.E., 2012. Object-based cloud and cloud shadow detection in Landsat imagery. Remote Sensing of Environment 118, 83-94.

Ziehn, T., Scholze, M., Knorr, W., 2012. On the capability of Monte Carlo and adjoint inversion techniques to derive posterior parameter uncertainties in terrestrial ecosystem models. Global Biogeochemical Cycles 26, GB3025.

APPENDIX A

A1. SPAc model winter wheat parameters

Table A.1: List of SPAc model parameters, including units, nominal values and corresponding cited sources, that are used to simulate winter wheat crop growth and development (adapted from: Sus *et al.*, 2010).

Parameter symbol	**Name**	**Unit**	**Nominal value**	**Source**
Nfrac	Fraction of leaf nitrogen content per unit area on cumulative leaf area for four canopy layers (from top to bottom).	Fraction	0.33 (layer 1), 0.27 (layer 2), 0.22 (layer 3), 0.18 (layer 4).	Hirose and Werger (1987)
gplant	Stem conductance	mmol m^{-2} s^{-1} MPa^{-1}	5	Adjusted to match leaf specific conductance from Liu *et al.* (2005)
Ψ_1	Minimum leaf water potential	MPa	−1.9	Johnson *et al.* (1987)
I	Stomatal efficiency	–	1.007	Adjusted to maintain max. gs <400 mmol m^{-2} s^{-1} (Ye and Yu, 2008)
C	Leaf capacitance	mmol m^{-2} MPa^{-1}	2000	Estimated (Williams *et al.*, 1996)
Rr	Root resistivity	MPa s g $mmol^{-1}$	10	Adjusted to match leaf specific conductance from Liu *et al.* (2005)
Vcmax	Maximum carboxylation capacity	μmol m^{-2} s^{-1}	64	Wullschleger (1993), Tambussi *et al.* (2005)
Jmax	Maximum electron transport rate	μmol m^{-2} s^{-1}	137	Wullschleger (1993), Tambussi *et al.* (2005)
Cla	Carbon per leaf area	gC m^{-2}	19.5	Penning de Vries *et al.* (1989)
rdc	Decomposition rate	h^{-1}	2.3×10^{-5}	Buyanovsky and Wagner (1987)

fa	Fraction of GPP respired	Fraction	0.44	Monje and Bugbee (1998)
troot	Turnover rate of roots	h^{-1}	6.25×10^{-3}	Penning de Vries *et al.* (1989)
mlit	Mineralization rate of litter	h^{-1}	2.8×10^{-4}	Buyanovsky and Wagner (1987)
mSOM	Mineralisation rate of SOM/CWD	h^{-1}	2.28×10^{-6}	Buyanovsky and Wagner (1987)
tlab	Turnover rate of labile pool	h^{-1}	6.25×10^{-3}	Penning de Vries *et al.* (1989)
rtr	Respiratory cost of labile transfers	Fraction	0.2133	Goudriaan and Van Laar (1994)
tar	Turnover rate of autotrophic respiration pool	h^{-1}	0.07	Adjusted to give ~daily turnover of pool
GDDem	Temperature sum at emergence	Degree days	125	Wang and Engel (1998)
trlstem	Rate of translocation of remobilisable carbon from stems	h^{-1}	8.3×10^{-3}	Penning de Vries *et al.* (1989)
rmax,v	Maximum development rate in vegetative phase	d^{-1}	0.04	Yan and Wallace (1998), Li *et al.* (2008)
rmax,r	Maximum development rate in reproductive phase	d^{-1}	0.035	Streck *et al.* (2003)
Tmin	Minimum temperature for development	°C	0	Li *et al.* (2008)
Topt	Optimum temperature for development	°C	24	Li *et al.* (2008)
Tmax	Maximum temperature for development	°C	35	Li *et al.* (2008)
Tmin,vn	Minimum temperature for vernalization	°C	−1.3	Porter and Gawith (1999)
Topt,vn	Optimum temperature for vernalization	°C	4.9	Porter and Gawith (1999)
Tmax,vn	Maximum temperature for vernalization	°C	15.7	Porter and Gawith (1999)
VDh	Effective vernalization days when plants are 50% vernalized	VD	22.5	Streck *et al.* (2003)
LAIcr	Critical leaf area index beyond which leaf senescence due to self-shading occurs	$m^2\ m^{-2}$	4	Van Laar *et al.* (1997)
dshmax	Maximum value of relative death rate due to shading	h^{-1}	1.25×10^{-3}	Van Laar *et al.* (1997)

PHcr	Minimum (or critical) photoperiod for development	h	8.25	Streck *et al.* (2003)
PHsc	Photoperiod sensitivity coefficient	–	0.25	Streck *et al.* (2003)

References

Buyanovsky, G.A., Wagner, G.H., 1987. Carbon transfer in a winter wheat (Triticum aestivum) ecosystem. Biol Fert Soils 5, 76-82.

Goudriaan, J., Laar, H.H.v., 1994. Modelling potential crop growth processes : textbook with exercises. Kluwer Academic Publishers, Dordrecht.

Hirose, T., Werger, M.J.A., 1987. Maximizing daily canopy photosynthesis with respect to the leaf nitrogen allocation pattern in the canopy. Oecologia 72, 520-526.

Johnson, R.C., Mornhinweg, D.W., Ferris, D.M., Heitholt, J.J., 1987. Leaf Photosynthesis and Conductance of Selected Triticum Species at Different Water Potentials. Plant Physiology 83, 1014-1017.

Li, L., McMaster, G.S., Yu, Q., Du, J., 2008. Simulating winter wheat development response to temperature: Modifying Malo's exponential sine equation. Computers and Electronics in Agriculture 63, 274-281.

Liu, L., Kon, H., Matsuoka, N., Kobayashi, T., 2005. Coordination between Stomatal Conductance and Leaf-specific Hydraulic Conductance in Maize (<i>Zea mays</i> L.). Journal of Agricultural Meteorology 61, 143-152.

Monje, O., Bugbee, B., 1998. Adaptation to high CO2 concentration in an optimal environment: radiation capture, canopy quantum yield and carbon use efficiency. Plant, Cell & Environment 21, 315-324.

Penning de Vries, F.W.T., Jansen, D.M., ten Berge, H.F.M., Bakema, A.H., 1989. Simulation of ecophysiological processes in several annual crops. Simulation Monographs, Pudoc, Wageningen, Netherlands.

Porter, J.R., Gawith, M., 1999. Temperatures and the growth and development of wheat: a review. European Journal of Agronomy 10, 23-36.

Streck, N., Weiss, A., Xue, Q., Stephen Baenziger, P., 2003. Improving predictions of developmental stages in winter wheat: a modified Wang and Engel model. Agricultural and Forest Meteorology 115, 139-150.

Sus, O., Williams, M., Bernhofer, C., Beziat, P., Buchmann, N., Ceschia, E., Doherty, R., Eugster, W., Grunwald, T., Kutsch, W., *et al.*, 2010. A linked carbon cycle and crop developmental model: Description and evaluation against measurements of carbon fluxes and carbon stocks at several European agricultural sites. Agriculture, ecosystems and environment. 139, 402-418.

Tambussi, E.A., Nogués, S., Ferrio, P., Voltas, J., Araus, J.L., 2005. Does higher yield potential improve barley performance in Mediterranean conditions?: A case study. Field Crops Research 91, 149-160.

Van Laar, H.H., Goudriaan, J., van Keulen, H., 1997. SUCROS97: simulation of crop growth for potential and water-limited production situations. Quantitative Approaches in Systems Analysis. Wageningen.

Wang, E., Engel, T., 1998. Simulation of phenological development of wheat crops. Agricultural Systems 58, 1-24.

Williams, M., Rastetter, E.B., Fernandes, D.N., Goulden, M.L., Wofsy, S.C., Shaver, G.R., Melillo, J.M., Munger, J.W., Fan, S.M., Nadelhoffer, K.J., 1996. Modelling the soil-plant-atmosphere continuum in a Quercus–Acer stand at Harvard Forest: the regulation of stomatal conductance by light, nitrogen and soil/plant hydraulic properties. Plant, Cell & Environment 19, 911-927.

Wullschleger, S., D., 1993. Biochemical Limitations to Carbon Assimilation in C3 Plants—A Retrospective Analysis of the A/Ci Curves from 109 Species. Journal of Experimental Botany 44, 907-920.

Yan, W., Wallace, D., H., 1998. Simulation and Prediction of Plant Phenology for Five Crops Based on Photoperiod×Temperature Interaction. Annals of Botany 81, 705-716.

Ye, Z.P., Yu, Q., 2008. A coupled model of stomatal conductance and photosynthesis for winter wheat. Photosynthetica 46, 637-640.

APPENDIX B

B1. Aggregated Canopy Model (ACM) variables

Table B.1: List of fixed variables used in the ACM aggregation equations (see Appendix B2).

Variable	Value used	Source
Average foliar nitrogen (g m^{-2})	1.0	Estimated from Sus *et al.* (2010)
Atmopheric CO_2 (ppm)	393	FLUXNET database (fluxnet.ornl.gov)
Minimum leaf water potential (MPa)	2.0	Johnson *et al.* (1987)
Soil water potential (MPa)	0.	Williams *et al.* (1997)
Soil-plant hydraulic resistance (fraction of total conductance)	0.2	Estimated from Williams *et al.* (2001)

B2. ACM derivation and equations

Using the 10 scalar coefficients and fixed variables (listed in Table 3.1 of Chapter 3 and Appendix Table B.1, respectively), ACM consists of aggregation equations, which are solved in sequence, in order to fit daily photosynthesis estimated by the fine-scale model. From Williams *et al.* (1997), the first governing equation assumes a linear relationship between GPP and total canopy nitrogen, which is estimated from the average foliar nitrogen (N) and leaf area index (LAI), also including the impacts of temperature on the metabolic processes:

$$p_{\mathrm{N}} = a_1 NLAI\ e^{-a_8 T} \qquad \text{Equation B.1}$$

where p_{N} is the total canopy nitrogen-limited photosynthetic capacity (g m^{-2}), T is the average daily temperature (°C, determined from the daily minimum and maximum temperatures), a_1 and a_8 are the Nitrogen use efficiency and Temperature calibration coefficients, respectively.

The fine-scale model, of which ACM is designed to emulate, simulates stomatal conductance that is responsive to atmospheric vapour pressure deficit, which in turn is related to temperature and temperature range. Therefore, ACM calculates the daily canopy conductance (g_c), which determines the rate of carbon (C) fixation, as a function of daily temperature range (T_d) and the soil-canopy water potential gradient (ψ_d, MPa, the difference between the minimum leaf water potential and soil water potential) balanced by the total soil-plant hydraulic resistance (R_{tot}):

$$g_{\mathrm{c}} = \frac{-\psi_d \ e^{-a_{10}}}{a_6 R_{tot} + T_d} \qquad \text{Equation B.1}$$

where a_{10} and a_6 are the water potential and hydraulic scalar coefficients, respectively.

Using the p_N and g_c values, the internal CO2 concentration (C_i) was then determined as a function of ambient atmospheric CO2 (C_a):

$$C_{\mathrm{i}} = \frac{1}{2}\left[C_a + q - p + \sqrt{(C_a + q - p)^2 - 4(C_a q - p\theta)}\right] \qquad \text{Equation B.2}$$

where $q = \theta - k$ and $p = p_N/g_c$. The rate of diffusion of atmospheric CO2 to the point of C fixation (p_D) is calculated as a function of g_c and the difference between C_a and C_i:

$$p_{\mathrm{D}} = g_{\mathrm{c}}\,(C_a - C_{\mathrm{i}}) \qquad \text{Equation B.3}$$

Since the diffusive constraints vary with irradiance (I), a two-step calculation was applied in order to calculate the light limitation. First, the canopy-level quantum yield (E_0) that was calculated based on LAI:

$$E_0 = \frac{a_7\, LAI^2}{a_9 + LAI^2}$$ Equation B.4

where a_7 and a_9 are the maxium canopy quantum yield and LAI-canopy quantum yield coefficients, respectively. The light limitation (p_{I}) is then calculated as:

$$p_I = \frac{E_0\, I p_D}{E_0 I + p_D}$$ Equation B.5

The final calculation of daily GPP (p_{T}) is then made, which is a function of p_{I}:

$$p_{\mathrm{T}} = p_1\,(a_5 D_{\mathrm{ms}} + a_2)$$ Equation B.6

where D_{ms} is the number of days (absolute) from the summer solstice (22 June/Julian day 173 in the Northern Hemisphere), a_5 and a_2 are the daylength constant and daylength coefficients.

References

Johnson, R.C., Mornhinweg, D.W., Ferris, D.M., Heitholt, J.J., 1987. Leaf Photosynthesis and Conductance of Selected Triticum Species at Different Water Potentials. Plant Physiology 83, 1014-1017.

Sus, O., Williams, M., Bernhofer, C., Beziat, P., Buchmann, N., Ceschia, E., Doherty, R., Eugster, W., Grunwald, T., Kutsch, W., *et al.*, 2010. A linked carbon cycle and crop developmental model: Description and evaluation against measurements of carbon fluxes and carbon stocks at several European agricultural sites. Agriculture, ecosystems and environment. 139, 402-418.

Williams, M., E.B Rastetter, D.N Fernandes, M.L. Goulden, G.R. Shaver, Johnson, L.C., 1997. Predicting gross primary productivity in terrestrial ecosystems. Ecological Applications 7, 882 - 894.

Williams, M., Law, B.E., Anthoni, P.M., Unsworth, M.H., 2001. Use of a Simulation Model and Ecosystem Flux Data to Examine Carbon-Water Interactions in Ponderosa Pine. Tree Physiology 21, 287-298.